

Rudder Incorporated Winglet Design for blended wing body aircraft

R. Hageman



Rudder Incorporated Winglet Design

for blended wing body aircraft

by

R. Hageman

to obtain the degree of Master of Science
at the Delft University of Technology,
to be defended publicly on Tuesday November 22, 2016 at 13:00.

Student number:	1306111
Project duration:	February 25, 2016 – November 22, 2016
Thesis registration number:	102# 16# MT# FPP
Thesis committee:	Dr. A. G. Rao, TU Delft, supervisor
	Dr. ir. M. Voskuijl, TU Delft
	Dr. ir. R. Vos, TU Delft
	Dr. ir. M.M. van Paassen, TU Delft

An electronic version of this thesis is available at
<http://repository.tudelft.nl/>



Preface

This thesis is part of my graduation project for obtaining the degree of Master of Science in Aerospace Engineering at Delft University of Technology. My academic career, that can be characterized by personal challenges, has enabled me to become a stronger person. Without the guidance and support of friends and family this would not have been possible. Therefore, I would like to thank those who have helped me along the way.

For my thesis assignment I drafted an ambitious proposal, that resulted in the current body of work. The diversity of the project required me to utilize programs written in languages I was not familiar with. Thanks to Jian Hao Wei, who patiently helped me understand his program, I was able to complete the assignment in a timely manner. I would also like to thank Dario, with whom I spend many afternoon trying to decode and modify a different software package. Guided by the expertise of Mark Voskuyl, we were able to incorporate the program in our research. The feedback provided by Roelof Vos enabled me to critically reflect on my work. I would also like to thank Leo Veldhuis for his insight into the complex aerodynamic phenomena. However, first and foremost I would like to thank Arvind Gangoli Rao for the opportunity to partake in interesting projects. Throughout my master he encouraged me to continue develop and expand my capabilities and understanding, for which I'm very grateful.

Finally, my thanks goes to my friends and family for their unwavering support during these last couple of months. And especially to my sister, who provided valuable feedback on this report.

*R. Hageman
Delft, November 2016*

Summary

Concern about the environmental footprint of aviation has re-sparked the interest in unconventional configurations, such as the blended wing body aircraft, BWB. While most research studies recognize the potential of the hybrid-body, they also list a number of challenges. Amongst these challenges is the need for adequate lateral-directional stability and control, which is complicated due to the concept's relative short moment arm and limited available control-volume. To refrain from further straining the trailing edge for directional control, most BWB employ either a conventional vertical tail or resort to yaw-control incorporated winglets. By combining the functionality of the vertical fin with the aerodynamic benefits of a winglet, the required control surface could be obtained without the drag penalty associated with a vertical tail.

Although a number of BWB, such as the X-48B, operate these active winglets, limited information is available on the design of such a non-planar component and its influence on the stability and control characteristics. The presented research investigates these aspects aiming to provide a better understanding of the influence of the individual winglet design variables. A design methodology was devised that implements a first order panel method connected to a virtual test flight program. The information collected from the analysis of 400 configurations was used to construct response surfaces that span the entire design space. The generated winglet design program also monitors the impact of the non-planar component on the aerodynamic performance, weight, and operating cost. This enables the user to optimize the tip device, given specified stability and control requirements.

It was found that implementing yaw-control incorporated winglets resulted in a statically stable aircraft that meets the requirements for crosswind landing. However, none of the tested configurations meet the dutch roll frequency criterion, corresponding to a satisfactory handling quality level. Research indicates that the tip device has little influence on ω_{dr} , indicating the need to modify the baseline aircraft. Analysis of the response surface estimates for the asymmetric eigenmodes yields a significantly large average error and standard deviation for the spiral mode, as compared to the results obtained from the corresponding flight mechanics models. Therefore, it is omitted from the study. Similar errors can be found for a number of other parameters. These parameters can generally be characterized by values that approach zero. The error and standard deviation is amplified when the parameter also changes sign. Normalization of these stability and control characteristics had little influence on the accuracy of the response surface. In recognition of the demonstrated inability of the response surface to accurately capture the behaviour of these parameters, it is concluded that further research is required to reduce the error of the estimates. Despite the indicated challenges, the system is able to explore various control surface configurations. This provides valuable insight into the behaviour of the stability and control characteristics and takes the first step towards the generation of less computational intensive models.

Contents

Summary	v
Nomenclature	ix
List of Figures	xiii
List of Tables	xv
1 Introduction	1
2 Context	3
3 Stability and Control	5
3.1 Stability Principles	5
3.1.1 Static Stability.	5
3.1.2 Dynamic Stability	7
3.2 Controllability	9
4 Winglet Design	11
4.1 Introduction	11
4.2 Aerodynamic Principles	12
4.3 Design Considerations	13
4.4 Parametrization.	14
5 Design Procedure	17
5.1 Methodology	17
5.2 Implementation	18
5.2.1 Pre-Aerodynamic Analysis	19
5.2.2 Post-Aerodynamic Analysis	20
5.3 Baseline Aircraft	23
6 Validation	25
6.1 Description of Computational Model and Data	25
6.1.1 Learjet Model 23	25
6.1.2 Fokker 100	26
6.2 Analysis of the Clean Configuration	27
6.3 Impact of Control Surface Options.	29
7 Sensitivity Study	33
7.1 Aerodynamic Analysis	33
7.2 Response Surface Models	35
8 Results	39
8.1 Parameter Analysis.	39
8.1.1 Performance Parameters	39
8.1.2 Stability and Control Parameters	44
8.1.3 Eigenmode Analysis	51
8.2 Winglet Optimization	57
9 Conclusion and Recommendations	63

A Baseline Aircraft	65
B Components	69
B.1 Multi-Model-Generator	69
B.2 VSAero	70
B.3 EMWET	71
B.4 DOC	72
B.5 Phalanx	74
C Sensitivity Data	75
C.1 Sensitivity Data: Regression and Correlation Models	75
C.2 Sensitivity Data: Error Estimation	79
Bibliography	85

Nomenclature

Latin Symbols

A	aspect ratio	[–]
AFW	airframe weight	[kg]
b	span	[m]
$b_{flapped}$	flapped span	[m]
BH	block hour	[h]
\bar{c}	mean aerodynamic chord	[m]
C_D	aircraft drag coefficient	[–]
C_{D_i}	induced drag coefficient	[–]
$C_{D_{HL}}$	high lift drag coefficient	[–]
C_L	aircraft lift coefficient	[–]
C_{L_0}	aircraft lift coefficient at zero angle of attack	[–]
$C_{L_{max}}$	maximum aircraft lift coefficient	[–]
C_l	section lift coefficient	[–]
C_l	rolling moment coefficient	[–]
C_{l_0}	steady flight rolling moment coefficient	[–]
C_{l_p}	rolling moment coefficient due to roll-rate	[–]
C_{l_r}	rolling moment coefficient due to yaw-rate	[–]
C_{l_β}	rolling moment coefficient due to sideslip	[–]
C_{l_δ}	rolling moment coefficient due to control surface deflection	[–]
C_{m_q}	pitching moment coefficient due to change in pitch-rate	[–]
C_{m_u}	pitching moment coefficient due to change in velocity	[–]
C_{m_α}	pitching moment coefficient due to change in angle of attack	[–]
$C_{m_\dot{\alpha}}$	pitching moment coefficient due to rate of angle of attack	[–]
C_n	yawing moment coefficient	[–]
C_{n_0}	steady flight yawing moment coefficient	[–]
C_{n_p}	yawing moment coefficient due to roll-rate	[–]
C_{n_r}	yawing moment coefficient due to yaw-rate	[–]
C_{n_β}	yawing moment coefficient due to sideslip	[–]
$C_{n_\dot{\beta}}$	yawing moment coefficient due to rate of sideslip	[–]
C_{n_δ}	yawing moment coefficient due to control surface deflection	[–]
C_p	pressure coefficient	[–]
C_{X_0}	steady flight X-force coefficient	[–]
C_{X_q}	X-force coefficient due to change in pitch-rate	[–]
C_{X_u}	X-force coefficient due to change in velocity	[–]
C_{X_α}	X-force coefficient due to change in angle of attack	[–]
C_Y	side-force coefficient	[–]
C_{Y_0}	steady flight side-force coefficient	[–]
C_{Y_p}	side-force coefficient due to roll-rate	[–]
C_{Y_r}	side-force coefficient due to yaw-rate	[–]
C_{Y_β}	side-force coefficient due to sideslip	[–]
$C_{Y_\dot{\beta}}$	side-force coefficient due to rate of sideslip	[–]
C_{Y_δ}	side-force coefficient due to control surface deflection	[–]
C_{Z_0}	steady flight Z-force coefficient	[–]
C_{Z_q}	Z-force coefficient due to change in pitch-rate	[–]
C_{Z_u}	Z-force coefficient due to change in velocity	[–]
C_{Z_α}	Z-force coefficient due to change in angle of attack	[–]
$C_{Z_\dot{\alpha}}$	Z-force coefficient due to change in rate of angle of attack	[–]

c_r	<i>root chord</i>	[m]
$CG_x_{aircraft}$	<i>x-coordinate of the centre of gravity of the aircraft</i>	[–]
cr_w	<i>wingtip to winglet root chord ratio</i>	[–]
D	<i>non-dimensional time derivative</i>	[–]
e	<i>oswald efficiency factor</i>	[–]
e_{avg}	<i>average error</i>	[%]
F_{AY}	<i>side-force</i>	[N]
FC	<i>flight cycles</i>	[–]
FTA	<i>number of flight test aircraft</i>	[–]
H_w	<i>hingeline to winglet chord ratio</i>	[–]
I_{xx}	<i>moment of inertia about x-axis</i>	[kg m ²]
I_{xz}	<i>product of inertia</i>	[kg m ²]
I_{yy}	<i>moment of inertia about y-axis</i>	[kg m ²]
I_{zz}	<i>moment of inertia about z-axis</i>	[kg m ²]
K	<i>non-dimensional moment of inertia</i>	[–]
L	<i>rolling moment</i>	[Nm]
L_A	<i>rolling moment</i>	[Nm]
l_w	<i>winglet length</i>	[mm]
M	<i>pitching moment</i>	[Nm]
MAC	<i>mean aerodynamic chord</i>	[m]
$MTOW$	<i>maximum take-off weight</i>	[kg]
N_A	<i>yawing moment</i>	[Nm]
NE	<i>number of engines</i>	[–]
OEW	<i>operating empty weight</i>	[kg]
p	<i>roll-rate</i>	[rad/s]
q	<i>pitch-rate</i>	[rad/s]
r	<i>yaw-rate</i>	[rad/s]
Q	<i>number of produced aircraft</i>	[–]
\bar{q}	<i>dynamic pressure</i>	[Pa]
R_b	<i>blending radius</i>	[m]
r_e	<i>end position of the rudder as a ratio of l_w</i>	[–]
r_s	<i>start position of the rudder as a ratio of l_w</i>	[–]
S	<i>surface area</i>	[m ²]
$S_{flapped}$	<i>flapped surface area</i>	[m ²]
S_{ref}	<i>reference surface area</i>	[m ²]
SFC	<i>specific fuel consumption</i>	[g/kN/s]
$SLST$	<i>static thrust at sea level</i>	[N]
$T_{\frac{1}{2}}$	<i>time to half the amplitude</i>	[s]
T_{rm}	<i>roll mode time constant</i>	[s]
\dot{u}	<i>acceleration in x-direction</i>	[m/s ²]
V	<i>velocity</i>	[m/s]
V_{cw}	<i>crosswind velocity</i>	[m/s]
W_0	<i>gross weight</i>	[kg]
W_e	<i>empty weight</i>	[kg]
W_{engine}	<i>engine weight</i>	[kg]
W_f	<i>fuel weight</i>	[kg]
W_{wing}	<i>structural wing weight</i>	[kg]
w	<i>downwash</i>	[m/s]

Greek Symbols

α	<i>angle of attack</i>	[deg]
$\alpha_{L=0}$	<i>aircraft angle of attack at zero lift</i>	[deg]
$\alpha_{l=0}$	<i>local angle of attack at zero lift</i>	[deg]
β	<i>sideslip angle</i>	[deg]
δ	<i>control surface deflection</i>	[rad]
ζ	<i>damping ratio</i>	[–]
η	<i>imaginary part of a complex eigenvalue</i>	[–]
θ	<i>pitch angle</i>	[deg]
ρ	<i>density</i>	[kg/m ³]
σ	<i>standard deviation</i>	[%]
ϕ	<i>roll angle</i>	[deg]
Ψ	<i>yaw angle</i>	[deg]
φ	<i>winglet cant angle</i>	[deg]
ω	<i>natural frequency</i>	[rad/s]
Λ	<i>sweep angle</i>	[deg]
Λ_w	<i>winglet sweep angle</i>	[deg]
λ	<i>eigenvalue</i>	[–]
λ	<i>winglet taper ratio</i>	[–]
μ	<i>non-dimensional weight</i>	[–]
ξ	<i>real part of a complex eigenvalue</i>	[–]

List of Figures

2.1 The X48-B scale model with active winglets - <i>source: NASA.gov</i>	4
3.1 Overview of the orientation of the selected reference frame	5
3.2 Lateral stability diagram - <i>source: J.A. Mulder et al, "Flight Dynamics" [14]</i>	9
4.1 The Armstrong Whitworth AW-52 with end-plates for directional control - <i>source: C.V. Murray, "Full-Scale Research on a Flying Wing"</i>	14
4.2 Parametric description of the rudder-incorporated winglet	15
5.1 Overview of the program upto the aerodynamic analysis	19
5.2 Overview of the program after the aerodynamic analysis	20
5.3 Theoretical fuel mass and volume as a function of the cryogenic fuel fraction	23
5.4 An visualization of an older version of the AHEAD multi-fuel BWB	24
6.1 Panel method representation of the Learjet Model 23 - <i>source: J.K. Nathman and A. McComas, "Comparison of Stability and Control Calculations from Vortex Lattice and Panel Methods" [28]</i>	26
6.2 Panel method representation of the Fokker 100	26
6.3 Comparison of the lift coefficient	27
6.4 Comparison of the drag coefficient	27
6.5 Comparison of the side-force coefficient	28
6.6 Comparison of the yawing-moment coefficient	28
6.7 Comparison of the rolling-moment coefficient	28
6.8 Multi-Model-Generator control surface options - <i>source: J.H. Wei, "Parametric modelling for determining aircraft stability & control derivatives" [29]</i>	29
6.9 Aerodynamic comparison of the different control surface models	30
6.10 Pressure distribution comparison for a 20.0 degrees control surface deflection - <i>source: J.H. Wei, "Parametric modelling for determining aircraft stability & control derivatives" [29]</i>	30
6.11 Comparison of the different control surface models on the yawing-moment coefficient	31
7.1 Computation time versus grid size for both tested solvers	35
8.1 The variation in lift over drag as a function of the aspect ratio and cant angle	40
8.2 An isolated overview of the effect of the cant angle on the lift coefficient .	41
8.3 Comparison between the lift and drag coefficient of a 3.0 m winglet . . .	41
8.4 The variation in spanload of a 3.0 m winglet as a function of the root chord ratio	41
8.5 The variation in lift over drag as a function of the aspect ratio and sweep angle	42
8.6 An isolated overview of the effect of the cant angle on the structural wing weight	43
8.7 The variation in structural wing weight as a function of the cant and sweep angle	44
8.8 The variation in effective dihedral as a function of the cant angle and aspect ratio	45
8.9 The effect of sideslip on the perceived sweep angle - <i>source: J.A. Mulder et al, "Flight Dynamics" [14]</i>	46
8.10 An isolated overview of the effect of the cant angle on the effective dihedral	46

8.11 The variation in effective dihedral as a function of the cant and sweep angle	47
8.12 The variation in side-force coefficient due to sideslip as a function of the cant angle and aspect ratio	48
8.13 An isolated overview of the effect of the cant angle on the side-force coefficient due to sideslip	48
8.14 The variation in side-force coefficient due to sideslip as a function of the cant and sweep angle	49
8.15 The variation in control power as a function of the cant angle and aspect ratio	49
8.16 An isolated overview of the effect of the cant angle and sweep on the control power	50
8.17 An isolated overview of the effect of the hinge position and various geometric parameters on the control power	50
8.18 The variation in roll damping as a function of the cant angle and aspect ratio	52
8.19 An isolated overview of the effect of the various geometric parameters on the roll mode	53
8.20 The variation in dutch roll damping as a function of the cant angle and aspect ratio	54
8.21 An isolated overview of the effect of the various geometric parameters on the dutch roll damping	55
8.22 The variation in dutch roll frequency as a function of the cant angle and aspect ratio	56
8.23 An isolated overview of the effect of the various geometric parameters on the dutch roll frequency	56
8.24 Overview of the tested samples	57
8.25 Overview of the stability characteristics for sideslip	60
8.26 Comparison between the linearised and non-linearised stability characteristics for sideslip	61
8.27 Comparison between the linearised and non-linearised DOC control power	62
8.28 Isometric view of the best sample DOC configuration at an angle of attack of 4.9 degrees	62
A.1 Top view of the preliminary AHEAD multi-fuel BWB	66

List of Tables

3.1	<i>Handling quality level criteria for the coupled and uncoupled roll and spiral</i>	8
3.2	<i>Handling quality level criteria for the dutch roll</i>	8
4.1	<i>Design space implemented in the winglet design program</i>	15
7.1	<i>Grid sensitivity study for the Lapack solver</i>	34
7.2	<i>Grid sensitivity study for the Blocked GS solver</i>	34
7.3	<i>Accuracy of the Gaussian correlation model on the various parameters</i>	36
7.4	<i>Accuracy of the cubic correlation model on the various parameters</i>	37
7.5	<i>Established error, as computed using a 2nd order polynomial cubic scheme</i>	38
8.1	<i>Geometry of the optimized configurations</i>	57
8.2	<i>Stability and control parameters of the optimized configurations</i>	58
8.3	<i>Optimization parameters of the optimized configurations</i>	58
8.4	<i>Stability and control parameter comparison to VSAero model</i>	59
8.5	<i>Optimization parameter comparison to VSAero model</i>	59
8.6	<i>Geometry of the best samples</i>	59
8.7	<i>Stability and control parameters of the best samples</i>	60
8.8	<i>Optimization parameters for the best samples</i>	60
A.1	<i>High level mission requirements of the AHEAD MF-BWB</i>	65
A.2	<i>Weight break-down of the MF-BWB preliminary design study</i>	65
A.3	<i>Centre of gravity and inertias of the MF-BWB preliminary design study</i>	65
A.4	<i>Planform parameters and aerodynamic properties of the MF-BWB preliminary design study</i>	66
A.5	<i>Planform coordinates and quarter chord twist angle</i>	67
C.1	<i>Accuracy of the exponential correlation model on the various parameters</i>	75
C.2	<i>Accuracy of the Gaussian correlation model on the various parameters</i>	76
C.3	<i>Accuracy of the linear correlation model on the various parameters</i>	76
C.4	<i>Accuracy of the spherical correlation model on the various parameters</i>	77
C.5	<i>Accuracy of the cubic correlation model on the various parameters</i>	77
C.6	<i>Accuracy of the spline correlation model on the various parameters</i>	78
C.7	<i>Established error for C_{n_β} and $C_{n_{\delta_r}}$, as computed using a 2nd order polynomial cubic scheme</i>	79
C.8	<i>Established error for C_{l_β} and C_{Y_β}, as computed using a 2nd order polynomial cubic scheme</i>	80
C.9	<i>Established error for $\delta_{r_{cw}}$, as computed using a 2nd order polynomial cubic scheme</i>	81
C.10	<i>Established error for λ_{sp} and λ_{rm}, as computed using a 2nd order polynomial cubic scheme</i>	82
C.11	<i>Established error for ζ_{dr} and ω_{dr}, as computed using a 2nd order polynomial cubic scheme</i>	83
C.12	<i>average error and standard deviation of the presented parameters</i>	84

1

Introduction

Although there are numerous types of aircraft in service today, most adhere to the classical tube-and-wing configuration in which a tail is present to stabilize the vehicle. Over the years various studies have been conducted to derive methods to estimate the stability and control characteristics of these types of aircraft to be implemented during the early stages of design. These methods are often based on empirical data and tailored to incorporate the individual components of an aircraft [1–3]. However, with the increasing demand in passenger travel and freight transport, there is concern about the environmental impact of aviation. To reduce the environmental footprint, despite the estimated growth rate of air travel of 5%, a step change in aircraft design is needed. Renewed interest in unconventional configurations, such as the blended wing body (BWB), produced a number of research studies. Literature identifies the stability and control aspect as one of the main challenges of the BWB aircraft [4, 5]. The problem can largely be attributed to the required control surface volume to meet the handling characteristics, as a result of the relative short moment arm. Adequate simulation models are required to predict the stability and control characteristics. As most existing models incorporate empirical data, these models need to be modified and validated for this new configuration. Although some studies have been performed to translate a number of stability and control methods for the use for BWB aircraft, limited information is currently available [6–8]. The challenges can be further specified to longitudinal and directional control [4–6]. A detailed investigation by Cook and De Castro into the longitudinal characteristics of civil BWB aircraft indicates the need to analyse the lateral-directional stability and control [9]. To gain directional control, without sacrificing valuable trailing edge span needed for lateral and longitudinal control, yaw-control incorporated winglets are proposed. By combining the functionality of the vertical fin with the aerodynamic benefits of a winglet, the required control surface could be obtained without the drag penalty associated with a vertical tail [1].

Limited information is available on the design of such a non-planar component and its influence on the stability and control characteristics of the aircraft. A better understanding of the influence of individual design parameters on these characteristics could provide future designers with the tools needed to generate models able to accurately describe the behaviour of BWB aircraft. Therefore, the research question was formulated to be:

What is the influence of the design variables of a yaw-control incorporated winglet on the lateral-directional stability and control of blended wing body aircraft?

To answer this question a design methodology able to design and optimize an active winglet needs to be devised and analysed. This leads to the secondary research question:

How to design and optimize an effective winglet for blended wing body aircraft with respect to drag, weight, and operating costs, which provides adequate lateral-directional stability and control, by means of a computer aided optimization procedure?

The report will first provide the context of the research. Once the challenges have been identified, a more detailed overview of the fields of interest will be provided. The requirements listed in these chapters will form the foundation for the design process. The selected methodology and its implementation will be discussed in detail in Chapter 5. Followed by the validation of the aerodynamic analysis and its computed stability and control derivatives. Next, a sensitivity study is performed to establish the effect of the parameters linked to the design procedure on the accuracy of the results. The subsequent chapter will present the results of the winglet optimization and will analyse the influence of the individual design parameters. The research will be concluded by critically reflecting on the selected design procedure and will provide recommendations for future research.

2

Context

Concern about the environmental footprint of aviation has created the need for more efficient aircraft and engines, as well as the need to utilize alternative fuels. These challenges have sparked the interest in unconventional aircraft configurations. One of the concepts that has attracted a lot of attention is the blended wing body aircraft, BWB. The concept is a blend between the conventional tube-and-wing configuration and the flying wing aircraft.

In the early half of the 20th century the flying wing was considered the pinnacle of powered flight by a number of respected aircraft designers [10]. The strongest advocate for this concept, the renowned Jack Northrop, started his research on this type of aircraft in 1928. His research resulted in the development of the XB-35 and YB-49 long-range bomber. Although the Air Force recognized the capabilities of the jet powered YB-49, the production contract was cancelled in favour of the more conventional B-47. In the late 1980's the Northrop company presented a new flying wing, the B-2 Spirit. Powered by 4 General Electric turbofan engines, the aircraft is considered to be one of the most advanced tactical bombers in service today. Despite the demonstrated capabilities, the aeronautical community is divided on the potential of the all-flying wing for commercial purposes. The main concerns about the performance of this concept can be traced back to the inefficient manner in which the useful load is to be stored within the wing and the relative low aspect ratio of the system. Reference [10] investigates these aspects by comparing both concepts. The study indicates that, for a given useful load and operating condition, the aerodynamic performance of the flying wing is slightly better. However, the research demonstrates that better results could be obtained by blending the fuselage and wing, creating the blended wing body aircraft. The enhanced aerodynamics could potentially reduce the environmental footprint [4, 10, 11]. However, the improved aerodynamic properties need to offset the weight penalty associated with the non-cylindrical pressure cabin.

Although most research studies recognize the potential of the concept, the CO_2 emission levels could be reduced even further by employing alternative fuels. Studies investigating the implementation of cryogenic fuels in the classical tube-and-wing configuration illustrate a substantial increase in drag [12]. However, the volume distribution inherent to the hybrid body could accommodate cryogenic fuels, such as LNG and LH₂, without significantly compromising the aerodynamic performance. The aerodynamic characteristics presented in literature, in combination with the potential to utilize alternative energy carriers, warrant the rise in interest in the BWB concept.

Research into the concept has not only demonstrated its potential, it also revealed a number of challenges [4, 5]. Amongst the identified challenges are the stability and control of the aircraft. In contrast to popular belief, it is possible to design a naturally stable hybrid body, as is evident from the designs by Armstrong, Northrop, Horton, and others. However, most of these vehicles are designed for a limited number of passengers, simplifying

the design process. Contemporary studies indicate that the concept has to cope with a strong nose-down moment [4, 11]. This nose-down moment complicates the control allocation and limits the applicability of trailing edge devices. To overcome this moment aerodynamicists can resort to reflex airfoils, as featured on the Horton aircraft [4]. Other possibilities include the use of leading edge carving or the implementation of a canard.

The challenges related to longitudinal stability and control have a direct impact on the lateral-directional control options. Due to the relative short moment arm inherent to the BWB concept, designers often have to employ a complex control surface architecture. This as a result of the limited available trailing edge control surface volume. To reduce the strain on the trailing edge the use of split drag rudders for directional control is omitted. Other possibilities to gain directional control comprise of the use of vertical surfaces or the employment of a complex control surface platform containing body flaps. However, literature notes the low yaw-damping of planar aircraft designs [4, 5]. Therefore, most BWB feature either winglets or a more conventional vertical tail for lateral-directional stability and control. By combining the functionality of the vertical fin with the aerodynamic benefits of a winglet, the required control surface could be obtained without the drag increase of a vertical tail [1]. Depending on the configuration, winglet rudders have the added advantage of having a larger moment arm.

Despite the fact that a number of BWB aircraft fly the yaw-control incorporated winglet, limited information is available on the impact of such a configuration on the stability and control of the system. It is to be noted that the collaboration of Stanford, Boeing, and NASA produced a BWB study that yielded windtunnel testing and the production of a scale model for flight testing. Data of their X48-B model, figure 2.1, that employs active winglets for directional control is available and will be used to define the design space.



Figure 2.1: The X48-B scale model with active winglets - source: NASA.gov

With renewed interest in unconventional configurations such as the BWB, research into the effect of yaw-control incorporated winglets could provide valuable information for future designs. By investigating the influence of various winglet design parameters on the stability and available control power new models could be developed for the early stages of design. Therefore, the thesis will devise a methodology to analyse these aspects by generating a computer program able to design and optimize an active winglet.

3

Stability and Control

In the previous chapter it was indicated that one of the challenges associated with blended wing body design was related to stability and control. In order to connect these aspects to the design of an active winglet the stability and control requirements need to be quantitatively identified. This chapter will discuss the fundamental principles of flight dynamics and identify the driving requirements. It will do so by differentiating between stability and control.

3.1. Stability Principles

The stability of an aircraft can be described by its response to a disturbance about one or more of its three axes, while originating from a specified equilibrium or trimmed condition. When the forces and moments created by the disturbance oppose the motion initiated by said disturbance, the aircraft is termed statically stable. If the resultant motion converges on a new equilibrium condition, the aircraft also possesses dynamic stability.

3.1.1. Static Stability

As indicated by the definition, the selected trimmed state defines the initial conditions for the stability analysis. Hence, the trimmability of the aircraft, which is largely dictated by the static stability characteristics, is of great importance. In order to analyse these characteristics, a frame of reference is to be selected. Most flight dynamics manuals formulate the equations of motion with respect to either the wind, body, or stability frame. These right-handed orthogonal reference frames position its origin at the aircraft centre of gravity. For the analysis of forces and moments the stability frame was selected. The orientation of the frame for zero sideslip and angle of attack is presented in figure 3.1.

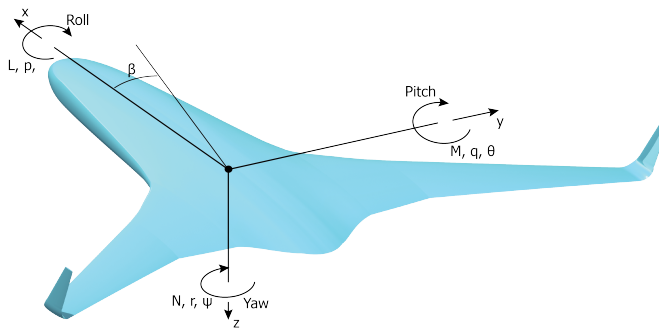


Figure 3.1: Overview of the orientation of the selected reference frame

Symmetry about the longitudinal axis of most aircraft reduces the complexity the equations of motion by decoupling the symmetric and asymmetric motions. As the focus of the research is on sizing the winglet to achieve satisfactory lateral-directional stability and control, the analysis of the requirements presented in this chapter will be limited to the asymmetric motions. To establish the mathematical tools needed to determine the static stability characteristics, one needs to review the forces and moments acting on the aircraft. It is to be noted that these forces and moments are dependent on the selected flight conditions. However, literature indicates the limited effect of the flight conditions on the lateral-directional characteristics [13, 14]. For the asymmetric motions the side-force F_{AY} , the rolling moment L_A , and the yawing moment N_A are of interest and can be non-dimensionalized using equations 3.1-3.3 [1, 3, 7, 14].

$$F_{AY} = C_Y \bar{q} S \quad (3.1)$$

$$L_A = C_l \bar{q} S b \quad (3.2)$$

$$N_A = C_n \bar{q} S b \quad (3.3)$$

These coefficients can be further specified using a first order Taylor series expansion.

$$C_Y = C_{Y_0} + C_{Y\beta} \beta + C_{Y\delta_a} \delta_a + C_{Y\delta_r} \delta_r \quad (3.4)$$

$$C_l = C_{l_0} + C_{l\beta} \beta + C_{l\delta_a} \delta_a + C_{l\delta_r} \delta_r \quad (3.5)$$

$$C_n = C_{n_0} + C_{n\beta} \beta + C_{n\delta_a} \delta_a + C_{n\delta_r} \delta_r \quad (3.6)$$

Due to symmetry, the steady state flight coefficients, indicated by index 0, are usually very small or equal to zero [14, 15]. Hence the system can be reduced to:

$$\begin{Bmatrix} C_Y \\ C_l \\ C_n \end{Bmatrix} = \begin{bmatrix} C_{Y\beta} & C_{Y\delta_a} & C_{Y\delta_r} \\ C_{l\beta} & C_{l\delta_a} & C_{l\delta_r} \\ C_{n\beta} & C_{n\delta_a} & C_{n\delta_r} \end{bmatrix} \begin{Bmatrix} \beta \\ \delta_a \\ \delta_r \end{Bmatrix} \quad (3.7)$$

The first column of the matrix on the right-hand side notes the stability characteristics of the aircraft without control deflections. When the disturbance initiates a sideslip the vertical fin or winglet will experience a change in angle of attack. In a statically stable design the resultant force balance will oppose the sideslipping motion. Closely related to $C_{Y\beta}$ is the static directional, or weathercock, stability derivative $C_{n\beta}$. The weathercock stability derivative describes the ability of the aircraft to generate a restoring yawing-moment to counter the sideslip. The main contributions to $C_{Y\beta}$ and $C_{n\beta}$ are the fuselage and the vertical fin or winglet, which explains the weak yaw-damping of planar configurations. As the restoring force generated by the vertical fin is often positioned above the centre of gravity, it will initiate a rolling motion, illustrating the need to analyse both the lateral and directional stability characteristics.

The remaining stability derivative, $C_{l\beta}$, is often referred to as the *effective dihedral* and forms one the main lateral stability derivatives. As the coefficient mainly depends on the characteristics of the wing, it is expected that the influence of the non-planar component will be minor. Therefore the static stability requirement following from $C_{l\beta}$ will not be implemented as a limiting design criterion. Analysis of the aerodynamic properties of the aircraft without winglets will produce the so-called tail-off characteristics, which will be used to substantiate this claim. It will also provide insight into the impact of the tip device on the static stability of the aircraft as a whole.

Following the definition and orientation of the forces and moments the static stability requirements can be listed to be:

$$\frac{dC_Y}{d\beta} < 0 \quad (3.8)$$

$$\frac{dC_n}{d\beta} > 0 \quad (3.9)$$

$$\frac{dC_l}{d\beta} < 0 \quad (3.10)$$

It is to be noted that these requirements must hold throughout the entire flight envelope. Hence it is to be validated that the non-linearities associated with large α and β do not significantly compromise the static stability.

3.1.2. Dynamic Stability

The definition for stability indicates the need for an initial equilibrium condition. The behaviour of the aircraft when it encounters an atmospheric or pilot induced disturbance at such a trimmed condition can be described by the equations of motion. A full derivation of these equations can be found in most text books on flight dynamics and will not be repeated in the presented research study. As previously mentioned, the symmetric pitching motion can be decoupled from the lateral-directional dynamics, resulting in two systems of equations. Although the research focusses on the asymmetric behaviour of the vehicle, the characteristics of the symmetrical eigenmotions will also be included in the computer aided analysis.

$$\begin{bmatrix} C_{X_u} - 2\mu_c D_c & C_{X_\alpha} & C_{Z_0} & C_{X_q} \\ C_{Z_u} & C_{Z_\alpha} + (C_{Z_\alpha} - 2\mu_c)D_c & -C_{X_0} & C_{Z_q} + 2\mu_c \\ 0 & 0 & -D_c & 1 \\ C_{m_u} & C_{m_\alpha} + C_{m_\alpha} D_c & 0 & C_{m_q} - 2\mu_c K_Y^2 D_c \end{bmatrix} \begin{bmatrix} \dot{u} \\ \alpha \\ \theta \\ \frac{q\dot{c}}{V} \end{bmatrix} = \begin{bmatrix} -C_{X_{\delta_e}} \\ -C_{Z_{\delta_e}} \\ 0 \\ -C_{m_{\delta_e}} \end{bmatrix} \delta_e \quad (3.11)$$

$$\begin{bmatrix} C_{Y_\beta} + (C_{Y_\beta} - 2\mu_b)D_b & C_L & C_{Y_p} & C_{Y_r} - 4\mu_b \\ 0 & -\frac{1}{2}D_b & 1 & 0 \\ C_{l_\beta} & 0 & C_{l_p} - 4\mu_b K_X^2 D_b & C_{l_r} + 4\mu_b K_{XZ} D_b \\ C_{n_\beta} + C_{n_\beta} D_b & 0 & C_{n_p} + 4\mu_b K_{XZ} D_b & C_{n_r} - 4\mu_b K_Z^2 D_b \end{bmatrix} \begin{bmatrix} \beta \\ \phi \\ \frac{pb}{2V} \\ \frac{rb}{2V} \end{bmatrix} = \begin{bmatrix} -C_{Y_{\delta_a}} & -C_{Y_{\delta_r}} \\ 0 & 0 \\ -C_{l_{\delta_a}} & -C_{l_{\delta_r}} \\ -C_{n_{\delta_a}} & -C_{n_{\delta_r}} \end{bmatrix} \begin{bmatrix} \delta_a \\ \delta_r \end{bmatrix} \quad (3.12)$$

The coefficients listed in the symmetric, equation 3.11, and asymmetric equations of motion, equation 3.12, will be obtained from an aerodynamic simulation. Solving the eigenvalue problem of the coefficient matrix provides information on the characteristics of these so-called eigenmotions. The solution of the lateral-directional characteristic equation generally consists of 2 non-oscillatory and 1 harmonic motion. The simplified equations of motion, given by equation 3.11 and 3.12, will be used in Chapter 8.1.3 to discuss the results. It is to be noted that these results will be based on simulations that employ the full, non-linear equations of motion.

Based on these properties, the predicted *handling quality levels*, HQL, can be derived. Handling qualities depict the ease and precision with which the pilot can execute a flight task [16]. Some of these characteristics are difficult to describe quantitatively, as they

are based on the opinion of the pilot. However, for analytical purposes the handling quality level has been developed to quantitatively document the behaviour of specific type aircraft. Different flight phases require different handling characteristics. Therefore, the flight envelope is decomposed into flight phase category A, B, and C. In which A corresponds to military combat operations, B relates to the nominal flight stages such as cruise and climb. The final category, C, encompasses the more critical take-off and landing. All presented HQL will be with respect to the flight phase B requirements.

The first eigenmotion to be discussed is the aperiodic roll subsidence, or roll mode, denoted by subscript $_{rm}$. The roll mode can be explained as the lag in response to a control input and is directly related to the roll stability. The behaviour of this mode is largely determined by the characteristics of the wing and can generally be substantially decoupled from the remaining two lateral-directional eigenmotions. Table 3.1 relates the time constant to the corresponding HQL.

Table 3.1: *Handling quality level criteria for the coupled and uncoupled roll and spiral*

mode	criterion	HQL 1	HQL 2	HQL 3	HQL 4
roll	T_{rm}	≤ 1.4	≤ 3.0	≤ 10.0	> 10.0
spiral	$T_{\frac{1}{2}}$	≥ 20	≥ 8	≥ 4	< 4
coupled	$\zeta \omega$	> 0.5	> 0.3	> 0.15	≤ 0.15

The second motion is also non-oscillatory and is termed the spiral mode. Usually characterized by slow dynamic behaviour, the spiral is a complex coupled motion in yaw, roll, and sideslip [13]. The properties of this eigenmotion are highly dependent on the effective dihedral and weathercock stability. Depending on the balance between these parameters the spiral can be stable or unstable. However, as $C_{l\beta}$ and $C_{n\beta}$ are often approximately equal, the second aperiodic motion will be nearly neutrally stable. Similar to the roll subsidence mode, the HQL of the spiral is dependent on the time to half the amplitude, table 3.1.

The final lateral-directional eigenmotion is the harmonic dutch roll. Named after the swaying motion of Dutch ice-skaters, the eigenmotion describes the classical damped periodic motion in yaw. This yawing motion is coupled to roll and to a lesser extend to sideslip [13]. The aerodynamic properties of the vertical fin or winglet largely dictates the characteristics of the eigenmotion. This leads to contradictory design requirements, as will be illustrated shortly. The handling quality levels of the eigenmotion are based on both the damping and frequency, as listed in table 3.2.

Table 3.2: *Handling quality level criteria for the dutch roll*

mode	criterion	HQL 1	HQL 2	HQL 3	HQL 4
dutch roll	ζ	≥ 0.08	≥ 0.02	> 0.00	≤ 0.00
	ω	≥ 0.4			< 0.4
	$\zeta \omega$	≥ 0.15	≥ 0.05	≥ 0.00	< 0.00

Although a large fin would be beneficial for the stability of the dutch roll, it would have a negative impact on the spiral. Therefore a compromise needs to be made, which often yields an unstable spiral mode and weakly damped dutch roll. The Routh-Hurwitz stability criteria can be employed to find a combination of stability derivatives that results in both a stable spiral and dutch roll. The stability criteria utilizes the characteristic equation, equation 3.13, in combination with the Routh's discriminant, equation 3.14. Based on the properties of these individual components the lateral stability diagram can be constructed. The diagram, depicted in figure 3.2, indicates the possible combinations of $C_{l\beta}$ and $C_{n\beta}$ that yield a stable spiral and dutch roll.

$$A\lambda_b^4 + B\lambda_b^3 + C\lambda_b^2 + D\lambda_b + E = 0 \quad (3.13)$$

$$R = BCD - AD^2 - B^2E \quad (3.14)$$

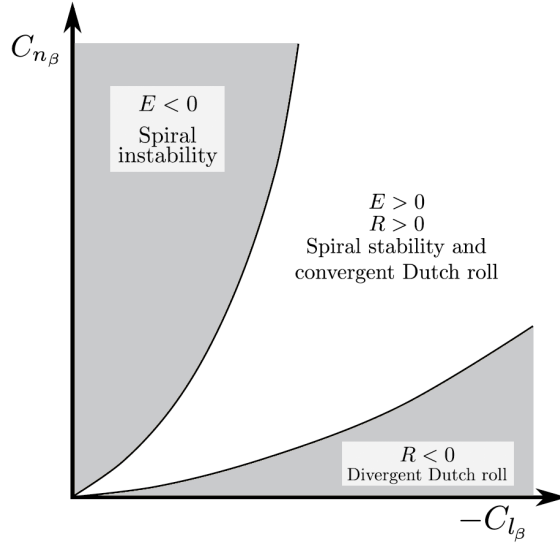


Figure 3.2: Lateral stability diagram - source: J.A. Mulder et al, "Flight Dynamics" [14]

3.2. Controllability

The rudder-incorporated winglets are the pilot's primary yaw controls. Deflection of these control surfaces alter the curvature of these non-planar surfaces, yielding a change in side-force. This variation in forces and moments due to a control surface deflection is referred to as the control power. For conventional vertical fins the control power is nearly constant upto deflection angles of 25 degrees [3]. Beyond this point the non-linearities in the flow reduce the effectiveness of the rudder until flow separation deteriorates its performance. The maximum control power produced by a normal vertical fin corresponds to a deflection angle of approximately 35 degrees. However, little information is available on the behaviour of the control power of yaw-control incorporated winglets. As modern computation methods are unable to accurately capture the non-linearities, the winglet rudder is to be over dimensionalised until windtunnel test data is available [6].

A more detailed investigation into the winglet rudder, which is to fulfil the same functionalities as a conventional fin, reveals the following requirements: [1, 3, 7]

- To provide a means for achieving a steady state of equilibrium (trim)
- To provide a means to counteract disturbances, such as gusts
- To provide sufficient directional control capabilities, up to high sideslip and rudder deflection angles:
 - for manoeuvring up to maximum yaw rates
 - to maintain heading and manoeuvre during the most critical one engine inoperative, OEI, condition
 - for landing in crosswinds of up to 55.5 km/h
- To have low control forces

Literature identifies 3 critical conditions for sizing the vertical fin for commercial airliners [1, 3, 7]. The first driving requirement was listed to be the one engine inoperative condition. However, as the engines of the BWB are positioned near the plane of symmetry, the yawing moment due to engine failure will be relatively small. As a result this condition is termed to be non-critical. The second requirement dictates that the aircraft is to be able to perform a crosswind landing while maintaining sufficient control power to adjust for atmospheric disturbances and changes in heading. In the acceptable means of compliance, set forth by the European certification authority EASA, the maximum sideslip angle is set to: [17]

$$\beta = \arcsin \frac{V_{cw}}{V} \quad (3.15)$$

With V_{cw} being the crosswind velocity of 55.5 km/h. The certification specifications for large transport aircraft, CS-25 [17], indicates that angles of 15 degrees are generally sufficient to show compliance. However, during the low speed flight stages the angle, computed in equation 3.8, might be larger than the prescribed sideslip angle. Hence, the maximum sideslip angle during landing needs to be established.

The final requirement is related to both the stability and controllability of the vehicle. This requirement indicates the need to postpone stall of the winglet beyond the maximum sideslip angle. At this flight condition the aircraft still needs to possess sufficient control power to return to a more acceptable sideslip angle. As there are no empirical models to estimate boundary layer separation for active winglets and computational models have difficulties to account for the non-linearities in the flow, this requirement needs to be validated at a later stage using windtunnel tests.

4

Winglet Design

Before discussing the design methodology employed to create the non-planar component, the different aspects of winglet design will be addressed. First an introduction into the tip device will be presented, followed by the aerodynamic principles and design considerations. The chapter is concluded by listing the assumptions that define the design space.

4.1. Introduction

It was 1908 when English polymath and engineer Frederick W. Lanchester first presented his idea of trailing edge vortices [18]. In his publication titled *Aerodynamics* he visualized the effect of the pressure differential between the upper and lower surface near the wingtip. As the high pressure underneath the tip is forced to the lower pressure region on top of the wing, the flow will experience a swirl known as tip or trailing edge vortices. This rotation in the flow pushes the air over the wing downward, reducing the effective angle of attack. Since the resultant aerodynamic force is defined to be perpendicular to the flow, the lift force is tilted aft, introducing the lift induced drag. Lanchester mathematically described the lift and drag forces using potential theory, which was later substantiated by German scientist Ludwig Prandtl. These fundamental aerodynamic equations, in combination with his own observations, led Lanchester to be the first to obtain a patent for the use of non-planar wingtip devices. However, designs of the early devices were merely end-plates aiming to improve stability and reduce the effect of tip vortices.

Over the years, various studies were conducted regarding non-planar planforms. Starting with the research by Lanchester and Prandtl, seeing its first application in the build by Sommerville, it continued to inspire and intrigue scientists. An important break-through came in the mid 70's when Richard T. Whitcomb from the NASA Langley Research Center published a technical note on the use of vertical components to reduce the aerodynamic drag. He had continued the work by Nagel(1924), Mangler (1937), Weber (1956), and others, with one important distinction. While others had discussed the application of vertical plates to improve the performance of the wing, Whitcomb stated that for an end-plate to be fully effective, it ought to generate sufficient side-force. He proposed small vertical wings to be placed at the wing tips, introducing the name *winglets*[19, 20].

Boeing continued the research and in 1988 the Boeing B747-400 became the first commercial airliner to operate with these wingtip devices. After studies revealed the potential of winglets on competitor aircraft, Airbus began to develop its own winglets, termed sharklets. These smoothly blended winglets were mounted on later versions of the A320 and will also be present on the latest member of the Airbus A320 family, the A320-NEO. Continued research has produced a vast variety of winglets. These non-planar wingtip devices are currently featured on nearly all derivatives of the Airbus and Boeing fleet.

4.2. Aerodynamic Principles

The complexity of the 3-dimensional flow around the by Whitcomb prescribed tip devices makes it impossible to provide a detailed description of the aerodynamic phenomena for the vast variety of winglets. Most winglet studies limit the aerodynamic dialogue to the relocation and dissipation of tip vortices in combination with the presence of a negative drag component [20, 21]. A more elaborate account of the behaviour of the flow field will be presented in this chapter. The presented phenomena will form the foundation needed to analyse the results and to identify possible trends.

Winglets aim to reduce the lift induced drag while limiting its contribution to the other drag components. The induced drag constitutes approximately 40% of the total drag during cruise, the most fuel intensive flight segment of the long-range blended wing body aircraft [22]. In 1908 Lanchester had laid down the mathematical foundation to compute the aerodynamic forces generated by a lifting surface. Prandtl and Munk verified his computations and validated the use of vortices to describe the behaviour of a flow. According to theory each lift generating section could be represented by a circulation of strength Γ . Variation in the spanwise lift distribution would, therefore, correspond to a change in circulation strength. The resulting roll-up of vortices would lead to the aforementioned tip vortices. As these vortices push down on the flow, they introduce a downward velocity component, which effectively angles the flow, creating the lift induced drag. The on potential flow based theorems were expanded, yielding Munk's well renowned theory for minimum induced drag. Munk's theorem states that to minimize the induced drag, the roll-up of vortices should be minimized [23]. The corresponding constant downwash profile was demonstrated to be a function of the cosine of the dihedral angle. In the publication he mathematically proved that the theorem holds for both planar and non-planar configurations. This indicates that the induced drag can be minimized by carefully balancing the forces and orientation of the non-planar component.

Although a simple canted surface component could be sized according to conventional wing design strategies, the wing-winglet interaction increases the complexity of the design process. The presence of the additional surface at the wingtip allows the air to recirculate, resulting in a higher tiploading. It is paramount that these velocities near the wingtip are not amplified by the pressure distribution over the winglet. An ill designed winglet can superimpose its supersonic velocities on the main wing, causing the wingtips to experience even higher velocities. This could potentially introduce shock waves or increase its strength [24]. It could also increase the chordwise region of supersonic flow at the tip. When the supersonic section expands too far aft, the subsonic flow aft of the shock cannot remain attached, which will lead to boundary layer separation [15]. Therefore great care has to be taken while designing the junction between wing and winglet. Most early designs correspond to a simple canted winglet that features a step-change in chord. Reducing the winglet root chord and positioning it as far aft as structurally possible, would limit the effect of the winglet suction peak on the pressure distribution over the wing. It is to be noted that, if the step-change in chord is considerable, a vortex could be formed prior to reaching the winglet. This trailing vortex, albeit being relatively weak, will have an impact on the aerodynamic performance. Modern winglet designs often show winglet root chords similar to the tip chord and apply blending to reduce the interference of both lifting surfaces.

The recirculation near the wingtip is a direct result of the added surface. By mounting a winglet, the pressure differential at the wingtip is no longer required to return to zero. The resulting higher tiploading enables the wing to produce more lift, a phenomena often referred to as the increase in effective span. This change in effective span has a positive effect on the aspect ratio which in turn reduces the lift induced drag, equation 4.1. It also allows the system to operate at a slightly lower lift coefficient.

$$C_{D_i} = \frac{C_L^2}{\pi A e} \quad (4.1)$$

When the winglet is to produce forces, it will also generate an induced velocity. Due to its orientation the velocity is termed side-wash or, more generally, normal-wash. The side-wash diffuses the rotation of the flow caused by the pressure difference on the upper and lower side of the main wing. However, in general the winglets will still experience a side-flow from the trailing vortices. The resulting normal-wash angles the aerodynamic force generated by the winglet forward. Although this slightly reduces the side-force, it introduces a negative drag component, lowering the total drag of the system[19, 20].

In order to produce adequate side-forces, the winglet itself creates a pressure difference between its two sides. This results in a tip vortex, albeit this tip vortex is weaker. More importantly, the trailing vortex is located far above the wing. Therefore it has little influence on the flow over the wing. It had already been noted that the induced velocity imposed by the trailing vortices reduce the effective angle of attack and rotates the resultant force. However, as the impact of the vortices is limited, the x-component of the resultant force is minimized.

Depending on the cant angle, the aerodynamic forces generated by the winglet will partly contribute to the lift. Apart from having a positive impact on the effective span, the wing-winglet configuration will be able to generate more lift. As a result, the design lift coefficient of the planform can be reduced. Hence, from an aerodynamic perspective it is best to employ wingtip extension or to elongate the wing [19, 21, 25].

Although winglets improve the lift induced drag, it has a negative contribution to the parasitic drag due to the added wetted area. To conclude, winglets can reduce the induced drag, but great care has to be taken when designing the wing-winglet intersection to ensure that the interaction is minimized. Since winglets aim to minimize C_{D_i} , its effect is most pronounced during the low speed flight stages when the aircraft operates at large angles of attack [19, 25].

4.3. Design Considerations

The discussion on winglet design is not only dictated by aerodynamic phenomena, but also has to address structural effects. Most papers use the root bending moment as an indication for the change in wing weight [19, 20]. In their paper on multidisciplinary design of wings and wing tip devices, Ning and Kroo argued that the root bending moment did not account for the effects of chordwise changes in the planform, both in torsion and bending, and could, therefore, not be used as a good indicator for the wing structural weight [26]. They applied a semi-empirical method to estimate the wing weight. A more elaborate structural model was proposed by Elham and Van Tooren in their *Winglet Multi-Objective Shape Optimization* [21]. The quasi-analytical weight estimation method EMWET was utilized for their research and will also be incorporated in the current project.

Although there are numerous types of winglet configurations possible, not all are suited for the incorporation of control surfaces. To accommodate a control surface, the winglet is required to have a large section of limited curvature. The simplest of tip devices meeting the requirements are end-plates as featured on the AW-52 or as seen on H-tails. Another option is the more conventional single element winglet, either at an angle with the wing or blended. As the incorporation of lateral-directional control into a winglet yields a rather new and complex configuration, it was opted to design a single element canted winglet. It has already been found that the wing-winglet interaction is strong for nearly vertical surfaces and that blending ought to be applied to reduce these effects [24]. However, it is beyond the scope of the current project to include blending parameters into the optimization.



Figure 4.1: The Armstrong Whitworth AW-52 with end-plates for directional control - source: C.V. Murray, "Full-Scale Research on a Flying Wing"

4.4. Parametrization

In order to be able to perform a computer aided design optimization, the surface to be designed needs to be represented by a consistent set of independent variables. The number of variables should be limited to reduce the required computation time associated with the exploration of a vast design space. To minimize this 'curse of dimensionality' a number of assumptions are made.

- The airfoils used for the winglet are known and are not included in the optimization.
- The twist of both the root and tip of the winglet is known and is not included in the optimization.
- The hinge line of the control surface is at a constant percentage of the winglet chord.
- The winglet is aligned with the trailing edge of the wing.

In most winglet optimization studies the airfoils are kept out of the design space [19, 21, 26]. Studies either use the winglet airfoil prescribed by Whitcomb or the profile used at the wing tip. A similar limitation will be enforced during the proposed design optimization. The main reason being the added complexity of airfoil optimization and the sensitivity of the parameters. Although the airfoils could be included in the design process by either using CST-coefficients or the more physically intuitive PARSEC-representation, this would expand the design space by a minimum of 10 parameters per airfoil.

The second assumption is based on results from literature [8, 21, 27]. Studies indicate that, although twist enables designers to tweak the spanload distribution, the impact of this parameter is marginal. It was therefore opted to further reduce the design space to be able to adhere to the selected optimization strategy without the need to generate a large sample pool.

To accommodate a control surface a design variable needs to be added. Although the start and end position along the vertical surface is fixed, the location of the hinge line is not. It is assumed that the moveable is mounted on the aft spar of the vertical component. In general the spar is positioned at a fixed chordwise position, hence the third assumption.

Literature aiming to optimize a winglet aligns the non-planar component with the trailing edge. Although some studies researching the aerodynamic benefits of active winglets indicate that extending the winglet beyond the trailing could have a positive effect on the contraction of the wake, the program utilized for modelling the aircraft is unable to cope with such discontinuities [8]. Hence, it is therefore opted to adhere to a similar approach as was used in other winglet optimization studies.

With the listed assumptions, the design space to be explored comprise of the following variables:

- Winglet length (l_w)
- Cant angle (φ)
- Winglet sweep angle (Λ_w)
- Wingtip to winglet root chord ratio (cr_w)
- Taper ratio (λ_w)
- Chordwise hinge line position (H_w)

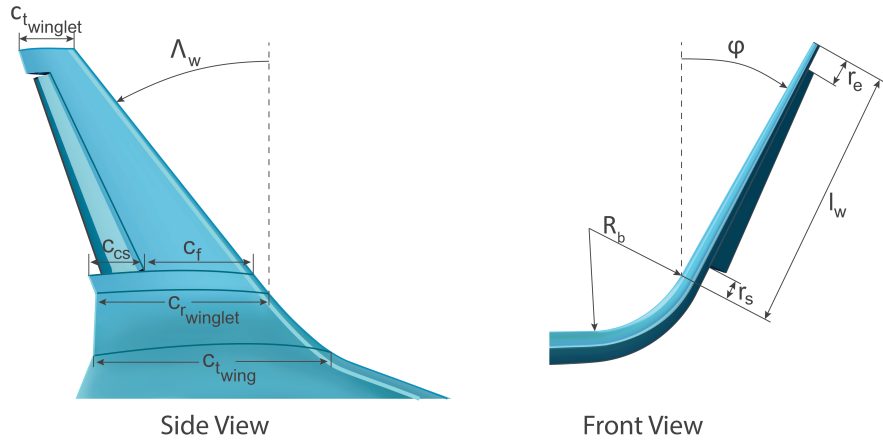


Figure 4.2: Parametric description of the rudder-incorporated winglet

A graphical representation of the variables used to describe the active winglet is presented in figure 4.2. Equations 4.2-4.4 are used to translate these variables to the non-dimensional parameters listed above. Apart from these parameters the figure also notes the blending radius R_b and the position of the rudder, r_s and r_e .

$$cr_w = \frac{c_{r_{winglet}}}{c_{t_{wing}}} \quad (4.2)$$

$$\lambda_w = \frac{c_{t_{winglet}}}{c_{r_{winglet}}} \quad (4.3)$$

$$H_w = \frac{c_{cs}}{c_{cs} + c_f} \quad (4.4)$$

The design space that is to be explored is listed in table 4.1. To ensure that a feasible solution would present itself, the design space was centred around the X-48B winglet configuration. Other bounds, such as the sweep angle, are based on aerodynamic limitations and requirements.

Table 4.1: Design space implemented in the winglet design program

	l_w [m]	φ [deg]	Λ_w [deg]	cr_w [-]	λ_w [-]	H_w [-]
upper bound	8.00	45.00	55.00	1.00	1.00	0.80
lower bound	3.00	1.00	25.00	0.55	0.30	0.80

5

Design Procedure

The requirements and design considerations listed in the previous chapters need to be linked to produce a method able to analyse and optimize the design of an active winglet. In this chapter the devised design methodology will be introduced and explained. The second part of the chapter will discuss the implementation of the procedure into a Matlab based program. The chapter is concluded by an introduction of the baseline aircraft.

5.1. Methodology

The type of optimization scheme that can be employed is dependent on the number of design variables and the formulated objectives. As the leading criterion is to provide adequate stability and control, the optimization scheme has to cope with the analysis and computation of the stability derivatives. Therefore, the selection of the optimization procedure is centred around the computation of these derivatives.

Design optimization of a winglet during the preliminary design stage is most often performed using a vortex lattice method. However, research into the ability of such a method to accurately establish the stability derivatives revealed a large discrepancy between the computed values and test data [7]. A higher fidelity potential flow solver, the 3-dimensional panel method, shows better results [28, 29]. Therefore it was opted to test and integrate such a 3D panel method. The commercial panel method VSAero is selected, as it is a multi-order panel method that implements an integral viscous boundary model [30]. Further information on the program can be found in Appendix B.2.

To establish the stability and control derivatives a single geometric configuration is to be analysed for a number of different attitudes, flight conditions, and control surface deflections. The required computation time to compute a complete data set corresponding to a single geometrical configuration is in the order of hours. It is to be noted that this time could be significantly reduced when a more efficient mesher is selected. To limit the required computation time, a Kriging response surface optimization strategy was selected. The method uses data entries for a number of sample points to construct a response surface. The accuracy of the surface is highly dependent on the number of sample points and the distribution of these points [31]. The best distribution is dependent on the behaviour of the design objective. As this behaviour is often unknown, it is nearly always opted for numerical problems to use equidistant sampling, such as the Latin Hypercube strategy. To ensure that the sampling results in a more evenly spaced grid the Latin Hypercube technique is connected to a min-max optimization [21, 31]. The min-max optimization maximizes the minimum distance between the entry points, creating a well distributed, space-filling, sampling pool.

The space-filling Latin Hypercube sampling strategy will be used to generate a number of winglet configurations. Each of the configurations will be analysed by VSAero to determine the stability and control derivatives. Implementation of these derivatives into the virtual flight test program Phalanx will provide information on crosswind landing and the handling quality levels of said configuration. The response surface of these characteristics will be used to limit the design space. The redefined design space will contain all solutions that yield adequate lateral-directional stability and control.

From within the viable design space the configuration will be identified that yield the best aerodynamic performance, weight properties and direct operating costs. To establish these parameters the aerodynamic loading of each of the configurations will be analysed by the class 2.5 wing weight estimation program EMWET [32]. The computed change in wing weight will produce the structural weight of the configuration, which will be substituted in a mission analysis scheme to derive the fuel weight and maximum take-off weight. Based on these results an estimate for the airframe cost can be established using reference [1]. The aircraft design and economic study by Liebeck et al. specifies a method to provide an indication of the direct operating cost during the early stages of design [33]. This method is used to ascertain the economic impact of each winglet configuration.

In the presented design methodology a distinction can be made between limiting and optimizing design objectives. The limiting objectives are directly related to the stability and control characteristics and are listed to be:

- The yawing moment coefficient due to sideslip needs to be positive
- A maximum winglet control surface deflection of 25 degrees during crosswind landing
- A minimum user-specified handling quality level for the asymmetric eigenmotions

The optimizing design objectives are secondary objectives that will be applied to the reduced design space. Related to the performance and cost of the aircraft, the optimizing objectives are given to be:

- Minimize structural weight
- Minimize MTOW
- Maximize lift over drag
- Minimize direct operating cost

5.2. Implementation

The introduced methodology is implemented in a flexible Matlab program that could be employed to design or explore various control surface configurations. The program can be decomposed into two parts with the aerodynamic solver VSAero as a natural boundary. This separation into pre-, and post-aerodynamic analysis will be used to discuss the functionalities and architecture of the program. A more detailed description of the individual components can be found in Appendix B.

It is to be noted that the program is separated into so-called *computation levels*. Within such a level all computations pertaining to a specific task are performed. Hence, most of the computation levels contain loops to analyse each of the winglet configurations. The different levels are indicated by the black lines in figure 5.1 and 5.2, which illustrates the workflow of the created design platform.

5.2.1. Pre-Aerodynamic Analysis

The pre-aerodynamic stage of the program is centred around the generation of the geometry and mesh needed to perform a VSAero analysis. The generation of the model and mesh is performed by a python based CAD program that requires detailed information on the geometry. Various computational modules have been constructed to facilitate the CAD program and incorporate it in the devised analysis and optimization platform. A schematic representation of the first stage is provided in figure 5.1.

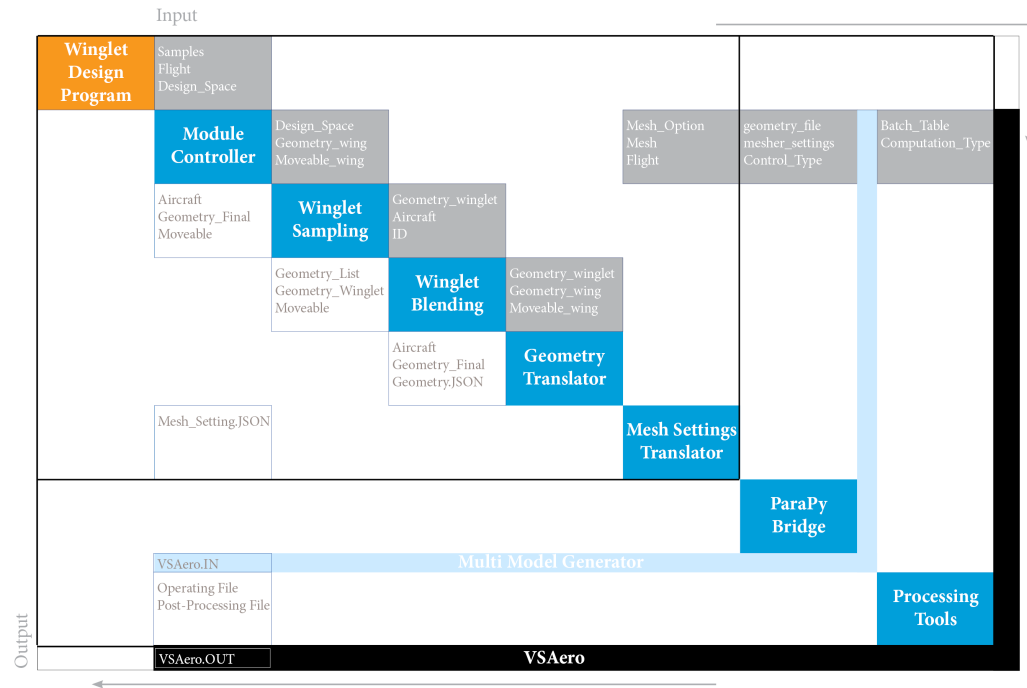


Figure 5.1: Overview of the program upto the aerodynamic analysis

At the heart of the *Winglet Design Program* is the *Module Controller*, which is called by a front-end script listing the design space and critical flight condition. All communication with the various functions and sub-programs is directed through this module, as it structures and prepares the data for analysis. Based on the predefined design space, the *Module Controller* initiates the generation of a specified number of winglet configurations. A Latin Hypercube sampling strategy is utilized to perform this task. The space-filling sampling method employs the previously mentioned min-max optimization to ensure a proper distribution [31, 34].

The geometric properties of each of the winglet configurations is passed on to the *Winglet Blending* module. This function employs a forth-order polynomial and a user-specified radius to create a smooth transition from wing to winglet. The continuity of the wing is an important criteria for the proprietary CAD program used to generate the model and mesh. Although the incorporation of winglet blending into the optimization process is out of scope, the module can easily be modified or replaced to test the influence of various blending methods.

Once the planform is described, the geometry needs to be translated for the python based CAD program known as the multi-model generator. This multi-model-generator, MMG, utilizes elementary building blocks to construct the 3-dimensional model. Each of these primitives can be initiated using so-called *.json*-files. These files contain information on the selected airfoils and twist distribution, as well as a description of the leading, and trailing edge. All information is computed by the Matlab program and is structured to be compatible with the MMG.

The final stage before calling the MMG is to produce a `.json` file pertaining to the mesh settings. Apart from details on the density of the grid, the document is to contain information on the type of computation. For the aerodynamic simulation it was opted to use the VSAero panel method with incorporated viscous models. The aerodynamic solver adheres to a card-based input system. Each card has a specified format and list a number of keywords related to the topic of said card. Based on these cards the user can select the mathematical solver, boundary condition, etc. More detail on the aerodynamic program will be presented in Appendix B.2.

Information on the geometry, mesh and control surfaces is passed on to the MMG, which generates a 3-dimensional CAD model. Connected to the MMG is the open source software package *Salomé*. *Salomé* is able to construct a variety of surface grids, based on a high-level meshing strategy embedded in the MMG. The MMG combines the resulting grid with data on the selected aerodynamic computation scheme to form the input file for VSAero.

A faculty server dedicated to high performance computations and the use of commercial packages was employed to access VSAero. Since the server requires a secure link, the process was not included in the program and requires some manual steps. Rather than having to run the files individually, a pre-processing script is created to aid the user. The script also generates a number of configuration files that is used to process the data once the aerodynamic analysis has been performed.

5.2.2. Post-Aerodynamic Analysis

The aerodynamic analysis produces a number of output files of which the `.OUT` is the most important. The document contains all information regarding the pressure distribution, velocity profiles, and boundary layer behaviour. These files form the starting point of the second stage, which is depicted in figure 5.2.

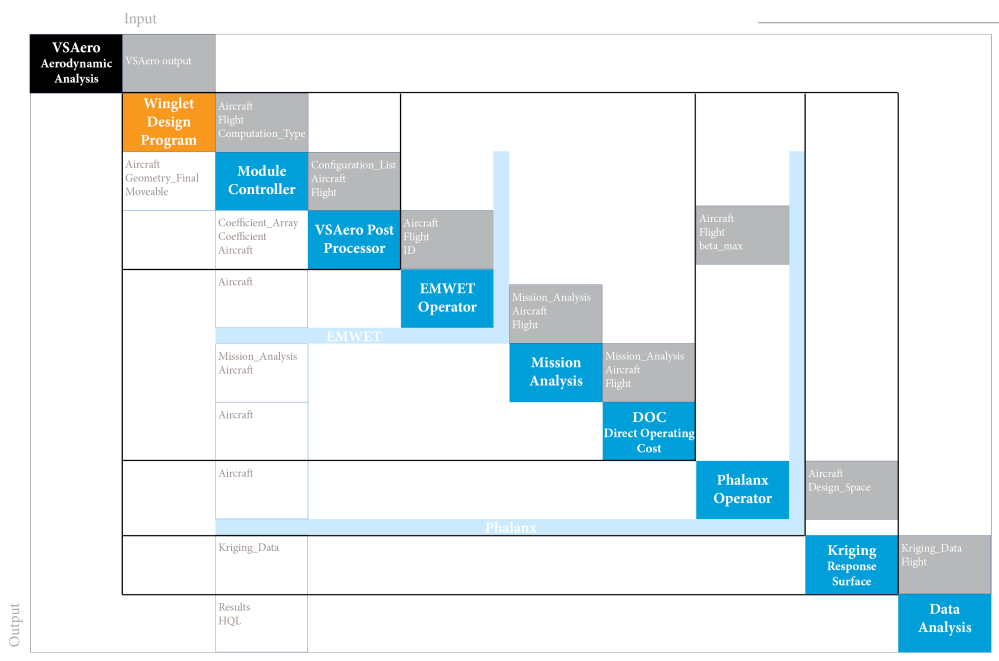


Figure 5.2: Overview of the program after the aerodynamic analysis

The VSAero Post-Processor module scans the aerodynamic output to establish the forces and moments coefficients. However, to compute the stability and control derivatives, each geometric configuration is analysed for slightly different attitudes and flight conditions. Each of these alterations can be identified from the name of the document. This unique nomenclature is used to sort all coefficients to establish the stability and control derivatives corresponding to a specific sample. Apart from the coefficients, the spanload and local pitching moments are computed and connected to the *Aircraft* struct, containing all information on the configuration.

The next stage is to determine the change in the structural wing weight due to the implementation of a winglet. It is to be noted that the aircraft is decomposed into a centre body and outer wings, of which only the latter will be analysed. The rationale behind this is that the centre body is not only subject to torsion and bending, but it also has to cope with the more complex loading of the pressure cabin. The outer wing is defined to start at 8.0 m from the line of symmetry and can be considered to be similar to a conventional wing.

The quasi-analytical structural weight estimation program EMWET is employed to establish the wing weight [32]. EMWET requires an input file specifying the geometry and material properties of the wing and a second file that lists the forces and moments. The method utilizes the geometry to derive the general structural composition of the wing. An iterative process is then initiated to size the individual components by computing the local bending moments and shear stresses. By adhering to an iterative computation scheme, EMWET is able account for load relief effects caused by the weight of the system.

The change in wing weight is used in the *Mission Analysis* module to determine the contribution of the various weight components. The scheme comprises of a classical class-I weight estimation that uses fuel fractions and a fixed structural weight ratio [1, 2]. To account for the change in wing weight, the ratio of the operating empty weight to W_0 is calculated for each configuration. For the fuel intensive flight stages, such as cruise and loiter, the method requires information on the aerodynamic performance and specific fuel consumption, SFC. Data on the SFC is to be implemented by the user, while the aerodynamic performance is directly obtained from VSAero. As the baseline aircraft operates on both conventional aviation fuel and LNG, the weight of the cryogenic tanks is to be taken into account. Rather than sizing the actual fuel tanks, a fuel tank density is derived based on a research study by NASA [35]. The obtained density was successfully validated against commercially available space-grade cryogenic tanks. The resulting iterative process produces the operating empty weight (*OEW*), W_0 and the required fuel weight, W_f .

Based on the weight decomposition and operating conditions the direct operating cost, DOC, can be estimated. This universally accepted method was first published in 1944 by the Air Transport Association of America, ATAA. The method was progressively modified and updated to reflect the economic breakdown of modern airliners [33]. The scheme requires an estimate of the airframe cost. An estimation method to compute this parameter is provided in reference [1]. A detailed overview of the computation scheme can be found in Appendix B.4.

As all optimization objectives have been determined, the focus shifts towards the limiting objectives. To analyse these stability characteristics, the virtual test flight program Phalanx is connected. The program was developed as a non-linear, multi-body flight dynamics model, compatible with multi-disciplinary design procedures. Further information on this virtual test flight program can be found in Appendix B.5. A general description of the aircraft and the implementation of the computed stability and control derivatives initiates the automatic generation of the flight mechanics model. Before Phalanx is able to derive the behaviour of the aircraft, a trimmed condition is to be established. The program is scripted to first determine the equilibrium condition during crosswind landing. This yields

the required rudder deflection, which is defined as one of the limiting criteria. A second trim run is initiated to establish the trimmed condition for a symmetric landing approach that forms the starting point for the stability analysis. The analysis provides information on the lateral-directional characteristics of a given geometric configuration. To create a more flexible system in which the user is not limited to the design of the asymmetrically deflected control surfaces, the winglet design program also gathers the information on the longitudinal motions. However, it is to be noted that for a proper analysis of the symmetric behaviour, the stability derivatives need to be established at the flight condition of interest. Since the dynamic pressure and Reynolds number has a profound impact on the aerodynamic properties of the vehicle, the stability derivatives will differ for various flight conditions. Although this will influence the behaviour of both the symmetric, and asymmetric characteristics, literature indicates that the flight condition only has a marginal impact on the lateral-directional properties [13]. The limited influence can be attributed to the aerodynamic symmetry present in most aircraft. As the asymmetric motions are largely concerned with the offset in aerodynamic loading, the influence of the change in dynamic pressure and the shift in local centre of pressure is limited.

Before the response surface of the different design objectives can be constructed, the data needs to be restructured. The geometry of each winglet configuration is collected in a single matrix that is used to correlate the output of the objectives to a specific location within the 6-dimensional design space. The Kriging response surface strategy assumes a stochastic relation between the output of entry nodes. To estimate the objective parameters at untried locations, the method employs various regression, and correlation models. These models attempt to capture the behaviour of the system by linking neighbouring points. The manner in which these points are connected is defined by a n^{th} -order polynomial regression model, while the strength and range of each point is given by the correlation model. An additional variable is introduced that describes the dominance of the different design variables. Using a large variety of sample points, the program is able to derive this so-called *Kriging predictor* by minimizing the least squares error. Once the Kriging model is defined, it can be superimposed on a grid that spans the entire design space. It was opted to use an equidistant grid, resulting in a total of 117649 unique winglet configurations. Due to memory limitations encoded in Matlab it was not possible to employ a grid with a higher density.

The output, as obtained from the Kriging module, is passed on to the data analysis section. This section translates the eigenmotion characteristics into HQL by comparing them to the criteria listed in table 3.1 and 3.2. The output is gathered to construct a matrix dedicated to the HQL of the asymmetric eigenmotions. It is to be noted that the HQL matrix can easily be expanded to include the symmetric motions.

Prior to optimizing the winglet, the design space is analysed to establish all configurations that yield a stable and controllable platform. Therefore, the response surfaces related to the HQL are compared to the minimum requirements specified by the user. If a configuration does not meet the requirements, the objective value is set to zero. A similar approach is used to establish whether the rudder deflection and $C_{n\beta}$ are within bounds. The resulting matrix is merged with the geometry and optimizing objectives, after which all rows containing zeros are removed from the system. Both the original and reduced matrices are flushed to the results directory for further analysis. These matrices allows the user to identify a possible correlation between an individual design variable and the behaviour of a design objective. This could produce valuable information for future designs.

The reduced matrix, consisting of all viable solutions, is further analysed. The optimized winglet configurations corresponding to an individual design objective is passed on to the results directory. All relevant data is gathered, structured and plotted for further analysis.

5.3. Baseline Aircraft

For the analysis of the design process and program the Advanced Hybrid Engine for Aircraft Development, AHEAD, multi-fuel blended wing body aircraft was selected as a baseline. The AHEAD consortium recognizes the need for a step change in both aircraft and engine configuration to reduce the environmental footprint of aviation. The production of CO_2 is directly related to the chemical process of transforming fuel into energy. Therefore, the AHEAD project proposes the use of cryogenic fuels such as LNG and LH₂, which have a lower carbon-dioxide signature. As indicated in Chapter 2, implementation of these fuels pose a significant problem for the classical tube-and-wing aircraft [12]. The reason for this is the relative low volumetric density, which is defined as the energy the fuel can generate per litre (VED [MJ/l_t]). Analysis of the theoretical relative fuel mass and volume as a function of the cryogenic fuel fraction for a given mission suggests the use of a multi-fuel architecture. Therefore the AHEAD consortium is developing a dual-fuel engine that employs both LNG and conventional aviation fuel simultaneously [36].

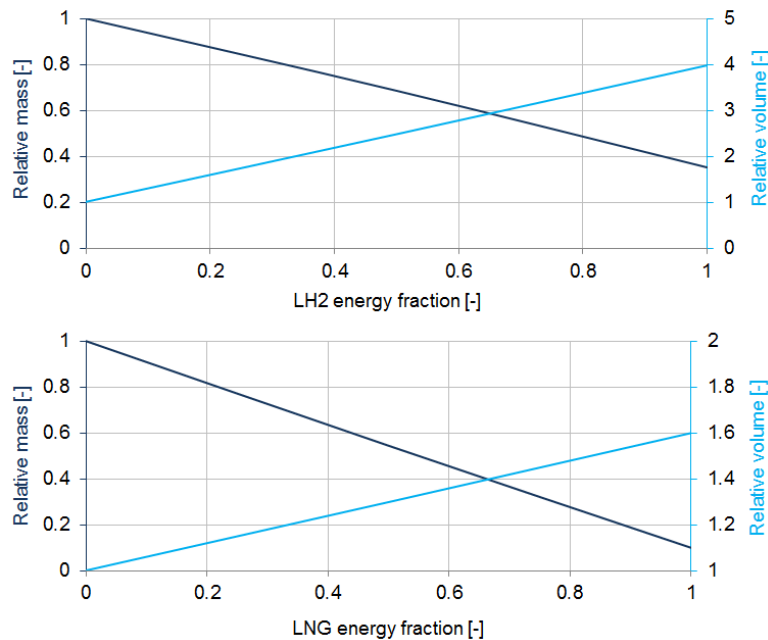


Figure 5.3: Theoretical fuel mass and volume as a function of the cryogenic fuel fraction

In the fall of 2011 a group of ten students were tasked to conceptually design a multi-fuel BWB that incorporates the AHEAD hybrid engines. The long range aircraft was to be able to accommodate 300 passengers on its 14000 km journey. The project yielded a slender hybrid body that featured a canard for longitudinal stability and control. The study showed great potential, but was unable to address all aspects due to time constraints. Based on the findings of the conceptual design a new project was initialized to progress the design to the preliminary stage. Although the general philosophy of the slender body design was honoured, the planform was significantly modified to yield a more feasible design. It was envisioned that the aircraft would be equipped with active winglets for yaw control. However, the complexity of the design process and the limited availability of computational models yielded a conceptual design of these components.

My knowledge of the aircraft and involvement in the various design stages made the AHEAD multi-fuel hybrid body an ideal option as a baseline aircraft. It had already been stipulated in the previous section that the abilities of the mesher currently connected to the MMG is limited. Hence a simplified representation of the AHEAD aircraft is used in the design program. The implemented geometry models the aircraft without canard and engines. As the research is investigating the effect of winglets on the lateral-directional

stability and control, it is expected that the cancellation of the canard has limited influence on the design. However, it is to be noted that a virtual moment about the pitch axis is to be applied to account for the canard in order to obtain a trimmable aircraft. The inability to account for the engines will have a more profound impact. Although the hybrid engines are partly embedded in the fuselage, the components will still have a contribution to the generated side-force.

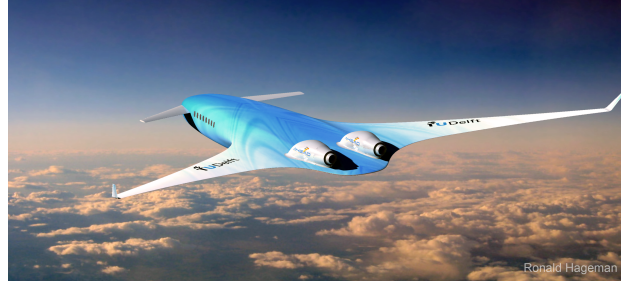


Figure 5.4: An visualization of an older version of the AHEAD multi-fuel BWB

Simplification of the aircraft also entails that no high-lift devices are modelled. As the BWB is analysed at landing conditions, empirical methods are employed to account for the change in lift and drag due to the deployment of slats and flaps [1]. The increase in lift at zero angle of attack can be estimated using equation 5.1. The equation utilizes the change in zero lift angle described by equation 5.2.

$$\Delta C_{L_0} = C_{L\alpha} \cdot \Delta \alpha_{L=0} \quad (5.1)$$

$$\Delta \alpha_{L=0} = \Delta \alpha_{l=0} \frac{S_{flapped}}{S_{ref}} \delta_{HL} \quad (5.2)$$

In the equation $\Delta \alpha_{l=0}$ represents the 2-dimensional change in zero lift α , which is set to 5 degrees. A moderate deflection angle of 10 degrees was defined as the aircraft already has to cope with a nose-down moment. Extending the leading and trailing edge also influences the slope of the lift-curve. The resulting change in $C_{L\alpha}$ is difficult to predict and was therefore only slightly increased.

$$\Delta C_{D_{HL}} = 0.0023 \frac{b_{flapped}}{b} \delta_{HL} \quad (5.3)$$

An estimation method for the drag was also presented in reference [1]. The method provides a crude estimate by using the deflection angle and flapped span to wing span ratio, equation 5.2. As each of these simplifications will have an influence on the stability and control, it is recommended that the design process is repeated once the mesher has reached a more mature stage.

The planform of the multi-fuel hybrid body can be characterized by the slender centre body and the aft position of the outer wings. The relative large surface area, as compared to conventional aircraft, enables the BWB to operate at a design lift coefficient of 0.155. This allowed designers to employ a modified version of the NACA/Langley N0011SC supercritical airfoil that possesses excellent aerodynamic and volumetric characteristics. A more detailed description of the aircraft can be found in Appendix A.

6

Validation

At the heart of the devised design methodology is the aerodynamic solver VSAero. Despite the fact that the winglet design tool employs a number of programs and methods, the only component that still need validating is this first order panel method. Two research studies have been found that describe the capabilities and limitations of VSAero [28, 29]. These papers, discussing a small business jet and the Fokker 100, will be used to validate the aerodynamic platform. In this chapter the research by Nathman, McComas and Wei is summarized and used to demonstrate the accuracy of VSAero. First, the computational models and the data used for comparison will be introduced, followed by an analysis of the clean configuration. The chapter is concluded by a brief overview of the impact of the various methods available to model the control surfaces.

6.1. Description of Computational Model and Data

Both studies simulate the aircraft during low speed flight stages, acknowledging the limitations of potential flow theory. The selected flight conditions and the models used during the computations will be discussed in this section.

6.1.1. Learjet Model 23

In October 1964 a small business jet entered service. With a wing span of 10.84 m the aircraft, designated Learjet Model 23, has a range of 2950 km and a capacity of upto 6 passengers. At that time, the design process of most small aircraft include limited wind-tunnel data. In combination with the often qualitative rather than quantitative flight tests, the designer obtained little feedback on the accuracy of the computed predictions [37]. In 1971 a full-scale windtunnel test at the NASA Ames 40 x 80 foot research facility was conducted to aid the designers. The research investigated the aerodynamic behaviour of the business jet at two Reynolds numbers, corresponding to a velocity of 27.8 m/s and 59.0 m/s. During the windtunnel tests the engines were replaced by flow-through nacelles that mimic the idle condition of the two General Electric turbojets.

The data collected by NASA provided detailed information on the forces and moments acting on the aircraft. In 2008 this data was utilized to determine the capabilities and limitations of both VSAero and a vortex lattice method [28]. In this chapter only the data pertaining to the VSAero computations of the 59.0 m/s simulations are included. For the analysis Nathman and McComas accurately modelled the twin engine aircraft, featuring its characteristic tip-tanks with lateral fins. The model, presented in figure 6.1, contains a total of 7178 panels and employs similar flow-through nacelles. Further information on the matrix solver, selected boundary layer settings, wake panels, and number of iterations is not listed in the paper.

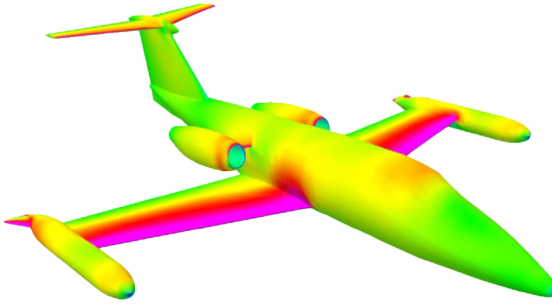


Figure 6.1: Panel method representation of the Learjet Model 23 - source: J.K. Nathman and A. McComas, "Comparison of Stability and Control Calculations from Vortex Lattice and Panel Methods" [28]

6.1.2. Fokker 100

As a redesign of the successful F-28 Fellowship, the Fokker 100 entered service early April 1988. The regional jet of Dutch origin has a seating capacity of approximately 100 passengers. Powered by two aft mounted Rolls-Royce turbofan engines, the aircraft has a range of 3170 km. The Fokker 100 had been selected by J.H. Wei as a baseline aircraft for the validation of VSAero and the multi-model-generator [29]. Since limited information on the geometric properties of the vehicle is available, he resorted to translating technical drawings. Although they produced an accurate description of the planform and layout, little information was provided regarding the airfoils and twist distribution.

The research by Wei focussed on parametric modelling of aircraft, aiming to establish the stability and control characteristics. As part of his thesis he created the latest version of the multi-model-generator, Appendix B.1. In the previous chapter it had already been indicated that the capabilities of the software package are currently limited due to the embedded mesh generator. Therefore, a simplified model of the Fokker 100 was employed to validate the aerodynamic solver. A render of the panel method representation is provided in figure 6.2. The simplification leads to the cancellation of the following features: nacelles; pylons; dorsal fin; wingbox fairing. The influence of these aspects on the aerodynamic performance is recognized and is included in the discussion presented in reference [29].

For the validation, a hybrid mesh is used to discretize the configuration into 9493 body panels and 10642 wake panels. As a result, most of the aircraft can be modelled using a structured, quadrilateral grid. Due to the large number of panels and complex geometry, it was opted to employ the iterative Lapack BGS scheme. For more detailed information on the performed panel method computations, the reader is referred to reference [29].

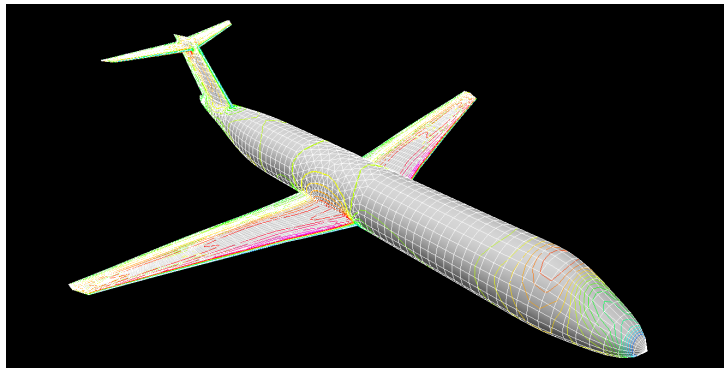


Figure 6.2: Panel method representation of the Fokker 100

The data used for validating the VSAero computations is based on windtunnel tests that correspond to a velocity of 98.6 m/s and an altitude of 3000 m. A summary of the results will be presented in the remainder of this chapter.

6.2. Analysis of the Clean Configuration

The validation of the clean configuration will mainly focus on determining the program's ability to derive the lateral-directional characteristics. While a good representation of this behaviour is imperative to the design of a winglet, the aerodynamic parameters C_L and C_D will be analysed first. Both research studies investigate the ability of the aerodynamic solver to establish the lift at different angles of attack. Their results, depicted in figure 6.3, demonstrate the accuracy of the panel method. However, it is to be noted that both simulations only analyse the linear part of the C_L -curve.

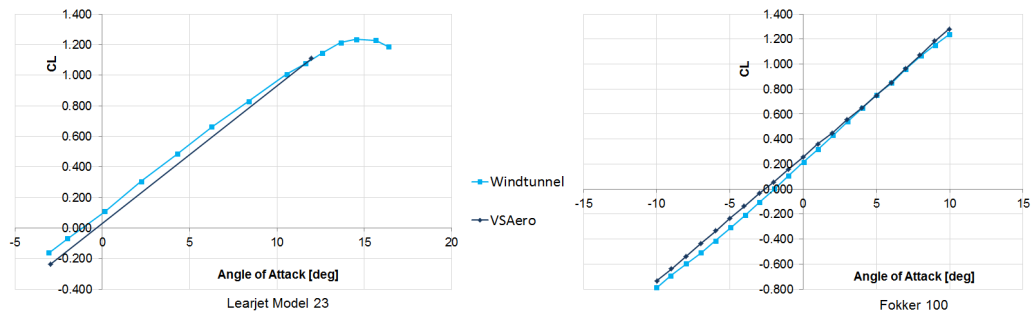


Figure 6.3: Comparison of the lift coefficient

The thesis by Wei also investigates the drag estimate, figure 6.4. Despite the fact that the drag is underpredicted, VSAero appears to be able to capture the behaviour of C_D rather well. The discrepancy in drag can be attributed to the simplification of the model. However, at this stage it is impossible to state whether the deviation is caused entirely by the absence of engines and nacelles, or in some part by the methods used by the program itself.

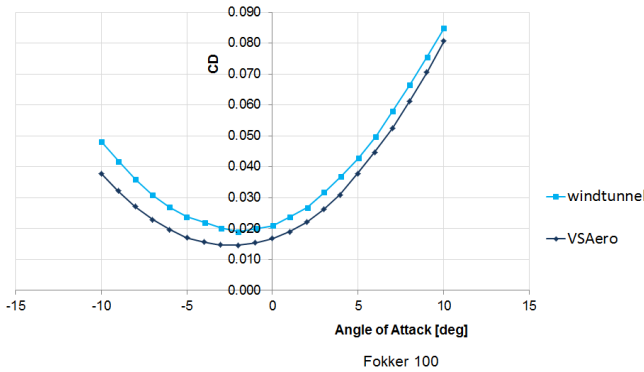


Figure 6.4: Comparison of the drag coefficient

The next parameter that is to be analysed is the side-force coefficient. The VSAero results for both aircraft, figure 6.5, provide a good estimation of C_Y for small angles of sideslip. For larger β the estimates start to deviate and demonstrate more irregular behaviour. Wei attributes these instabilities to improper modelling of the root chord wake line [29]. As a result the wake of the wing will partially intersect the aft part of the fuselage. If these instabilities are indeed caused by the interaction between the wake and fuselage, better results are to be expected for the BWB simulations. Wei also notes that some discrepancies found for the lateral force and yawing moment are due to the absent dorsal fin.

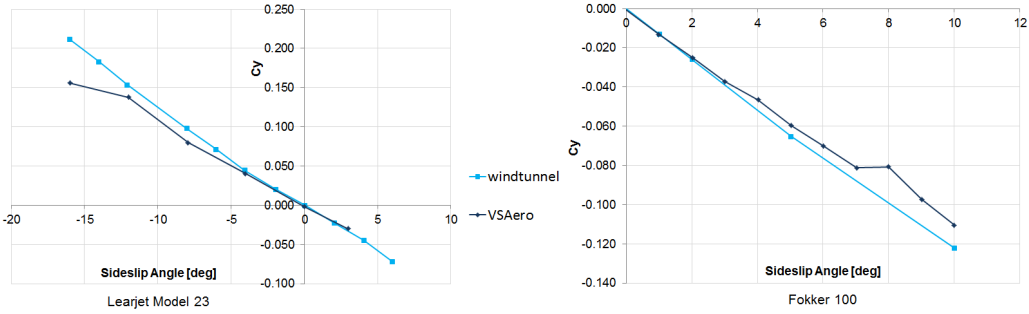


Figure 6.5: Comparison of the side-force coefficient

The results by Wei with respect to C_n demonstrate similar characteristics. However, comparison to the Learjet computations indicates a larger error. Due to the relative small size of the parameter it is more sensitive to minor pressure variations. These variations could be caused by a difference in the level of convergence. Despite these discrepancies, the plots presented in figure 6.6 demonstrate a sufficient level of accuracy.

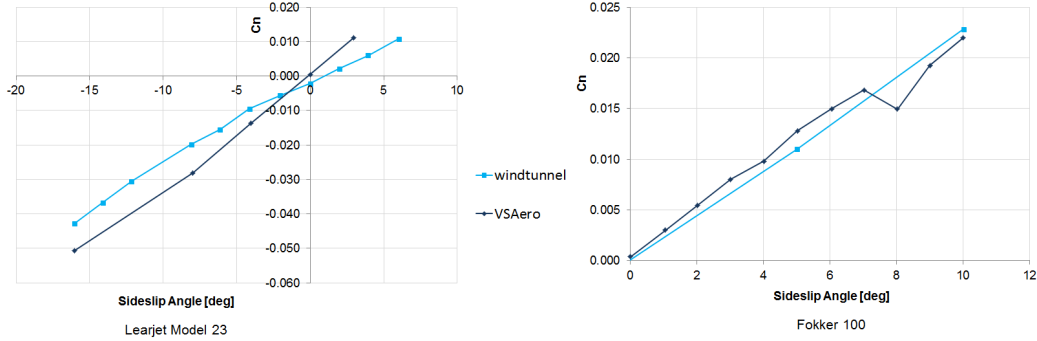


Figure 6.6: Comparison of the yawing-moment coefficient

The final parameter that is to be analysed, is the rolling moment initiated by a sideslipping motion. Only data with respect to the Fokker 100 is available. The results, depicted in figure 6.7, show similar instabilities as were found for C_n and C_Y . Apart from this irregularity that occurs at approximately 7.0 degrees, the trend appears to be slowly diverging. Since the linearised equations of motion will be utilized to ascertain the stability characteristics, the divergent behaviour will not deteriorate the accuracy of the scheme.

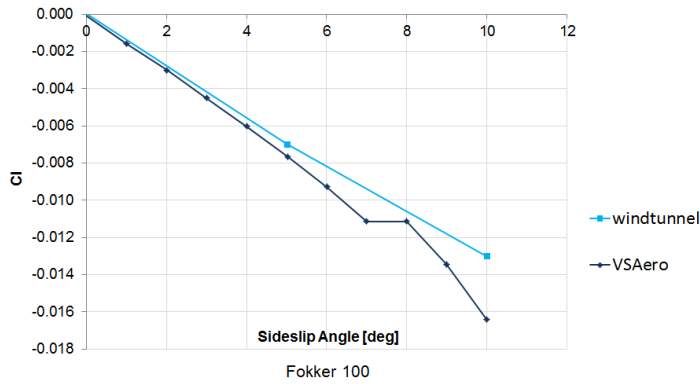


Figure 6.7: Comparison of the rolling-moment coefficient

To conclude, VSAero was found to be sufficiently accurate in establishing the various aerodynamic properties, especially for relative small angles of attack and sideslip. The limitations of the program seems to stem from the complex configuration and the resulting challenges of modelling the wake. As the simplified BWB consists of a single element, the instabilities ought to be minimized. Therefore, it is expected that the aircraft can still be analysed at larger angles of sideslip.

6.3. Impact of Control Surface Options

The MMG features 3 options to model control surfaces. Each of these models will be briefly introduced and analysed to determine the accuracy of the different representations. The 3 control surface models are listed to be:

- VSAERO normal rotation
- not slotted-gap-transition surface
- not slotted-gap

A graphical representation of each of the methods is provided in figure 6.8. The first option mathematically rotates the orientation of the moveable's normal vector to mimic a deflection. The other methods physically rotate the control surface to change the orientation of the flow. In the first of these two options, the gap created between the wing and the deflected surface is closed to prevent air from slipping through. The final option models the surface without closing the opening.

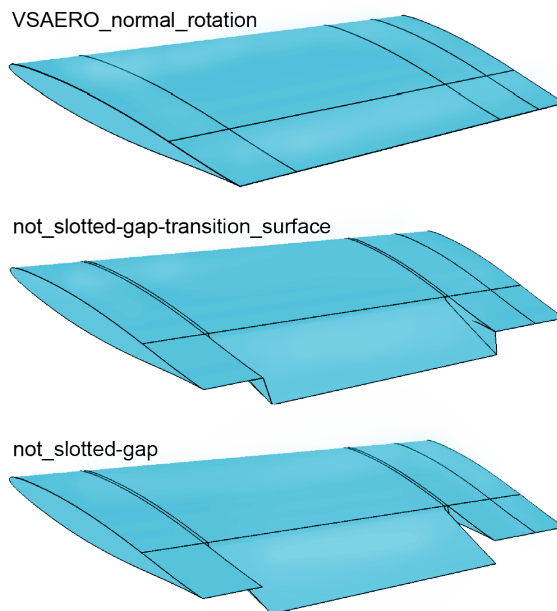


Figure 6.8: Multi-Model-Generator control surface options - source: J.H. Wei, "Parametric modelling for determining aircraft stability & control derivatives" [29]

It was found that last of the three options produced significant increases in drag. Due to the opening, a low pressure area is created in the vicinity of the gap. Since VSAero is unable to properly account for viscosity, this will lead to unrealistic velocities. Therefore, reference [29] considers the *not slotted-gap* a non-viable option and will not be included in the analysis.

For small deflection angles, there was virtually no difference between the two remaining methods. Beyond δ equals 20.0 degrees the deviations become more distinguishable. Figure 6.9 illustrates a shift of the lift-drag polar for a 20.0 degrees aileron deflection. The additional drag, associated with the *transition surface* option, is explained by investigating the pressure distribution over the airfoil, figure 6.10. The *normal rotation* shows a relative sharp pressure peak that is positioned just forward of the control surface, while the pressure peak of the *transition surface* is located on the moveable. Hence, the forces generated by the secondary peak will have a different orientation. This translates to an increase in induced drag for the *transition surface*.

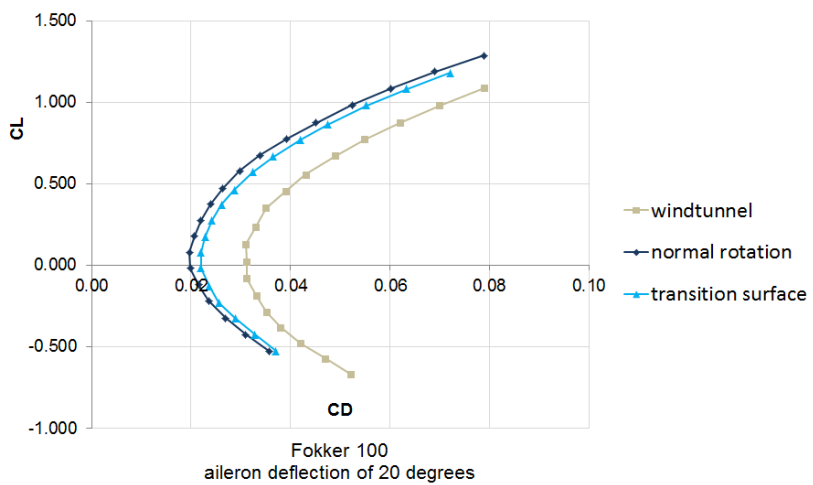


Figure 6.9: Aerodynamic comparison of the different control surface models

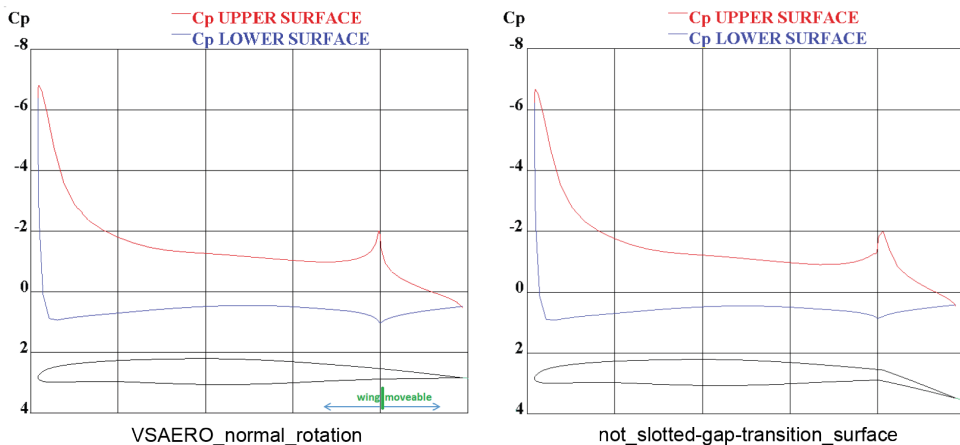


Figure 6.10: Pressure distribution comparison for a 20.0 degrees control surface deflection - source: J.H. Wei, "Parametric modelling for determining aircraft stability & control derivatives" [29]

Both methods have also been tested for a rudder deflection of 33.0 degrees, figure 6.11. Since C_Y , C_l , and C_n all show a similar pattern, it is opted to only include the plot for the yawing-moment. The image illustrates the error to be smallest for the *transition surface*. However, the *normal rotation* is better able to capture the general trend.

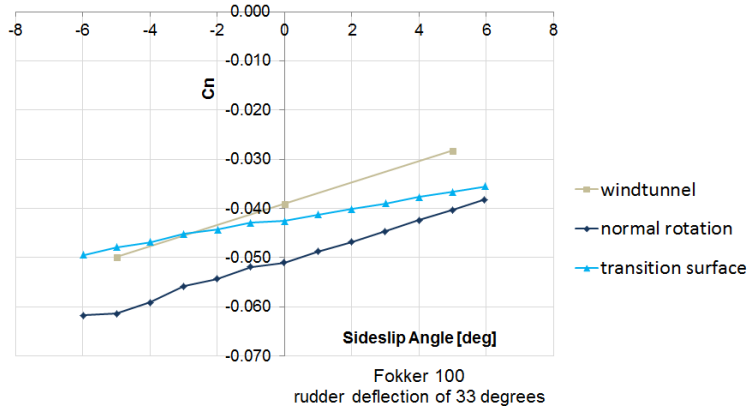


Figure 6.11: Comparison of the different control surface models on the yawing-moment coefficient

Comparison between the two control surface representations, indicate that the models are nearly identical. The main difference between the models is caused by the variation in shape and location of the secondary suction peak. This influences the contribution to the lift induced drag. However, this effect is only visible at relative large deflection angles. Comparison of the rudder performance at a deflection angle of 33.0 degrees reveals that both models produce different curves. While the error of the *transition surface* is smallest, the *normal rotation* is better able to capture the behaviour of the various lateral-directional parameters. Therefore, it is opted to employ the *normal rotation* representation during the remainder of the project.



Sensitivity Study

The sensitivity study comprises of two parts. The first part investigates the accuracy of various mesh sizes and compares two mathematical solvers. The analysis will be used to select a grid size and mathematical solver that is able to quickly and accurately compute the aerodynamic properties of the aircraft. In the second part a variety of options will be tested to find an appropriate setting for the Kriging response surface methodology.

7.1. Aerodynamic Analysis

The required computational time of the program is largely dependent on the generation of the VSAero input files and the aerodynamic analysis. While the user has little influence on the computational time to generate the input files, the user has a significant impact on the VSAero calculations. By minimizing the grid size and selecting an appropriate mathematical solver the computation time can be limited. In order to establish the impact of both grid size and solver a sensitivity study is performed.

Literature indicates that the direct aerodynamic solver *Lapack* is the most accurate and robust method to solve the flow tangency condition [30]. Therefore, the Lapack scheme, in combination with a very fine grid, will be used as a baseline to investigate a variety of mesh sizes. These mesh sizes are centred around the by VSAero proposed properties. The density of the grid can be defined by the number of nodes in chordwise direction and the spanwise pitch. As the change in lift distribution is rather gradual in spanwise direction the pitch size can be relatively large, compared to its chordwise counterpart. The number of chordwise nodes needs to be sufficient to accurately capture the suction peak and the behaviour of the boundary layer. If the number of nodes is too small the effect of the suction peak is averaged out. However, increasing the density beyond a given point does not add to the accuracy of the scheme and will only increase the computation time. The selected number of nodes for the sensitivity study are: 20, 30, 40, 50, and 60. It is to be noted that, due to the architecture of the MMG, the wing is decomposed in an upper and lower surface, each corresponding to an individual mesh. The spanwise pitch that is tested is listed to be: 1800, 1600, 1400, 1200, and 1000. As the spanwise distribution is defined as a pitch, increasing this value would yield a lower grid density. The results of the sensitivity study are tabulated in table 7.1.

As noted, literature has found the *Lapack* solver to be most accurate and robust. However, the scheme is less suited for configurations with a considerable number of computation nodes. Research indicates that an iterative solver could be more efficient in these scenarios. The fastest iterative solver embedded in VSAero is termed *Blocked GS*, with GS being the acronym for *Gauss-Seidel* [30]. A similar grid analysis was performed using this method, its results are presented in table 7.2.

Table 7.1: Grid sensitivity study for the Lapack solver

LAPACK						
CL	20	30	40	50	60	
1000	4.70%	1.32%	2.19%	1.83%	0.14%	
1200	4.56%	1.29%	2.05%	1.49%	0.25%	
1400	4.36%	1.46%	2.36%	2.00%	0.62%	
1600	4.67%	0.67%	1.97%	2.11%	0.90%	
1800	3.68%	0.06%	2.19%	1.80%	0.65%	
CD	20	30	40	50	60	
1000	5.40%	0.22%	1.05%	1.05%	0.45%	
1200	5.02%	0.45%	0.67%	0.82%	0.67%	
1400	4.80%	0.30%	1.27%	0.97%	1.35%	
1600	5.10%	1.42%	0.45%	1.12%	2.02%	
1800	3.07%	2.70%	0.60%	0.60%	1.95%	
CM	20	30	40	50	60	
1000	8.26%	1.07%	2.91%	2.75%	0.61%	
1200	8.11%	1.07%	2.75%	2.14%	0.84%	
1400	7.80%	1.30%	3.21%	2.91%	1.45%	
1600	8.19%	0.08%	2.68%	3.14%	2.07%	
1800	6.66%	0.69%	2.98%	2.52%	1.22%	

Table 7.2: Grid sensitivity study for the Blocked GS solver

Blocked GS						
CL	20	30	40	50	60	
1000	4.61%	1.66%	2.50%	2.42%	0.20%	
1200	4.70%	1.18%	2.92%	1.88%	0.31%	
1400	4.58%	1.12%	3.07%	2.28%	0.03%	
1600	4.36%	0.65%	2.92%	2.36%	0.48%	
1800	4.36%	0.87%	2.73%	2.50%	1.38%	
CD	20	30	40	50	60	
1000	5.17%	0.67%	1.50%	1.65%	0.60%	
1200	5.47%	0.37%	1.95%	1.12%	1.12%	
1400	5.32%	0.60%	2.47%	1.42%	1.12%	
1600	4.35%	1.35%	1.95%	1.35%	1.50%	
1800	4.20%	0.60%	1.42%	1.42%	0.00%	
CM	20	30	40	50	60	
1000	8.11%	1.61%	3.37%	3.44%	0.69%	
1200	8.26%	0.92%	3.98%	2.68%	0.84%	
1400	8.03%	0.77%	4.21%	3.21%	0.23%	
1600	7.73%	0.08%	3.98%	3.44%	1.15%	
1800	7.65%	0.54%	3.75%	3.60%	2.07%	

The aim of the aerodynamic analysis is to obtain a lift coefficient with a deviation of less than 1.0%, while minimizing the error for C_D , with a maximum of 2.0%. From the results it can be concluded that the a minimum of 30 chordwise points per surface is required to properly reflect the pressure distribution. A second observation is the variation of the accuracy between 30 and 40 nodes. The lower estimated error of the coarser grid can be explained by the apparent inability of the mesh to cope with the large pressure gradient at the leading edge. As the mesh only has a limited number of computation nodes, the peak of the pressure distribution is under-predicted. However, the width of this peak is overestimated due to the same principle of averages that caused the deviation in peak strength. From the simulations it seems that the error due to the coarseness of the mesh is averaged out.

The tables also show that the accuracy of both methods are compatible. However, analysis of the required computational time illustrate a significant time advantage when opting for the iterative Blocked GS solver. An overview of the computational time as a function of the mesh size can be found in figure 7.1.

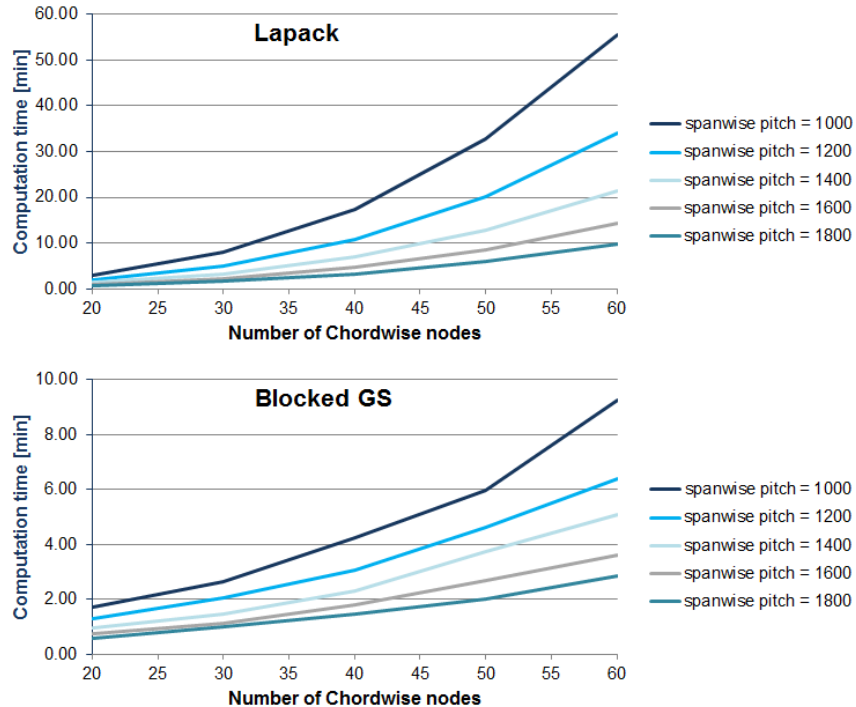


Figure 7.1: Computation time versus grid size for both tested solvers

Based on the presented accuracies and the corresponding computation power a mesh size of 30×1600 was selected. Although the 30×1800 grid seems to better represent the drag, the grid was discarded due to the transient behaviour during convergence.

7.2. Response Surface Models

A response surface strategy utilizes the information of sample points to predict the behaviour at off-site local. It does so by connecting neighbouring points and searching for a trend between these data samples, the so-called *regression*. The strength of this relation, or the realm of influence, is determined by a correlation model [31]. The employed response surface methodology provides a number of options that correspond to a specific regression and correlation scheme. Each of these models is tested to establish the accuracy of the response surface to determine the best strategy. The regression models are defined as an n^{th} -order polynomial, while the correlation models include: [34]

- Exponential
- Gaussian
- Linear
- Spherical
- Cubic
- Spline

The winglet design program is used to generate and analyse 200 unique winglet configurations. Each configuration produces information on both the limiting and optimizing objectives. The data needed to establish the stability and control characteristics is vast and requires multiple surfaces to generate. Hence, a selection needs to be made to test the various models. For the sensitivity study the optimizing objectives are selected, which are supplemented by two stability parameters. Amongst these parameters is the yawing moment coefficient due to sideslip, as it is one of the limiting criteria. The second parameter is the yawing moment coefficient due to rudder deflection, $C_{n_{\delta_r}}$. This parameter was selected as it is one of the leading parameters during rudder design. For each of these parameters a response surface model is constructed based on the input of the 200 samples. The average error of the model was determined by comparing the surface to 40 randomly generated winglets. Apart from the computing the average error, the study also lists the error of the individual configuration to derive the standard deviation. The process was repeated for all regression and correlation models. Detailed information on these models can be found in reference [34].

Chapter 5 indicated that the accuracy of a response surface is dependent on the number of sample points and the behaviour of the system one wants to identify. The first stage of the sensitivity study pertains to modelling the underlying behaviour of the system. To analyse the impact of the number of data entries the exercise is repeated for a data set of 400 geometries. The results of a selected number of correlation models are presented in tables 7.3 and 7.4. An overview of all results can be found in Appendix C.1.

Table 7.3: Accuracy of the Gaussian correlation model on the various parameters

Correlation model: Gaussian							
Samples: 200		$C_{n_{\beta}}$	$C_{n_{\delta_r}}$	LD	W_{wing}	MTOW	DOC
Polynomial order							
0	e_{avg}	201.73%	7.62%	0.48%	1.40%	0.48%	0.24%
	σ	1008.43%	7.48%	0.41%	0.92%	0.38%	0.20%
1	e_{avg}	39.35%	5.93%	0.44%	1.02%	0.46%	0.22%
	σ	58.93%	4.77%	0.33%	0.67%	0.34%	0.16%
2	e_{avg}	45.25%	4.18%	0.36%	0.76%	0.38%	0.19%
	σ	84.01%	3.58%	0.29%	0.69%	0.30%	0.14%
Samples: 400		$C_{n_{\beta}}$	$C_{n_{\delta_r}}$	LD	W_{wing}	MTOW	DOC
0	e_{avg}	35.39%	5.48%	0.46%	0.89%	0.47%	0.25%
	σ	43.97%	3.66%	0.29%	0.60%	0.29%	0.17%
1	e_{avg}	67.71%	6.02%	0.48%	0.95%	0.50%	0.27%
	σ	203.14%	5.13%	0.34%	0.91%	0.36%	0.19%
2	e_{avg}	55.80%	5.02%	0.39%	0.66%	0.41%	0.22%
	σ	214.38%	4.47%	0.26%	0.56%	0.27%	0.14%

The first thing to note when analysing the results is the large average error and even larger standard deviation of the $C_{n_{\beta}}$ and $C_{n_{\delta_r}}$ estimates. The results suggest the inability of the method to accurately predict these parameters. A more detailed analysis revealed that the large discrepancy can be explained by the size of the variable. Both $C_{n_{\beta}}$ and $C_{n_{\delta_r}}$ are small and as the parameters approach zero the relative error becomes more pronounced. This can be clearly seen when comparing the error for each of the 40 test configurations, tabulated in table 7.5. Normalization of these parameters yielded no increase in accuracy of the model.

Table 7.4: Accuracy of the cubic correlation model on the various parameters

Correlation model:	Cubic	Samples: 200						
Polynomial order			C_{n_β}	$C_{n_{\delta_r}}$	LD	W_{wing}	$MTOW$	DOC
0	e_{avg}	200	77.36%	13.37%	0.53%	1.99%	0.53%	0.22%
	σ		217.90%	19.34%	0.41%	1.76%	0.43%	0.18%
1	e_{avg}	400	40.23%	5.37%	0.45%	1.11%	0.46%	0.23%
	σ		66.77%	5.57%	0.31%	0.78%	0.33%	0.16%
2	e_{avg}	200	45.12%	4.31%	0.36%	0.75%	0.39%	0.18%
	σ		99.25%	3.34%	0.27%	0.70%	0.28%	0.14%
Samples: 400			C_{n_β}	$C_{n_{\delta_r}}$	LD	W_{wing}	$MTOW$	DOC
0	e_{avg}	400	116.01%	10.31%	0.56%	2.18%	0.50%	0.27%
	σ		420.60%	8.59%	0.38%	2.21%	0.40%	0.21%
1	e_{avg}	400	61.86%	6.65%	0.49%	0.99%	0.51%	0.27%
	σ		160.71%	6.99%	0.32%	0.94%	0.34%	0.18%
2	e_{avg}	400	35.15%	4.65%	0.41%	0.66%	0.42%	0.22%
	σ		85.97%	4.29%	0.27%	0.59%	0.29%	0.16%

An interesting observation is the limited influence of the regression and correlation models. Literature clearly demonstrates the importance of selecting an appropriate scheme to properly model the behaviour of a system, although the presented results shows otherwise [31]. The limited effect of the scheme could be attributed to the high density of sample points. By increasing the number of data entries, the dependency on estimation models is reduced as the effect of interpolation is minimized. Although the effect of the regression and correlation scheme is minimal, a selection was made based on the average error and standard deviation. The selected model encompasses a 2nd order polynomial in combination with a cubic correlation model.

When comparing the results of the model based on 200 samples to that consisting of 400 nodes it can be observed that the average error is similar. This similarity could also be explained by the high density of data points.

To conclude, the selected response surface strategy comprises of a 2nd order polynomial regression model connected to a cubic correlation scheme and is based on 400 sample points. The results presented in the next chapter are based on these settings.

Table 7.5: Established error, as computed using a 2nd order polynomial cubic scheme

Config	C_{n_β}			$C_{n_{\delta_r}}$		
	Analysis	Estimate	Error	Analysis	Estimate	Error
1	0.0138	0.0052	62.43%	-0.0153	-0.0157	2.45%
2	0.0255	0.0238	6.62%	-0.0254	-0.0254	0.15%
3	0.0030	0.0005	82.48%	-0.0060	-0.0058	4.26%
4	0.0417	0.0399	4.27%	-0.0219	-0.0234	6.57%
5	0.0444	0.0379	14.76%	-0.0229	-0.0239	4.44%
6	-0.0029	-0.0018	35.39%	-0.0065	-0.0070	6.75%
7	0.0026	0.0006	78.09%	-0.0062	-0.0050	19.17%
8	0.0237	0.0270	14.19%	-0.0184	-0.0181	1.86%
9	0.0249	0.0344	38.40%	-0.0182	-0.0171	5.98%
10	0.0066	0.0034	49.26%	-0.0069	-0.0077	11.67%
11	-0.0001	-0.0006	550.04%	-0.0105	-0.0104	1.21%
12	0.0278	0.0209	24.70%	-0.0172	-0.0163	5.09%
13	0.0252	0.0245	2.78%	-0.0245	-0.0245	0.02%
14	0.0052	0.0042	18.93%	-0.0073	-0.0069	5.36%
15	0.0195	0.0209	7.45%	-0.0134	-0.0139	4.12%
16	0.0123	0.0116	6.18%	-0.0101	-0.0107	6.03%
17	0.0056	0.0046	17.24%	-0.0090	-0.0093	3.41%
18	0.0551	0.0532	3.45%	-0.0247	-0.0275	10.99%
19	0.0285	0.0296	3.90%	-0.0228	-0.0217	4.73%
20	0.0054	0.0074	37.81%	-0.0149	-0.0135	9.27%
21	0.0232	0.0197	15.10%	-0.0189	-0.0184	2.73%
22	-0.0052	-0.0030	43.57%	-0.0116	-0.0097	15.89%
23	0.0068	0.0101	49.18%	-0.0069	-0.0061	11.62%
24	0.0181	0.0134	26.14%	-0.0156	-0.0158	1.15%
25	0.0192	0.0211	9.82%	-0.0116	-0.0121	4.68%
26	0.0091	0.0063	30.82%	-0.0104	-0.0106	1.73%
27	0.0399	0.0402	0.64%	-0.0257	-0.0266	3.62%
28	0.0064	0.0072	11.38%	-0.0130	-0.0130	0.45%
29	0.0161	0.0145	9.90%	-0.0132	-0.0138	4.10%
30	0.0231	0.0176	23.82%	-0.0146	-0.0145	0.28%
31	0.0049	0.0052	5.89%	-0.0098	-0.0097	1.01%
32	0.0194	0.0233	19.96%	-0.0190	-0.0178	6.36%
33	0.0185	0.0141	23.75%	-0.0155	-0.0157	1.07%
34	0.0665	0.0532	19.94%	-0.0409	-0.0398	2.86%
35	0.0346	0.0355	2.74%	-0.0267	-0.0260	2.62%
36	0.0372	0.0346	7.05%	-0.0216	-0.0229	5.59%
37	0.0287	0.0390	35.59%	-0.0230	-0.0229	0.51%
38	0.0388	0.0360	7.24%	-0.0213	-0.0217	1.66%
39	0.0300	0.0304	1.40%	-0.0146	-0.0148	1.21%
40	0.0340	0.0327	3.80%	-0.0184	-0.0190	3.52%

8

Results

The results in this chapter are based on the aerodynamic analysis and response surface calculations presented in the previous chapter. The constructed response surfaces enable the user to investigate the influence of the design variables on a number of key parameters, and ultimately optimize the configuration. The parameters that will be analysed in this chapter are C_{l_β} , C_{n_β} , $C_{n_{\delta_r}}$, the eigenvalues of the equations of motion, the lift over drag ratio, and the wing weight. The first part of this chapter will examine the behaviour of the listed parameters, while the second part will discuss the winglet optimization.

It is to be noted that the twist distribution is not included in the design process, hence the resultant spanload will not be optimized. This could lead to an unintended bias when comparing results, as one configuration might be closer to its optimum than another.

8.1. Parameter Analysis

This section on the behaviour of key parameters is decomposed into two stages. During the first stage the influence of the design variables on the aerodynamic performance and structural wing weight will be investigated, as a means to validate the constructed design process. Research into the implementation and optimization of conventional winglets identifies a clear relationship between the cant angle and the two performance parameters. Hence, the first stage is to verify whether these trends can also be observed in the presented winglet study. The second stage will discuss a variety of stability and control parameters. The aim is to identify and explain the behaviour of these parameters to provide a first step towards the generation of less computational intensive models.

8.1.1. Performance Parameters

While the investigation of the capabilities of VSAero in Chapter 6 validated the aerodynamic solver, the design program itself still needs to be authenticated. Comparison of the behaviour of the aerodynamic performance and structural wing weight to other winglet studies will be used as a verification of the system as a whole, before continuing to analyse the stability and control properties.

Lift over Drag ratio

Due to the selected aerodynamic method, both C_L and C_D will change when varying the geometry. This is in contrast to winglet studies that employ vortex lattice methods, which are able to predefine a specific lift coefficient. Therefore, the lift over drag ratio, LD, will be used to compare aerodynamic performance.

The complexity of the flow, as introduced in Chapter 4.2, requires a systematic approach to assess the influence of the individual design variables. The first variables to be analysed are the cant angle and aspect ratio. The resulting carpet plots are depicted in figure 8.1. During the analysis the taper ratio was set to 0.41 and Λ_w was fixed at 40.0 degrees. It was found that the winglet taper ratio had limited influence on the performance and demonstrated similar behaviour as the root chord ratio.

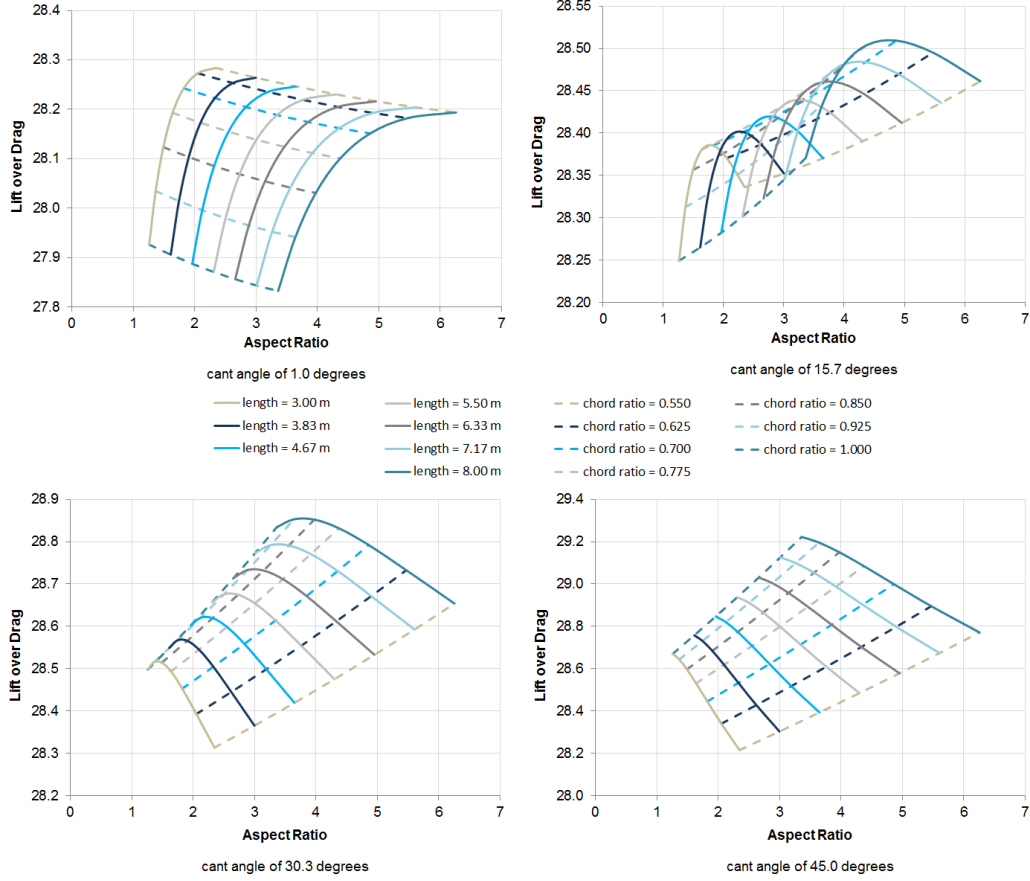


Figure 8.1: The variation in lift over drag as a function of the aspect ratio and cant angle

A number of interesting observations can be made from the resulting plots. One thing to notice is the parabolic behaviour of the l_w -curves, which appears to be more pronounced for shorter winglets. In order to explain this behaviour, a more detailed analysis of C_L and C_D is needed. Investigation into these aerodynamic coefficients indicates that the shape of the parabolic progression of C_L is nearly independent of the cant angle, figure 8.2. Therefore, it was opted to generate a number of VSAero configurations, corresponding to a single cant angle, to compare the behaviour found by the aerodynamic solver to the constructed response surface. The VSAero predictions lead to a scattering of points, as depicted in figure 8.3. The response surface, unable to capture this erratic behaviour, establishes a curvature that minimizes the average error. For the performed analysis the average error was found to be 0.97%, with a maximum of 1.29%. However, to fully understand the irregularities of the computed lift coefficient, one has to redirect its scope away from the winglet. Analysis of the spanwise lift distribution illustrates the sensitivity of the aerodynamic computations over centre body. Due to the high levels of sweep, the mesh becomes significantly skewed. As a result, the skewed cells appear to be more sensitive to pressure variations. Therefore, VSAero advises to use grids with sweep angles smaller than 60.0 degrees [30]. However, the shape of the baseline multi-fuel hybrid body makes it impossible to honour this criterion.

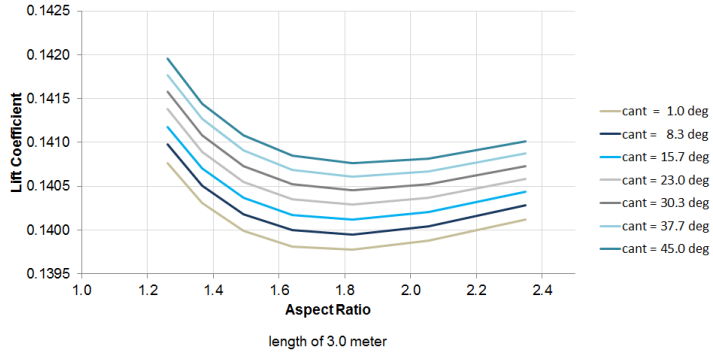


Figure 8.2: An isolated overview of the effect of the cant angle on the lift coefficient

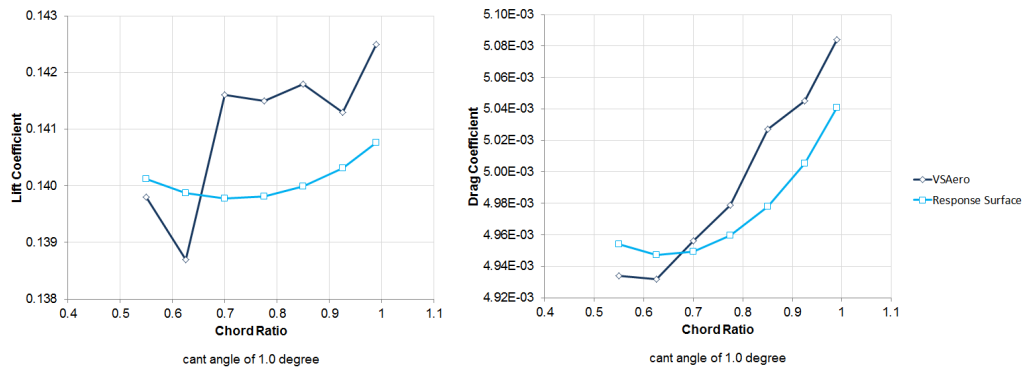


Figure 8.3: Comparison between the lift and drag coefficient of a 3.0 m winglet

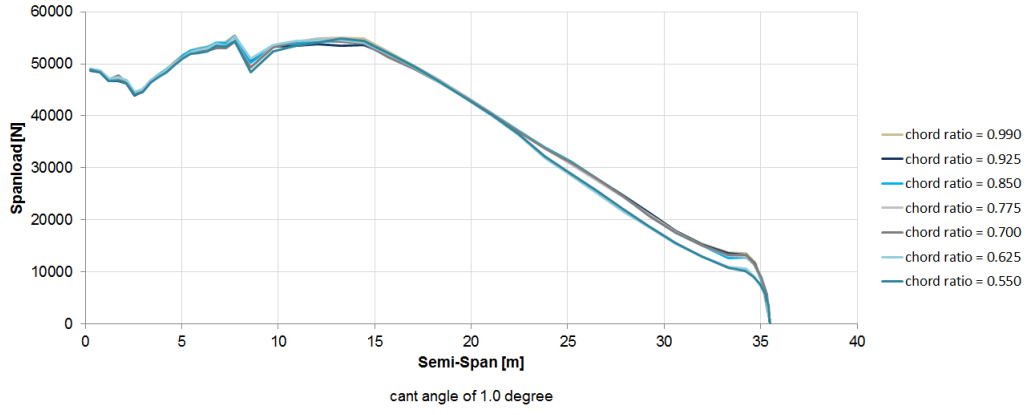


Figure 8.4: The variation in spanload of a 3.0 m winglet as a function of the root chord ratio

Returning to the carpet plots presented in figure 8.1 and focussing on the nearly vertical winglet, it can be seen that increasing l_w has a negative effect on LD, despite the increase in aspect ratio. This can be explained by the quadratic relation between the lift coefficient and the induced drag. The presence of the winglet obstructs the formation of trailing vortices at the wingtip, allowing for a higher tiploading. This increase in lift can be further amplified by elongating the non-planar surface, which diverts the trailing vortices away from the wing. The resultant forces generated by the surface will also contribute to C_L , albeit being marginal due to its orientation. The indicated rise in C_L , in combination

with the increase in surface drag and the limited influence of the nearly vertical surface on the effective span, yields a significant increase in drag. This is in accordance with Munk's theorem for minimized induced drag [23]. The theorem states that the normal-wash, corresponding to a minimum induced drag, can be described as a function of the cosine of the dihedral. Hence, theory indicates that the normal-wash generated by a nearly vertical winglets ought to be limited.

When the cant angle is increased, the force generated by the winglet is angled to have a stronger component in z-direction, adding to the total lift. Apart from its influence on C_L , the canted surface will have a more pronounced effect on the aspect ratio of the system as a whole. As a direct result of the change in effective span and corresponding aspect ratio, the induced drag of the system can be reduced by elongating the non-planar component. Similar to the previously discussed configuration, a balance needs to be found between the generated forces and the cant angle, as is evident from figure 8.1. From these carpet plots it can be seen that larger values for the lift over drag can be achieved by increasing the cant angle. This observation is substantiated by other research on the effect of winglets [19, 21].

Analysis of the effect of sweep reveals a similar need for balance between the cant angle and the forces produced by the winglet. This behaviour can be explained by connecting sweep theory to Munk's theorem. Sweep theory indicates that the velocity as experienced by the surface is dependent on the relative angle to the flow. By increasing this angle the forces generated by the surface will be lowered. For near vertical configurations the optimum sweep angle is at approximately 55.0 degrees. This relative large Λ_w limits the production of the normal-wash. However, as the cant angle increases the parabolic curves in figure 8.5 translate towards higher LD and lower Λ_w . This is in agreement with Munk's theorem.

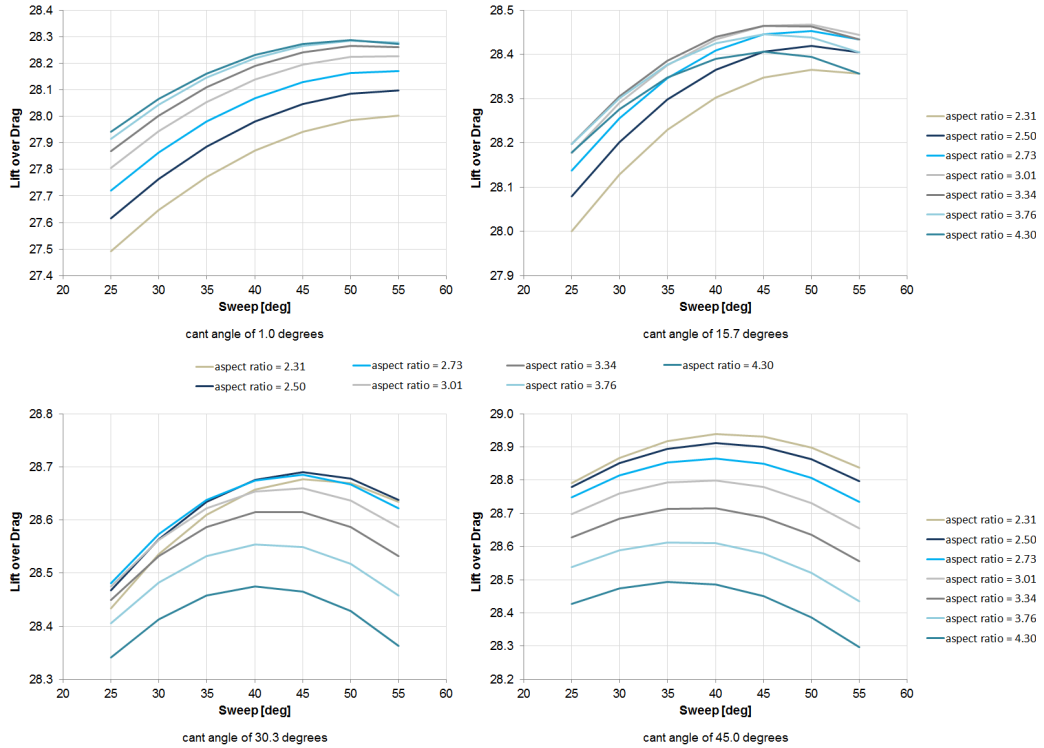


Figure 8.5: The variation in lift over drag as a function of the aspect ratio and sweep angle

Structural Wing Weight

Each of the design variables will have an impact on the structural continuity of both the front and aft spar, as well as on the torsion and bending moment. Throughout the analysis the change in wing weight will be explained by determining the influence of the design variables with respect to these aspects.

Before discussing the effect of the individual parameters, it is to be noted that the implementation of a winglet redistributes the aerodynamic forces near the wingtip. Due to the added surface the lift distribution near the wingtip will be higher, as it is no longer required to return to zero. The corresponding increase in bending moment, in combination with the added weight of the structural component, will have a negative effect on the wing weight. However, the shape and size of the configuration will have a strong influence on the aerodynamic and structural loading.

The effect of the cant angle as a function of the aspect ratio is monitored first. The results, depicted in figure 8.6, are based on a fixed taper ratio of 0.41 and a Λ_w of 40.0 degrees. The figure illustrates a significant increase in structural weight for increasing φ . Changes to the cant angle alter the orientation of the resultant force generated by the winglet. When φ increases, the new orientation has a negative impact on the wing weight, as it significantly contributes to the bending moment due to its large moment arm. The presented relationship between the cant angle and wing weight has also been identified in other winglet studies [19, 21, 26].

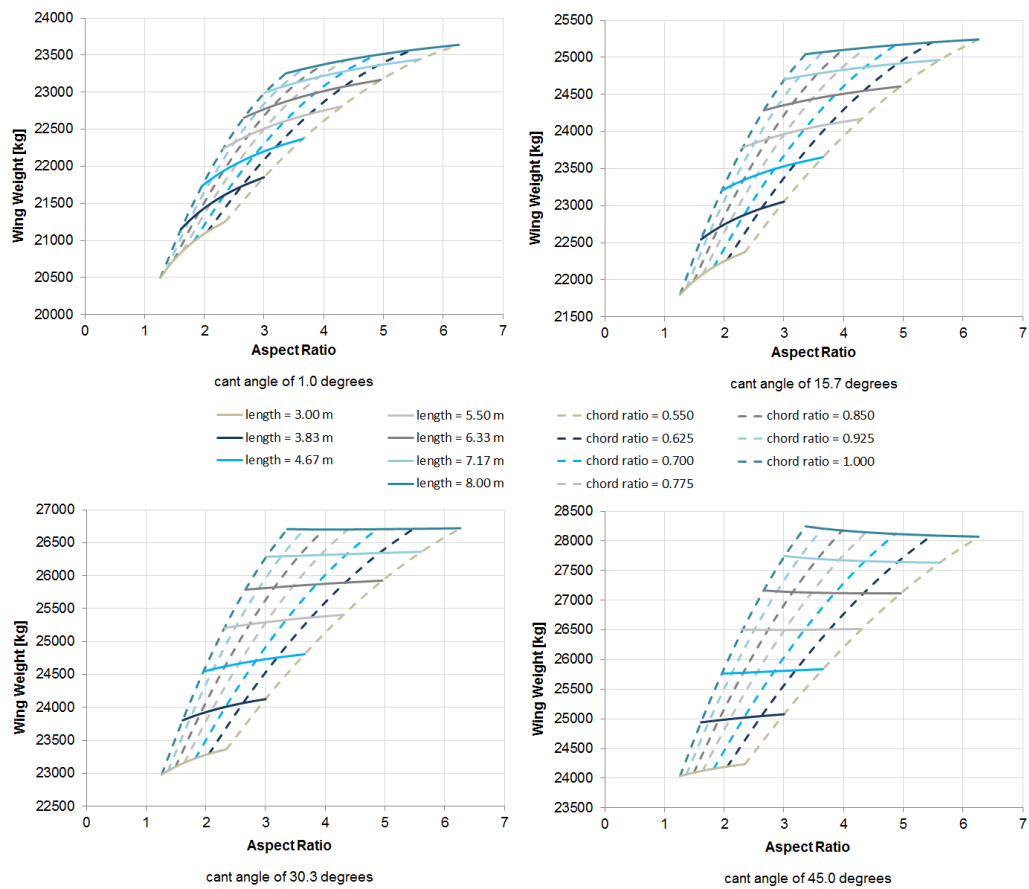


Figure 8.6: An isolated overview of the effect of the cant angle on the structural wing weight

Figure 8.6 also reveals the influence of the root chord ratio. When the root chord ratio is reduced, the front spar will encounter a discontinuity due to the constant chordwise position of the spar. To cope with the resulting stress concentrations, the member is reinforced by increasing its size. A similar situation is created when tapering the non-planar surface, albeit the effect is less pronounced. The structural discontinuity causes the wing weight to increase, despite the minor reduction in aerodynamic loading associated with a reduction in c_{r_w} and λ_w . As φ increases, the kink in the structural member becomes less pronounced and the aerodynamic loading will occupy a more prominent role. This effect is clearly visible in the carpet plots as the change in gradient of the constant l_w -curves.

To explain the influence of sweep, depicted in figure 8.7, one has to account for both structural and aerodynamic effects. When the surface is swept, the local centre of pressure is translated aft. However, as the longitudinal distance to the centre of gravity is expanded, the forces generated by the swept surface decrease. Apart from altering the torsion and bending moment, sweep also yields a discontinuity of the load paths. Similar to the effect of the root chord ratio, this discontinuity creates stress concentrations that need to be compensated for by increasing the mass of the spars.

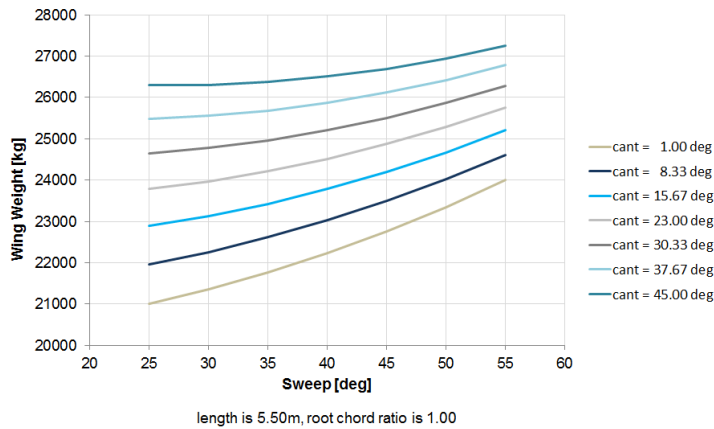


Figure 8.7: The variation in structural wing weight as a function of the cant and sweep angle

To conclude, the performance parameters show similar trends as identified by other winglet studies. Hence, further investigation of the stability and control characteristics is warranted.

8.1.2. Stability and Control Parameters

This section investigates the behaviour of key stability and control parameters. The aim is to provide insight into the influence of the design variables, which is needed to construct less computational intensive models. The stability and control parameters that are investigated are C_{l_β} , C_{n_β} and C_{δ_r} .

It is to be noted that, although the canted surface will have a contribution to both the rolling and yawing moment, the effective dihedral and weathercock stability will be discussed separately. The reason for this is the relative large error in the response surface with respect to the decomposed forces induced by the sideslipping motion. The deviation between these estimates would make the analysis of the behaviour and orientation of the resultant force unreliable. An overview of the error of the various response surfaces can be found in Appendix C.2.

Effective Dihedral

The effective dihedral can be described as a moment response to a sideslipping motion. The behaviour of this parameter is rather complex and largely depends on the characteristics of the wing. The current research will identify the variation of $C_{l\beta}$ for varying winglet configurations. It will do so by relating the change in configuration to the corresponding change in moment arm or generated forces. Similar to the analysis of the performance parameters, the investigation of $C_{l\beta}$ starts with the generation of a number of carpet plots. These plots have been constructed using a constant taper ratio of 0.41 and a sweep angle of 40.0 degrees.

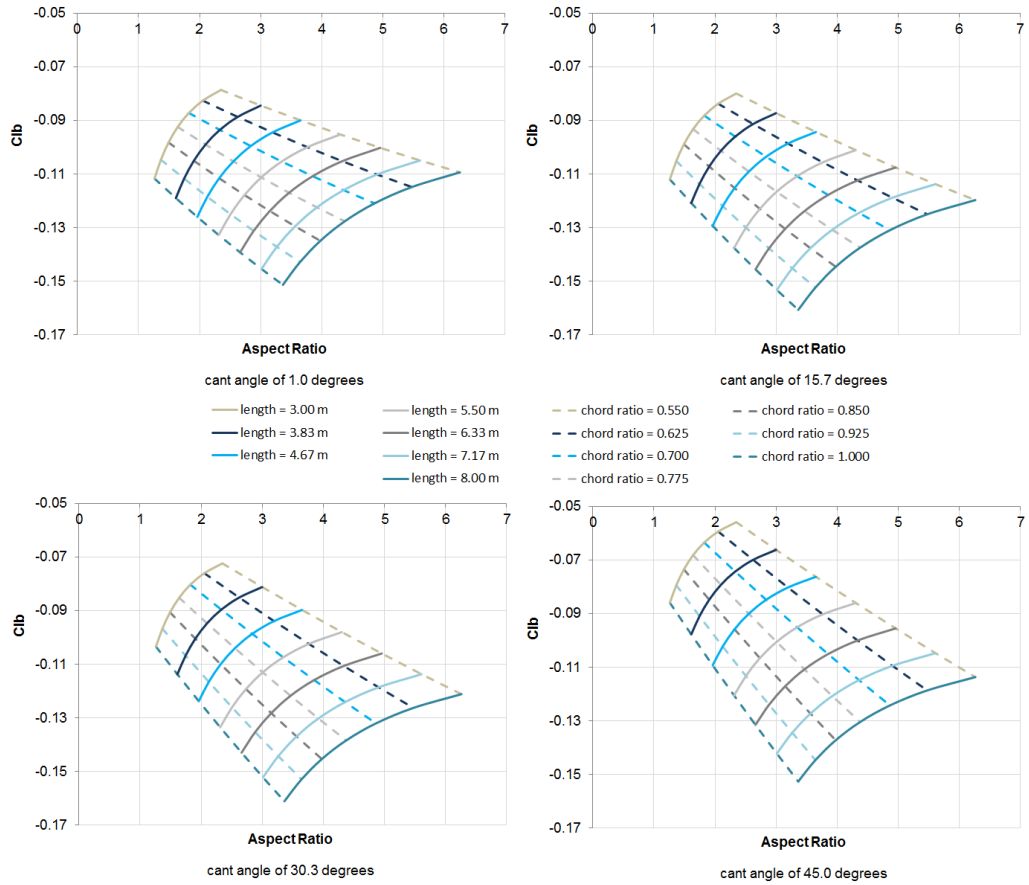


Figure 8.8: The variation in effective dihedral as a function of the cant angle and aspect ratio

The results, visualized in figure 8.8, show a clear repetitive pattern that demonstrates only minor variations for changing cant angle. From the figure it can be seen that the effective dihedral is reduced when smaller root chord ratios are applied. To explain this behaviour, it is important to emphasize that $C_{l\beta}$ describes the rolling motion due to sideslip. In a sideslipping motion the winglet on the leading wing will partly obstruct the flow near the wingtip. On the trailing wing the canted surface will act as an endplate, creating a slightly higher wingloading. However, due to the motion there will also be a discrepancy in the sweep angle as experienced by the two wings, figure 8.9. This would lead to an asymmetric spanload that generates a restoring rolling moment. The previously mentioned blocking effect of the winglet will slightly reduce this asymmetric lift distribution and shorten its moment arm, albeit this effect is limited. The sideslip also causes a force differential between the two winglets, as a result of the variation in effective angle of attack. Due to the lateral velocity component, the leading winglet will experience an increase in α , while the angle of attack on the trailing tip device is reduced. This effect is most pronounced for nearly vertical winglets. Decomposition of this resultant force will have a lift generating

component that contributes to the restoring moment. Hence, as the root chord ratio is reduced, the force differential deteriorates and the stabilizing moment becomes smaller.

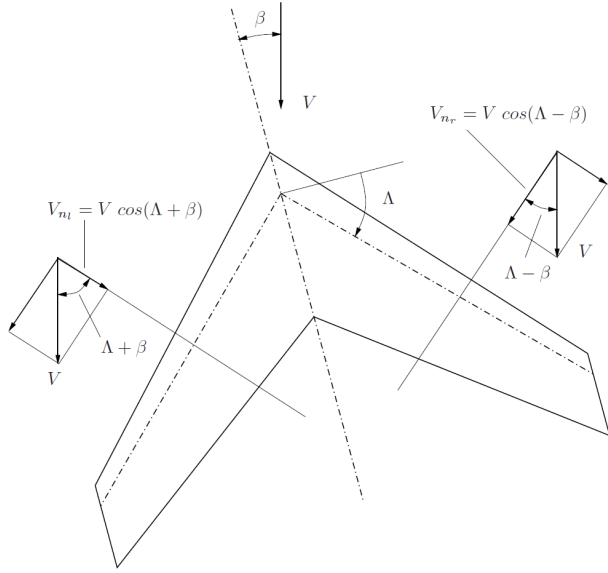


Figure 8.9: The effect of sideslip on the perceived sweep angle - source: J.A. Mulder et al, "Flight Dynamics" [14]

Similar to the root chord ratio, the length of the winglet will influence the generated forces. However, l_w will also have a more pronounced impact on the moment arm. When the winglet is canted, the orientation, size and position of the resultant force is altered. Hence, the contribution of the winglet to $C_{l\beta}$ is a balance between the force differential, the change in moment arm, and the variation of the perceived sweep angle. The resulting relation for the cant angle, as found by the response surface, is depicted in figure 8.10.

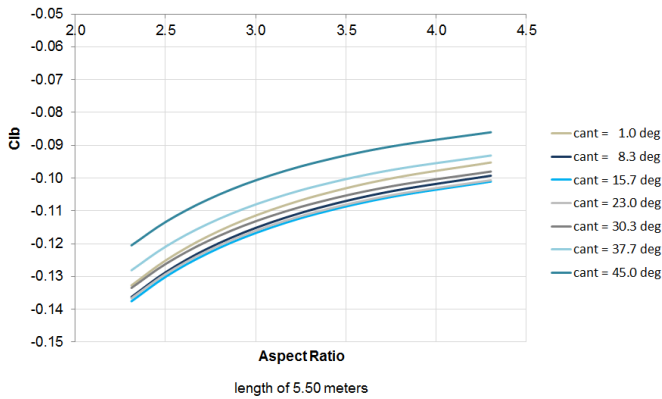


Figure 8.10: An isolated overview of the effect of the cant angle on the effective dihedral

It had been illustrated that the contribution of the winglet to $C_{l\beta}$ is dependent on a number of aspects. As a result the influence of the sweep angle will also vary. Figure 8.11 visualizes the effect of Λ_w for a winglet corresponding to a length of 5.5 m, a taper ratio of 0.41, and a root chord ratio of 1.0. The plot shows a vertical translation that is in accordance with the previously demonstrated cant angle behaviour. It also shows that the influence of sweep is more pronounced for small values of φ . This further illustrates the previously introduced theorem.

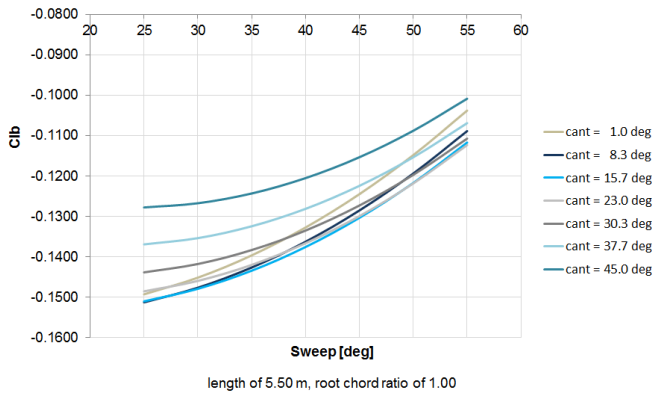


Figure 8.11: The variation in effective dihedral as a function of the cant and sweep angle

Weathercock Stability

In contrast to C_{l_β} , the weathercock stability can be more easily explained. However, rather than monitoring C_{n_β} directly, it was opted to use the side-force coefficient due to sideslip, C_{Y_β} . The choice was motivated by the apparent difficulties of the response surface to accurately map the behaviour of C_{n_β} . Further investigation into the accuracy of the different surfaces showed a significantly lower average error and standard deviation for C_{Y_β} , Appendix C.2. By analysing this parameter, the behaviour of the weathercock stability can be described in more detail. The only component that will not be monitored, but theorized, will be the influence of the design variables on the longitudinal distance between the centre of gravity and the location of the resultant force.

To generate a yawing moment there ought to be a resultant side-force that is not aligned with the centre of gravity. In the previous analysis it had been noted that the sideslipping motion creates a difference between the perceived angles of attack of the leading and trailing winglets. This imbalance in α_{eff} is largely responsible for the aforementioned side-force due to sideslip. Monitoring the behaviour of C_{Y_β} for a range of l_w and root chord ratios clearly demonstrates that a larger surface corresponds to a stronger lateral force, figure 8.12.

By selecting an appropriate combination combination of λ_w , l_w , and cr_w , one can obtain a specified C_{Y_β} . However, each of these parameters will also have an influence on the moment arm and, therefore, on C_{n_β} . Decreasing the taper ratio will result in a higher aspect ratio, and corresponds to an aft translation of the local centre of pressure. The taper ratio also modifies the shape of the non-planar component. Smaller values for λ_w will yield a downward shift of the c.p. In combination with sweep, this downward shift will result in a shorter moment arm. Sweep also translates the c.p. aft when the winglet is elongated. The final option to alter the surface area is by changing the root chord ratio. Due to its definition and alignment, a reduction in cr_w would also yield a longer moment arm.

Another observation that can be made from figure 8.12, is the change in C_{Y_β} with varying cant angle. As the cant angle is increased, the orientation of the resultant force reduces the component in lateral-direction. It is to be noted that φ only alters the side-force and not the moment arm.

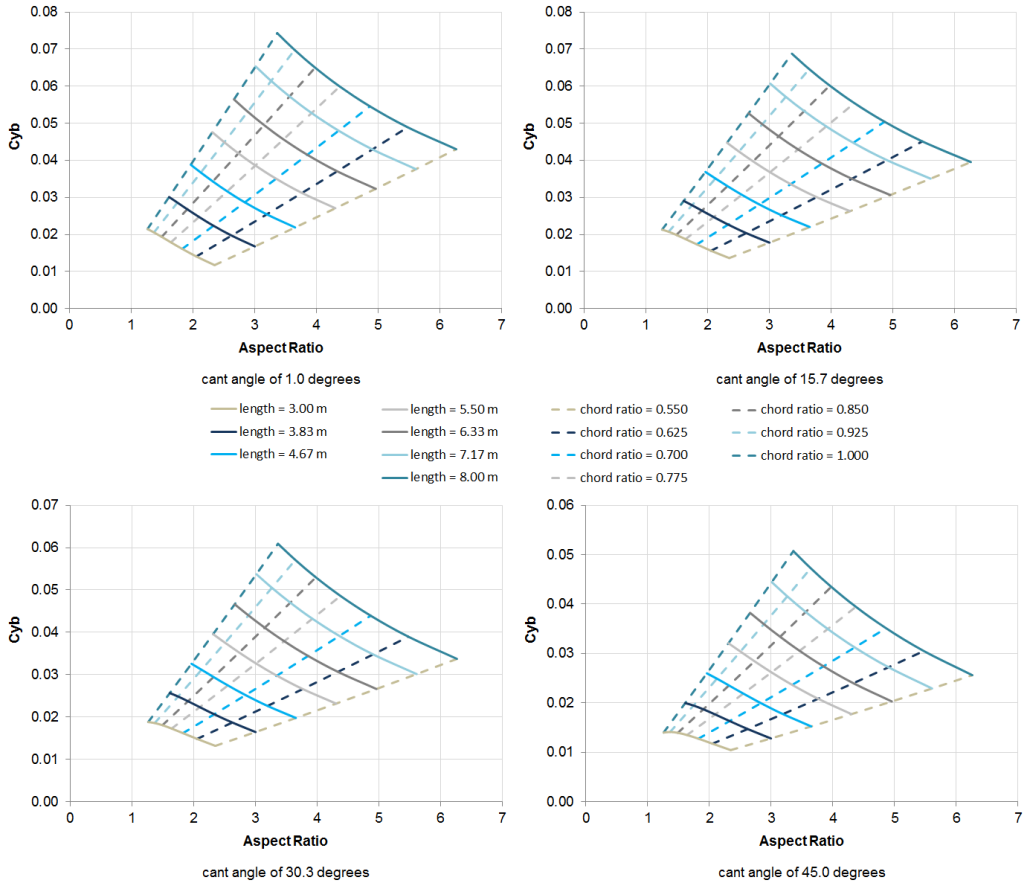


Figure 8.12: The variation in side-force coefficient due to sideslip as a function of the cant angle and aspect ratio

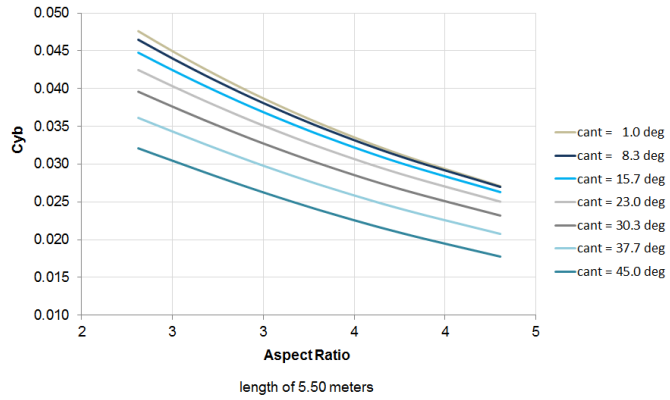


Figure 8.13: An isolated overview of the effect of the cant angle on the side-force coefficient due to sideslip

The final design variable that is to be analysed is the sweep angle. The impact of this variable on the moment arm has already been discussed. However, figure 8.14 also demonstrates its influence on the side-force due to sideslip. Increasing the sweep angle would reduce the forces generated by the winglet. The effect of sweep on the weathercock stability is dependent on whether the change in moment arm is stronger than the change in side-force, which depends on the characteristics of the winglet.

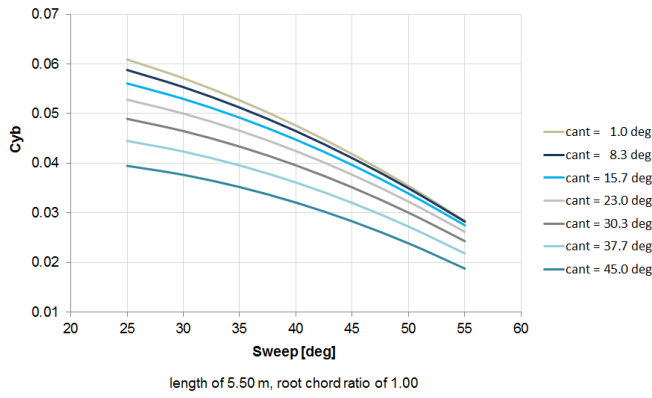


Figure 8.14: The variation in side-force coefficient due to sideslip as a function of the cant and sweep angle

Rudder Control Power

The control surfaces embedded in the winglets are the pilot's primary controls to adjust the heading. Therefore, it is imperative that these moveables are able to initiate an adequate yawing moment. In addition to the winglet design variables, an extra parameter had to be included to account for the control surface. For this purpose the hinge position was defined, which represents the chordwise location of the hingeline with respect to the trailing edge. It is recognized that the controls incorporated in the canted surface will also have a contribution to the rolling moment. However, as a proper control allocation of both aileron and elevator is yet to be performed, the focus will solely be on the moment about the z-axis.

The rudder deflection is mathematically modelled as the local rotation of the normal-component in the flow-tangency condition, effectively simulating the control surface as a non-slotted flap. According to plain flap aerodynamics, a secondary pressure peak will form in response to the sudden change in geometry. During the analysis of the control power a limited deflection of 5.0 degrees was used, resulting in only a minor secondary peak. Hence, once a winglet configuration has been selected, it is to be investigated whether the boundary layer is able to cope with the flow characteristics for a wide range of deflection angles.

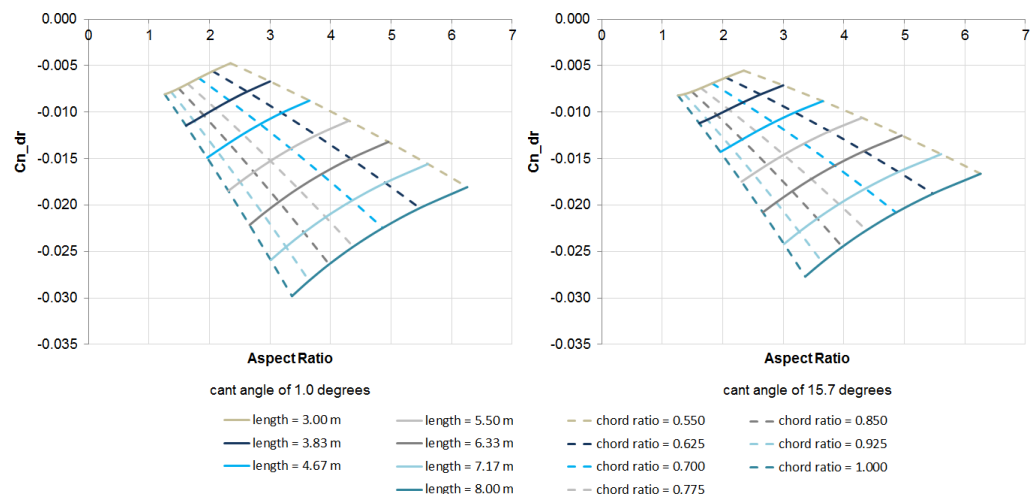


Figure 8.15: The variation in control power as a function of the cant angle and aspect ratio

Analysis of the behaviour of the control power demonstrates a clear dependency on the size of the canted surface, figure 8.15. The carpet plots for only 2 cant angles have been included, as the plots reveal similar behaviour to C_{Y_β} . The images correspond to a winglet with a taper ratio of 0.41, a sweep angle of 40.0 degrees, and H_w of 0.30. Since the hinge position is defined as a percentage of the chord, enlarging the surface area will also result in an increase of the control surface. The control power is not only dictated by the forces generated by the moveable, it also depends on its distance to the centre of gravity. However, the discussion on the influence of the geometric variables on the moment arm has already been presented during the analysis of C_{n_β} , and will not be repeated here.

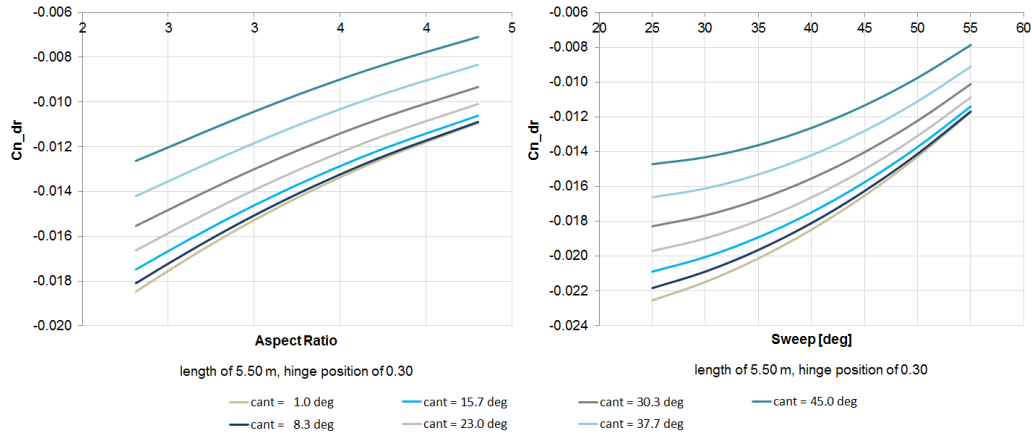


Figure 8.16: An isolated overview of the effect of the cant angle and sweep on the control power

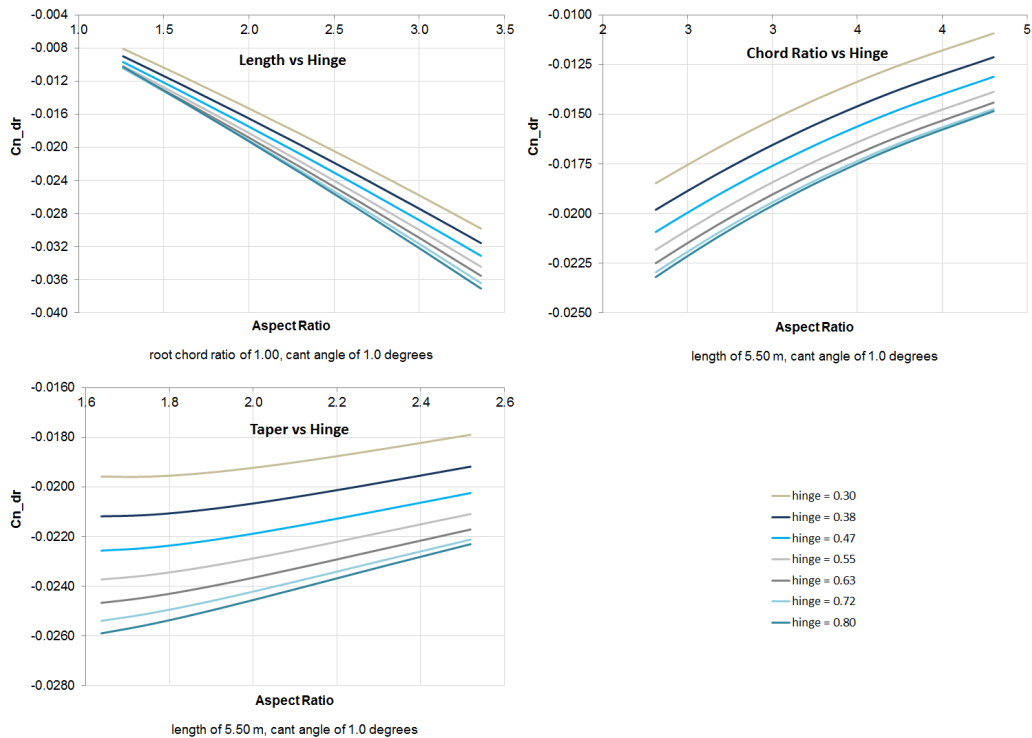


Figure 8.17: An isolated overview of the effect of the hinge position and various geometric parameters on the control power

A more detailed description of the cant angle and sweep is visualized in figure 8.16. The image clearly shows the change in orientation of the generated forces for varying φ and its influence on the control power. The plot on the right-hand side demonstrates the impact of sweep theory. The influence of Λ_w on $C_{n\delta_r}$ is equal to the relationship found between sweep and previously discussed stability parameters.

The final stage of the analysis investigates the influence of the hinge position itself. As was to be expected, the results show that increasing H_w corresponds to an increase in control power. It is to be noted that the presented research allows for a wide range of H_w . Large values for the hinge position could compromise the structural integrity of the design. It could also cause the leading edge suction peak to interact with the secondary pressure jump. Therefore, more detailed research is advised when considering such a configuration.

8.1.3. Eigenmode Analysis

The solution to the eigenvalue problem of the equations of motion provides insight into the dynamic stability of the aircraft. In Chapter 3.1.2 it had been indicated that the lateral-directional equations produce 2 aperiodic, and 1 oscillatory mode. The analysis of the individual modes is based on the constructed response surfaces. At the beginning of each subsection the level of accuracy of each of these models will be presented. As the correlation between the various stability derivatives is rather complex, a simplified system will be used to guide the discussion on the influence of the geometric design variables on the different eigenmodes.

Roll Mode

The aperiodic roll subsidence mode is a heavily damped motion and can often be significantly decoupled from the other eigenmodes. The winglet design program utilizes the eigenvalue to construct the response surface. It was found that the average error was approximately 10.0%, with a standard deviation of 7.3%.

Since the non-oscillatory roll is heavily damped, the other motions will have little time to impact this eigenmotion. Therefore, the equations of motion can be simplified by assuming that the aircraft is only able to roll, equation 8.1. This would lead to the following expression for the eigenvalue of the roll mode: [14]

$$\left(C_{l_p} - 4\mu_b K_X^2 D_b \right) \frac{pb}{2V} = 0 \quad (8.1)$$

$$\lambda_{rm} = \frac{C_{l_p}}{4\mu_b K_X^2} \quad (8.2)$$

$$T_{rm} = \frac{-1}{\lambda} \quad (8.3)$$

According to the simplified equation, the eigenmode depends on the rolling moment coefficient due to an initialized roll-rate and on the general characteristics of the aircraft. Hence the impact of the winglet design variables ought to be limited. The carpet plots depicted in figure 8.18 illustrate that for nearly vertical winglets the time constant is hardly influenced by the geometry. When the cant angle is increased, the significance of the non-planar component becomes more visible. This can be explained by the change in orientation of the resultant force and its contribution to the rolling moment.

A closer investigation into the influence of the various parameters reveals that the root chord ratio has the most pronounced effect, figure 8.19. As the root chord ratio is reduced T_{rm} converges on a single value, regardless of the cant angle. This suggests that the contribution to the rolling moment due to roll-rate is largely generated by the inboard section, despite the relative shorter moment arm. Further investigation also shows the marginal effect of the taper ratio and sweep angle. This also suggests that the contribution of the winglet to T_{rm} is dominated by the transition from wing to winglet, rather than by the forces generated by the canted surface.

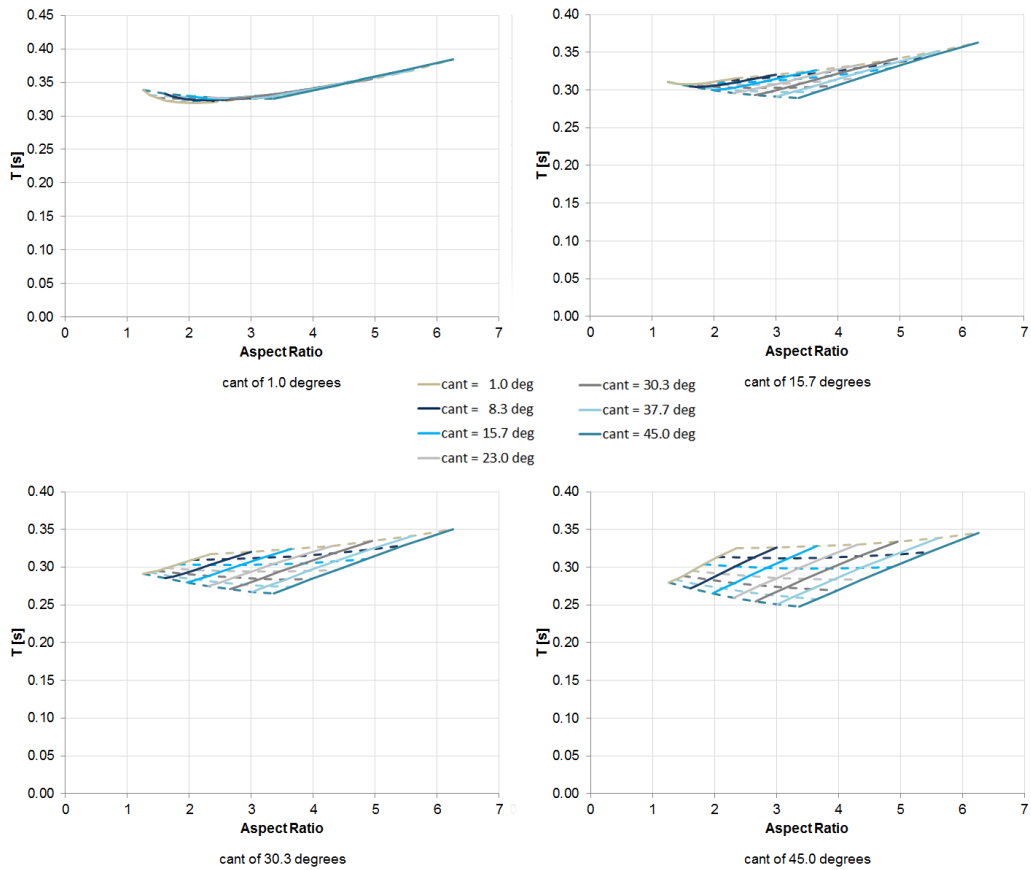


Figure 8.18: The variation in roll damping as a function of the cant angle and aspect ratio

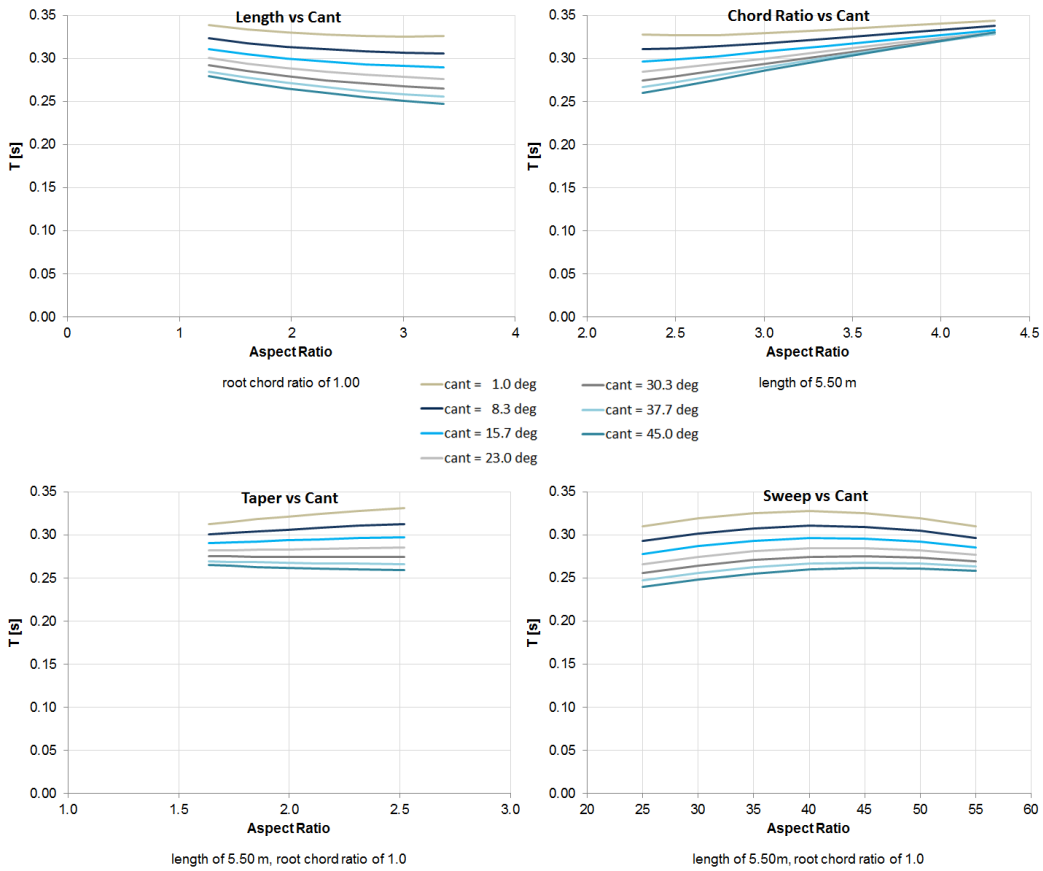


Figure 8.19: An isolated overview of the effect of the various geometric parameters on the roll mode

Spiral Mode

The spiral is a complex eigenmode that couples roll, yaw, and sideslip [13]. The weakly damped motion is often close to neutral stability. These small values for λ_{sp} and the presence of both stable and unstable configurations result in an extremely large error and standard deviation. As the average error is defined as the deviation of the estimate with respect to the aerodynamically computed value, sign changes and values approaching zero will cause a relative large error. Analysis of the accuracy of the eigenvalue indicates the average error to equal 58.0%, with a standard deviation of 114.8%. It is recognized that the response surface data is not reliable and further investigation is needed to generate more accurate models. Therefore, it is opted to omit the analysis of the aperiodic spiral mode from this report.

Dutch Roll

The last asymmetric eigenmotion is the harmonic dutch roll. The complex conjugates that result from the characteristic equation provide the damping and frequency of this swaying motion. For a complete analysis the behaviour of both ζ_{dr} and ω_{dr} will be mapped. The average error for the damping was found to be 15.3% with a standard deviation of 13.2%, while the frequency corresponds to a e_{avg} of 12.6% and a σ of 8.6%.

The dutch roll can be described as a motion in yaw, roll, and sideslip. However, the periodic motion can be approximated by omitting roll from the equation. The resulting system, equation 8.3, produces a quadratic equation that yields the following expression for the damping and frequency:

$$\begin{bmatrix} C_{Y\beta} - 2\mu_b D_b & -4\mu_b \\ C_{n\beta} & C_{n_r} - 4\mu_b K_Z^2 D_b \end{bmatrix} \begin{bmatrix} \beta \\ \frac{rb}{2V} \end{bmatrix} = 0 \quad (8.4)$$

$$\lambda_{dr} = \xi \pm \eta i \quad (8.5)$$

$$\xi = \frac{C_{n_r} + 2K_Z^2 C_{Y\beta}}{8\mu_b K_Z^2} \quad (8.6)$$

$$\eta = \frac{\pm \sqrt{(-2\mu_b (C_{n_r} + 2K_Z^2 C_{Y\beta}))^2 - (24\mu_b^2 K_Z^2)(4\mu_b C_{n\beta} + C_{Y\beta} C_{n_r})}}{16\mu_b^2 K_Z^2} \quad (8.7)$$

$$\zeta_{dr} = \frac{-\xi}{\sqrt{\xi^2 + \eta^2}} \quad (8.8)$$

$$\omega_{dr} = \sqrt{\xi^2 + \eta^2} \frac{V}{b} \quad (8.9)$$

The expressions indicate that the stability of the oscillatory motion is strongly influenced by the design of the non-planar component. Investigation into the impact of the geometric design variables on ζ_{dr} substantiate this claim.

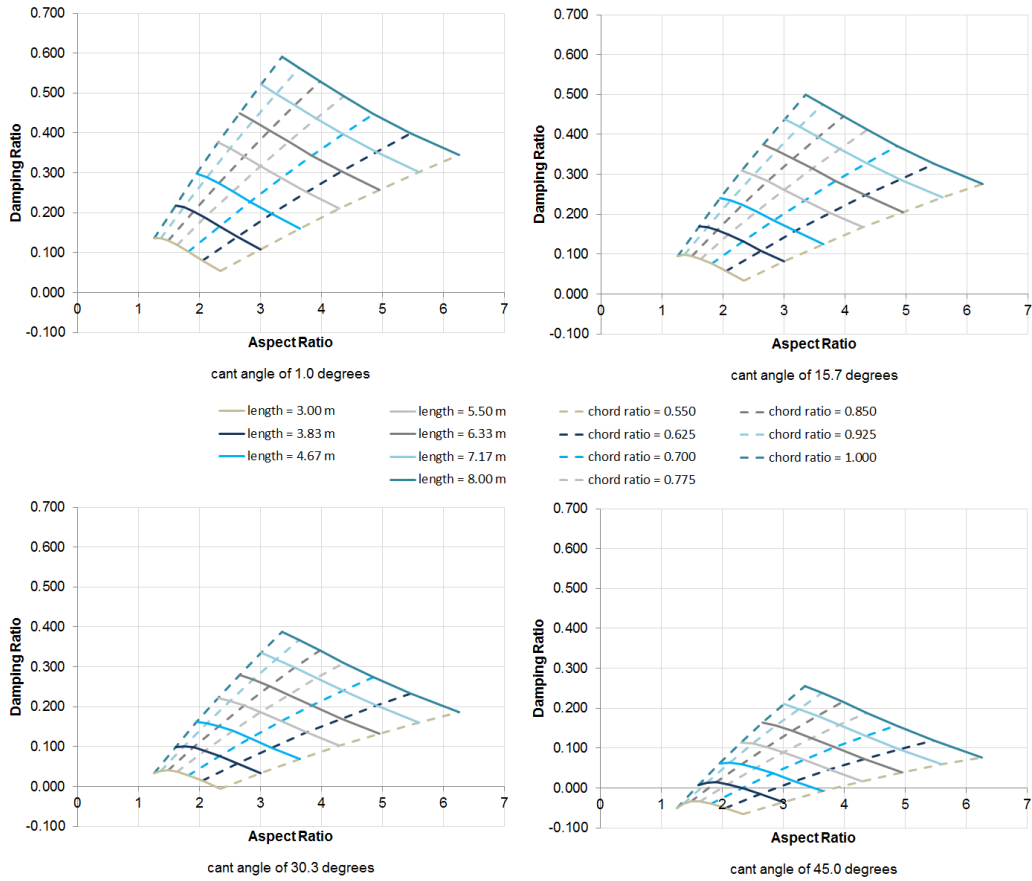


Figure 8.20: The variation in dutch roll damping as a function of the cant angle and aspect ratio

The vertical shift and compression of the carpet plots with increasing cant angle is clearly visible in figure 8.20. As the cant angle becomes larger, the lateral forces generated by the canted surface deteriorate. Reduction of the surface area of the winglet has a similar effect. Further investigation into the influence of the individual design parameters on a 5.50 m winglet confirms this relation, figure 8.21. The impact of the root chord ratio and length is most noticeable, as they have the strongest influence on the size of the tip device. When the cant angle is increased the effect of all geometric variables, including sweep, becomes weaker. This is most likely a direct result of the change in orientation of the normal force and its contribution to the yawing moment.

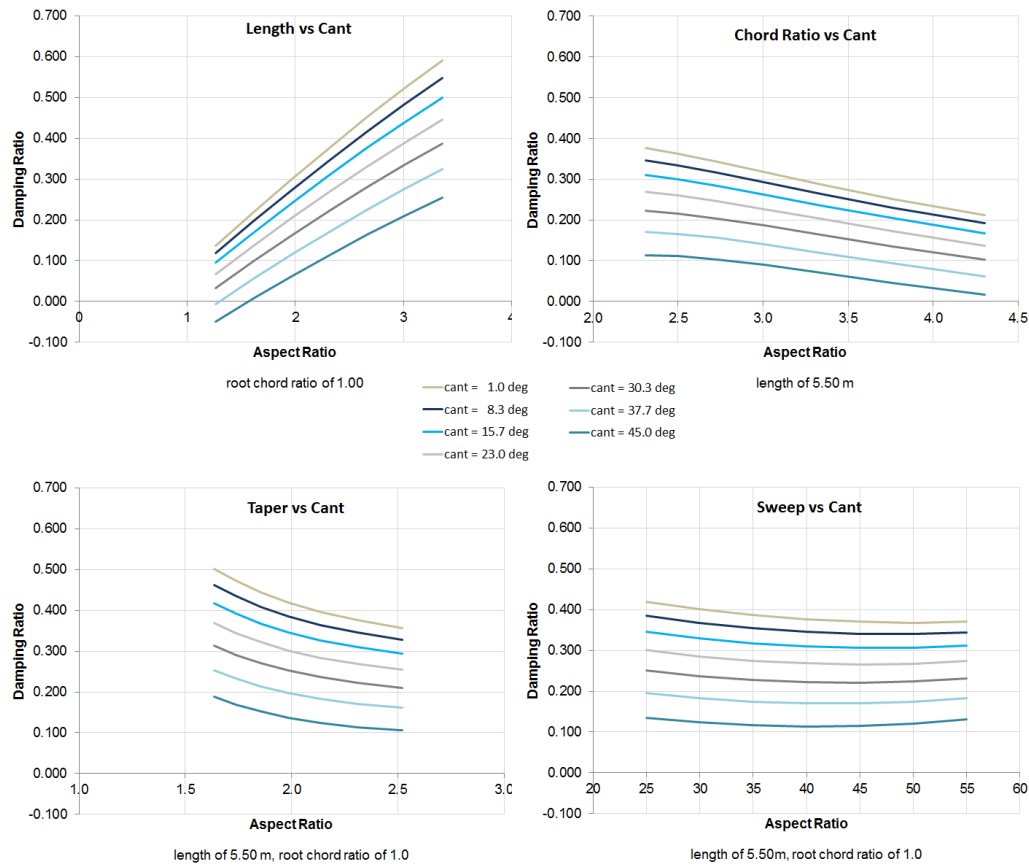


Figure 8.21: An isolated overview of the effect of the various geometric parameters on the dutch roll damping

The simplified equation for the frequency, equation 8.9, indicates that the parameter is dependent on a large number of factors. Most of these parameters are related to either the characteristics of the vertical component or the general properties of the aircraft. However, the carpet plots, represented in figure 8.22, illustrate the limited influence of the winglet configuration on ω_{dr} . The influence is even further reduced when the cant angle is increased. A more detailed investigation was performed on a 5.50 m winglet to identify the correlation between the variables and the frequency, figure 8.23. Similar to ζ_{dr} , it appears that the frequency is dependent on the production of lateral forces. Hence, a large surface area and small values for φ correspond to an increase in frequency. This corroborates the dependency on the vertical component, as indicated by equation 8.9. It is to be noted that all investigated configurations lead to a dutch roll frequency that is below the threshold for satisfactory flight characteristics, as indicated by the handling quality levels, table 3.2. Since a wide spectrum of winglet configurations has been analysed, which appears to have little influence on ω_{dr} , the baseline aircraft is to be modified to meet the HQL requirements.

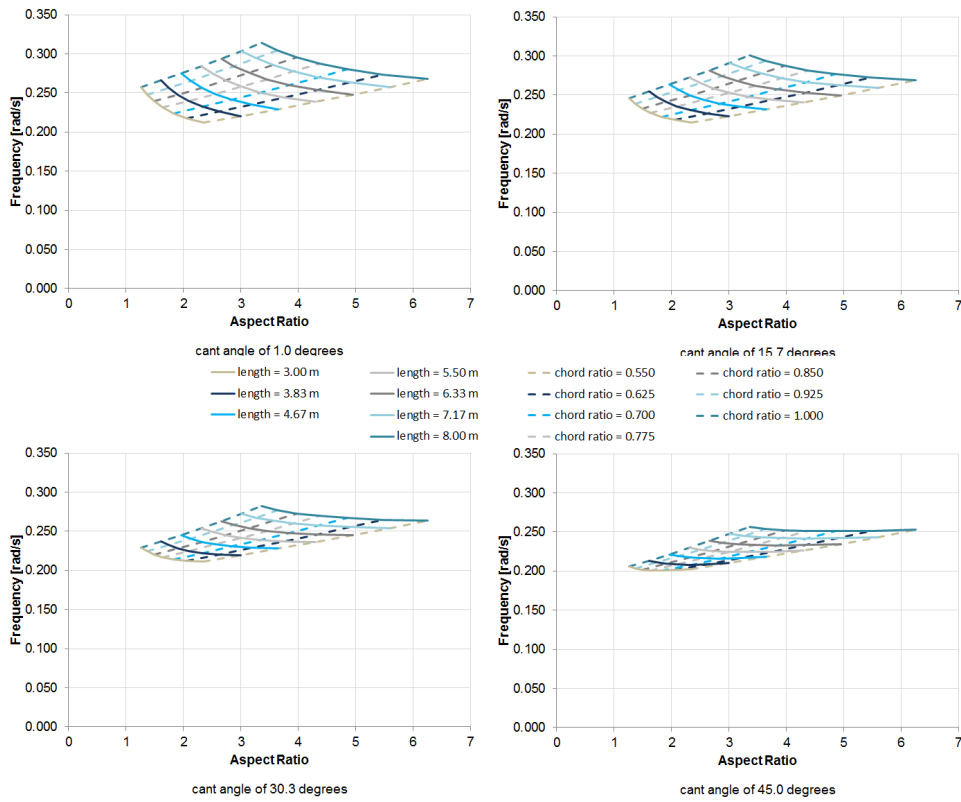


Figure 8.22: The variation in dutch roll frequency as a function of the cant angle and aspect ratio

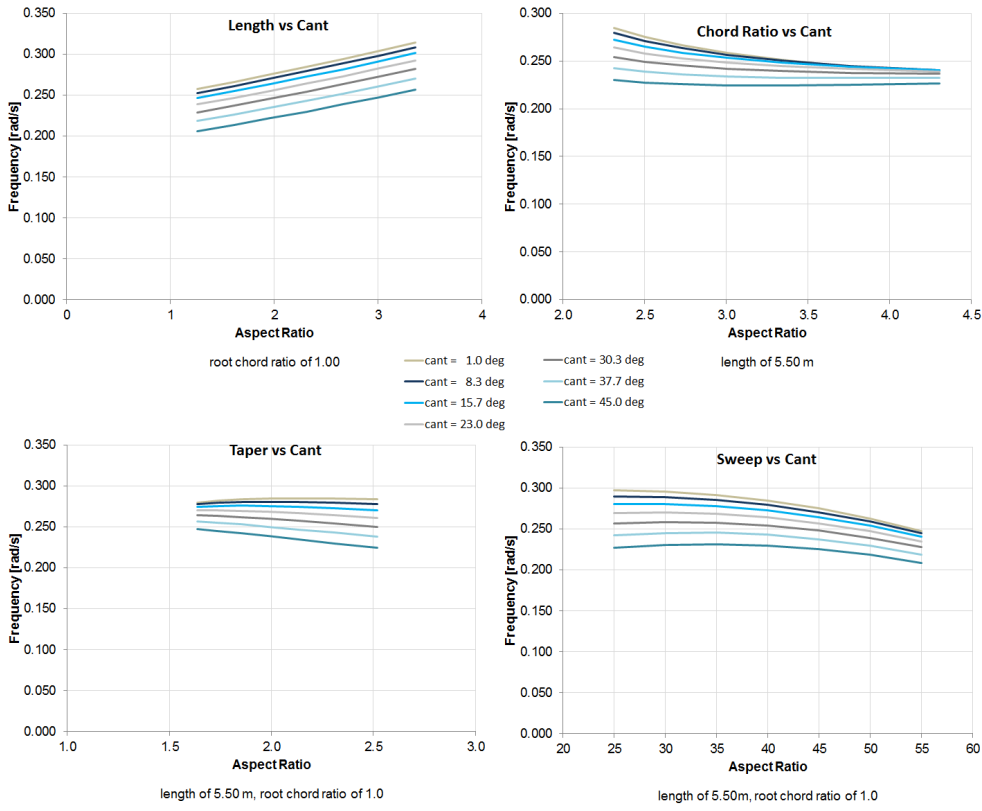


Figure 8.23: An isolated overview of the effect of the various geometric parameters on the dutch roll frequency

8.2. Winglet Optimization

The previous section provided insight into the behaviour of the various parameters, as mapped by the response surfaces. In this section these maps will be used to identify the best winglet configuration for a number of design objectives. Chapter 5.1 differentiates between the so-called limiting, and optimizing objectives. During the optimization each of the 117649 configurations is tested against the stability and control requirements to verify whether they meet the limiting objectives. The resulting reduced design space is then analysed for each of the optimization criteria. However, at the end of the previous section it was found that none of the winglet configurations meet the dutch roll frequency criterion. Since the tip device appears to have little influence on ω_{dr} , it was opted to disregard the dutch roll as a limiting objective and introduce it as part of the optimization.

Of the 117649 configurations 15407 provide satisfactory stability and control. Amongst these viable solutions are a wide range of geometric combinations. This can be seen from figure 8.24 by the large variety for both the aerodynamic ratio and the structural wing weight fraction. The image also indicates the relative position of the optimized winglets. It was found that MTOW and DOC coincide and are, therefore, plotted on top of each other. From the plot it can be observed that both optima for MTOW and DOC gravitate towards the aerodynamic maximum. Due to the baseline's 14000 km mission, the economic impact of the fuel usage becomes more prominent. Since the fuel consumption for long-range commuters is largely dependent on the aerodynamic performance, LD becomes dominant. The geometric properties corresponding to each of the optimization objectives can be found in table 8.1.

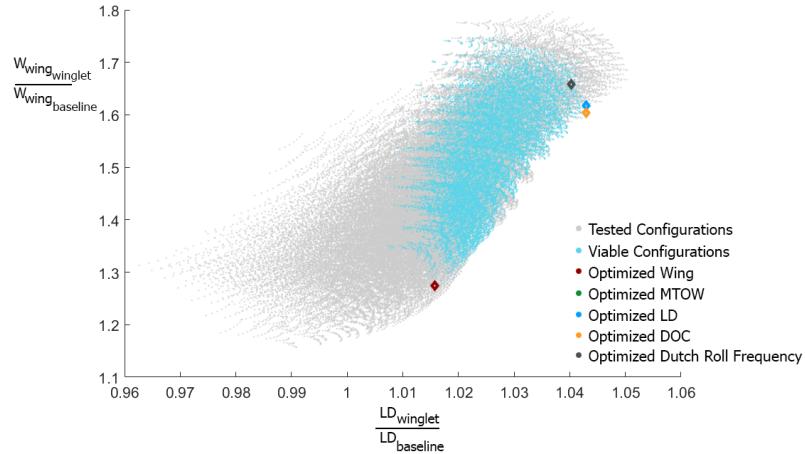


Figure 8.24: Overview of the tested samples

Table 8.1: Geometry of the optimized configurations

	l_w [m]	φ [deg]	Δ_w [deg]	cr_w [-]	λ_w [-]	H_w [-]
minimum W_{wing}	3.00	8.3	35.0	0.55	0.30	0.38
minimum MTOW	6.33	45.0	40.0	1.00	0.30	0.38
maximum LD	6.33	45.0	45.0	1.00	0.30	0.30
minimum DOC	6.33	45.0	40.0	1.00	0.30	0.38
maximum ω_{dr}	8.00	45.0	30.0	1.00	0.53	0.72

The response surface estimates of the stability and control characteristics for each of the objectives are listed in table 8.2. The negative value for $C_{n\beta}$ indicates that the baseline aircraft is statically unstable. In the previous section, figures 8.12-8.14, the stabilizing effect

of winglets has been demonstrated. Similar observations resulted from studies investigating the effect of winglets on classical tube-and-wing aircraft [38, 39]. From the table it can be observed that to minimize the wing weight a small, near vertical tip device was selected. The relative small surface area will produce limited lateral forces, which corresponds to the low values for the moment and force coefficients due to sideslip. These values are increased for the larger surfaces found for the remaining optimization objectives. A comparison of the optimization criteria is provided in table 8.3. The comparison reveals that despite the significant increase in W_{wing} , MTOW is reduced for all configurations.

Table 8.2: Stability and control parameters of the optimized configurations

	C_{n_β} [-]	C_{l_β} [-]	C_{Y_β} [-]	$C_{n_{\delta_r}}$ [-]	$\delta_{r_{cw}}$ [deg]	T_{rm} [s]	ζ_{dr} [-]	ω_{dr} [rad/s]
baseline	-0.0132	-0.0662	-0.0110					
minimum W_{wing}	0.0012	-0.0783	-0.0510	-0.0056	24.6	0.32	0.057	0.212
minimum MTOW	0.0087	-0.1306	-0.0729	-0.0157	23.5	0.25	0.162	0.235
maximum LD	0.0064	-0.1215	-0.0653	-0.0130	23.3	0.26	0.152	0.229
minimum DOC	0.0087	-0.1306	-0.0729	-0.0157	23.5	0.25	0.162	0.235
maximum ω_{dr}	0.0273	-0.1652	-0.1239	-0.0325	24.6	0.23	0.329	0.258

Table 8.3: Optimization parameters of the optimized configurations

	W_{wing} [kg]	%	MTOW	[kg]	%	LD	[%]	DOC	[\$]	[%]
baseline	16837		2.0997E+06			27.48		2.2653E+07		
minimum W_{wing}	21466	127.49	2.0894E+06	99.51	28.28	102.90	2.2635E+07	99.92		
minimum MTOW	27014	160.44	2.0616E+06	98.19	29.04	105.66	2.2531E+07	99.46		
maximum LD	27230	161.73	2.0627E+06	98.24	29.04	105.66	2.2539E+07	99.50		
minimum DOC	27014	160.44	2.0616E+06	98.19	29.04	105.66	2.2531E+07	99.46		
maximum ω_{dr}	27924	165.85	2.0724E+06	98.70	28.96	105.39	2.2595E+07	99.74		

Since the limiting HQL can be set by the user, the program is used to determine the influence of this handling characteristic on the performance of the aircraft. For the current analysis, which is limited to the roll mode and spiral, it was found that the presented optima already correspond to an HQL of 1. However, when the program is expanded and additional objectives have been defined, the winglet design tool could be utilized to analyse the structural, aerodynamic, or economic impact of a design requirement.

The accuracy of the response surface estimates is analysed by generating aerodynamic models for each of the 5 configurations. The results of this exercise are presented in table 8.4 and 8.5. As explained in Chapter 7, the large deviation found for the weathercock stability can partly be attributed to the size of C_{n_β} . Another cause for the discrepancies found in table 8.4 is the sensitivity to minor pressure variations of the skewed cells at centre body. The position of the configuration within the design space has an impact as well. Since the response surface utilizes neighbouring samples to estimate the characteristics at a specified local, the average error is often relatively large near the boundaries of the design space. This effect is most visible for the LD and dutch roll frequency configuration. Further limitations of the method can be related to its mathematical representation of a system. Response surfaces attempt to capture the underlying behaviour using smooth, continuous relationships. However, if a parameter is dependent on a large number of variables or demonstrates erratic behaviour, it becomes increasingly more difficult to accurately construct a surface, as is evident from the deviation in $\delta_{r_{cw}}$. These relative large errors indicate the need for further research into the applicability of response surfaces during the optimization process.

Table 8.4: Stability and control parameter comparison to VSAero model

	ΔC_{n_β} [%]	ΔC_{l_β} [%]	ΔC_{Y_β} [%]	$\Delta C_{n_{\delta_r}}$ [%]	$\Delta \delta_{r_{cw}}$ [%]
minimum W_{wing}	-20.00	-0.83	-4.14	-22.51	165.87
minimum MTOW	-39.65	0.22	-16.95	-1.84	-40.41
maximum LD	-50.34	-21.86	-21.77	-6.47	-40.75
minimum DOC	-39.65	0.22	-16.95	-1.84	-40.41
maximum ω_{dr}	36.51	38.60	21.93	5.93	-13.45

Table 8.5: Optimization parameter comparison to VSAero model

	ΔW_{wing} [%]	$\Delta MTOW$ [%]	ΔLD [%]	ΔDOC [%]
minimum W_{wing}	-2.15	0.78	-0.85	0.36
minimum MTOW	-2.44	-0.19	0.02	-0.12
maximum LD	-1.04	-0.14	-0.38	0.14
minimum DOC	-2.44	-0.19	0.02	-0.12
maximum ω_{dr}	-2.48	0.33	-0.64	0.22

The sensitivity study and the results presented in table 8.4 illustrate the difficulties of the response surface to accurately capture the behaviour of some parameters. In recognition of these inaccuracies, a secondary analysis is performed using the original 400 data samples. During the process 2 of the 400 samples were corrupted, leaving 398 viable configurations. Analysis reveals that 60 out of the 398 options meet the limiting objectives. From this reduced database the best samples with respect to the optimization criteria have been selected and are tabulated in table 8.6.

Table 8.6: Geometry of the best samples

	l_w [m]	φ [deg]	Λ_w [deg]	cr_w [-]	λ_w [-]	H_w [-]
minimum wing weight	4.30	3.6	32.9	0.8991	0.9185	0.5985
minimum MTOW	7.87	44.3	45.9	0.8720	0.4875	0.3303
maximum LD	7.87	44.3	45.9	0.8720	0.4875	0.3303
minimum DOC	3.53	28.1	46.2	0.7647	0.3210	0.3419
maximum ω_{dr}	6.34	44.7	30.5	0.6569	0.9423	0.6306

It is to be noted that the geometry for both MTOW and LD are equal. In contrast to the optimization process, the best configuration found with respect to the cost does not coincide with MTOW. This can be explained by the limited number of samples and the dependency of the direct operating cost on the structural weight, Appendix B.4.

The stability and control parameters corresponding to the best samples are tabulated in table 8.7 and visualized in figure 8.25. From the plots it can be seen that the winglet corresponding to the minimum wing weight has the strongest C_{n_β} . Due to its nearly vertical orientation, the 4.30 m winglet is able to produce significant lateral forces. The plot also demonstrates the minor destabilizing effect of the MTOW and LD winglet on the effective dihedral. In section 8.1.2 it was indicated that C_{l_β} is dependent on a number of aspects. Further investigation is needed to isolate the phenomena responsible for this destabilizing effect.

Table 8.7: Stability and control parameters of the best samples

	$C_{n\beta}$ [-]	$C_{l\beta}$ [-]	$C_{Y\beta}$ [-]	$C_{n\delta_r}$ [-]	$\delta_{r_{cw}}$ [deg]	T_{rm} [s]	ζ_{dr} [-]	ω_{dr} [rad/s]
baseline	-0.0132	-0.0662	-0.0110					
minimum wing weight	0.0254	-0.0978	-0.1204	-0.0195	20.53	0.71	0.112	0.211
minimum MTOW	0.0041	-0.0618	-0.0593	-0.0172	10.31	0.24	0.162	0.160
maximum LD	0.0041	-0.0618	-0.0593	-0.0172	10.31	0.24	0.162	0.160
minimum DOC	0.0033	-0.0935	-0.0571	-0.0078	18.33	0.28	0.099	0.215
maximum ω_{dr}	0.0076	-0.1304	-0.0695	-0.0188	17.62	0.35	0.168	0.280

Table 8.8: Optimization parameters for the best samples

	W_{wing} [kg]	MTOW [%]	LD [%]	DOC [\$]	DOC [%]
baseline	16837		27.48	2.265E+07	
minimum wing weight	21657	128.63	27.99	2.276E+07	100.48
minimum MTOW	28639	170.09	29.08	2.257E+07	99.63
maximum LD	28639	170.09	29.08	2.257E+07	99.63
minimum DOC	23778	141.23	28.70	2.255E+07	99.54
maximum ω_{dr}	27263	161.92	28.33	2.282E+07	100.75

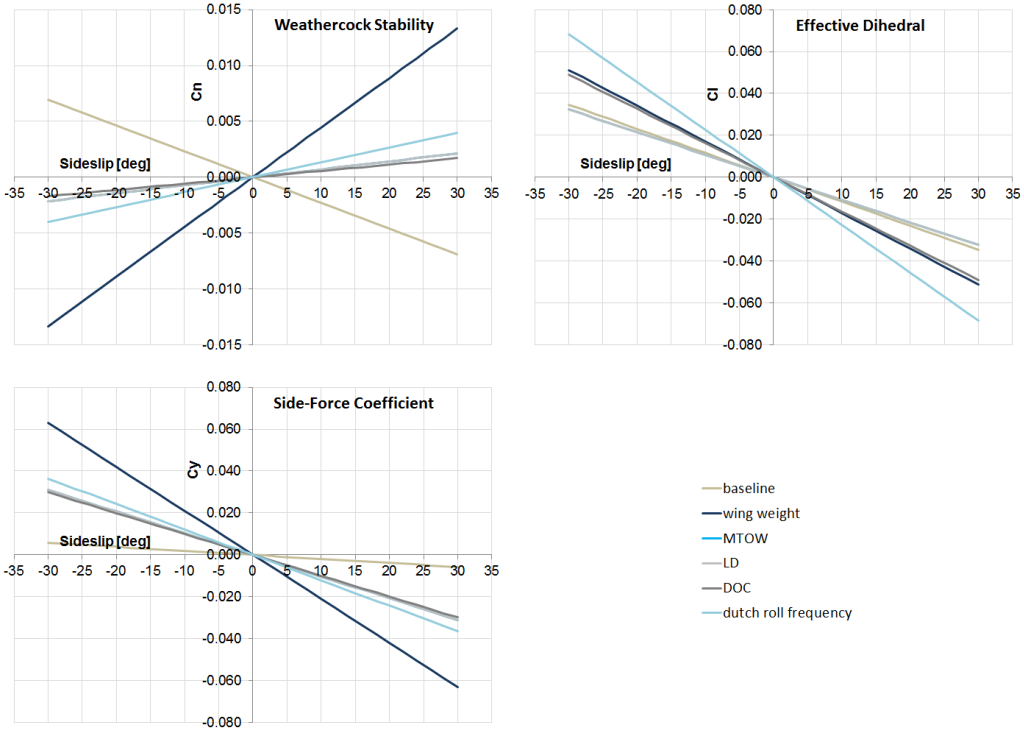


Figure 8.25: Overview of the stability characteristics for sideslip

A linearisation of the stability and control characteristics is used to establish the behaviour of the aircraft. To investigate the accuracy of the method, the linearised model for C_n , C_l , and C_Y is compared to the non-linearised properties corresponding to a range of sideslip angles. It is to be noted that the linearised models are based on the aerodynamic analysis of the aircraft at an angle of attack of zero. An additional curve has been added to figure 8.26 to establish the influence of a change in α . The figure illustrates the validity of the linearisation and demonstrates a particularly good approximation for C_l . The minor deviation found for C_n and C_Y at large angles of sideslip can be attributed to the size of

the parameters and the relative small angle used to ascertain the linearised values. However, the flow appears to remain attached, even at maximum sideslip angles. Hence, the stall criterion listed in Chapter 3 is met.

Another important conclusion to be drawn from figure 8.26 is the significant impact of α on the stability characteristics. Therefore, it is recommended to investigate the implementation of empirical models to account for this variation in slope. Although additional simulations could capture the change due to α , empirical models are preferred as they limit the required computational time.

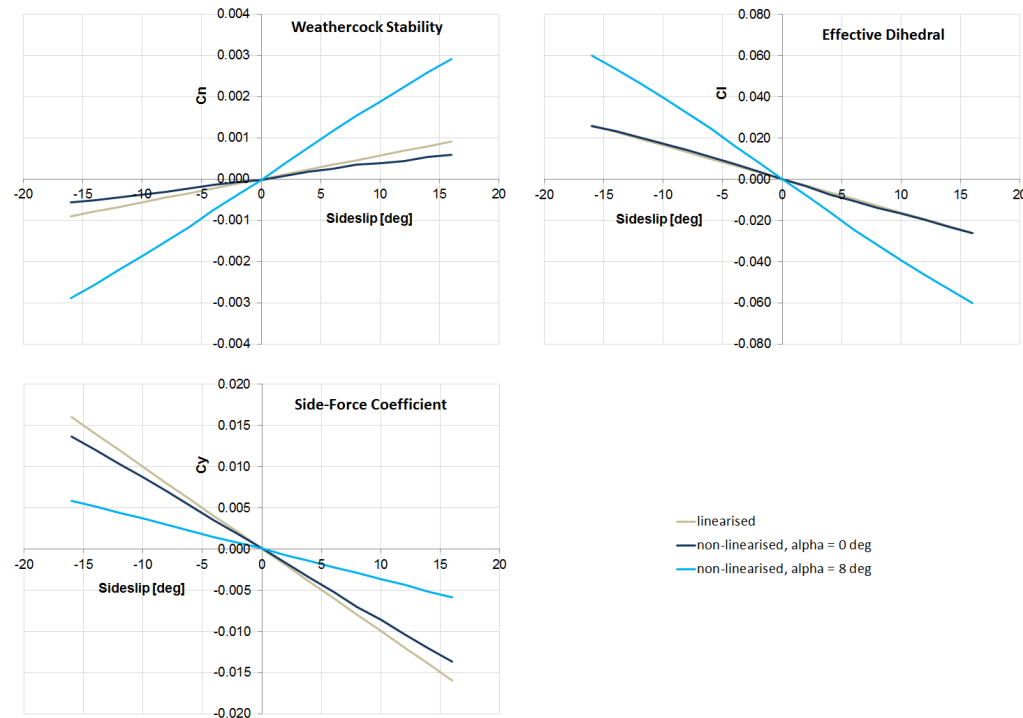


Figure 8.26: Comparison between the linearised and non-linearised stability characteristics for sideslip

The non-linear behaviour of the control power is analysed and compared to its linear counterpart, figure 8.27. The presented results are based on α equals zero and two values for β . Up to deflection angles of approximately 8 degrees the power curve for zero sideslip shows near linear behaviour. Beyond this angle the non-linearities in the flow decrease the available control power. At δ_r equals 30.0 degrees the deviation between the two models was found to be 24.2%. Despite this reduction in control power, the aerodynamic computations indicate that the flow is still able to remain attached. A similar exercise was performed at maximum sideslip. Sideslip alters the angle of attack of the winglet, effectively translating the power curve downward. It can be seen that the control power shows some irregularities for large, negative deflections. These variations are an indication that the aerodynamic solver has not yet fully converged, which is most likely due to minor flow separation. Analysis of the available control power at 30.0 degrees deflection yields a deviation of 44.7%. Assuming the ailerons are able to counteract the rolling moment, the non-linear rudder deflection angle to achieve trim is computed to be 26.8 degrees. Although this is beyond the threshold of the limiting criterion, the rudder demonstrates that it is still capable of generating additional power.

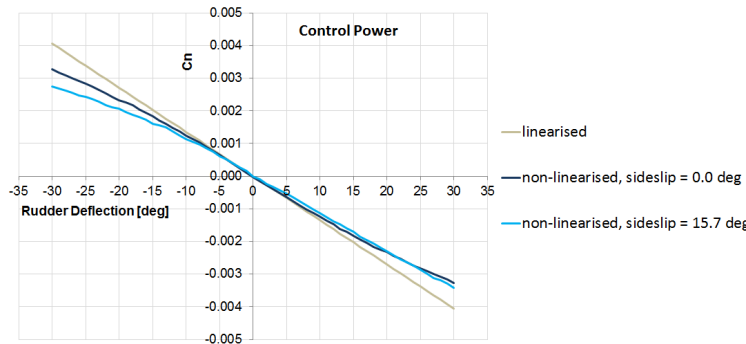


Figure 8.27: Comparison between the linearised and non-linearised DOC control power

This chapter demonstrated the ability of the program to analyse the influence of the individual winglet design variables. The identified behaviour of the various parameters was utilized to optimize the tip device with respect to 5 optimization objectives. However, the relative large error for some of these parameters, as caused by the response surfaces, indicates the need for further research into the applicability of the method. Therefore, a secondary analysis was performed based on the 400 tested configurations. The results indicate that the aerodynamic performance, MTOW, and direct operating cost can be improved by employing yaw-control incorporated winglets, despite the significant increase in W_{wing} .

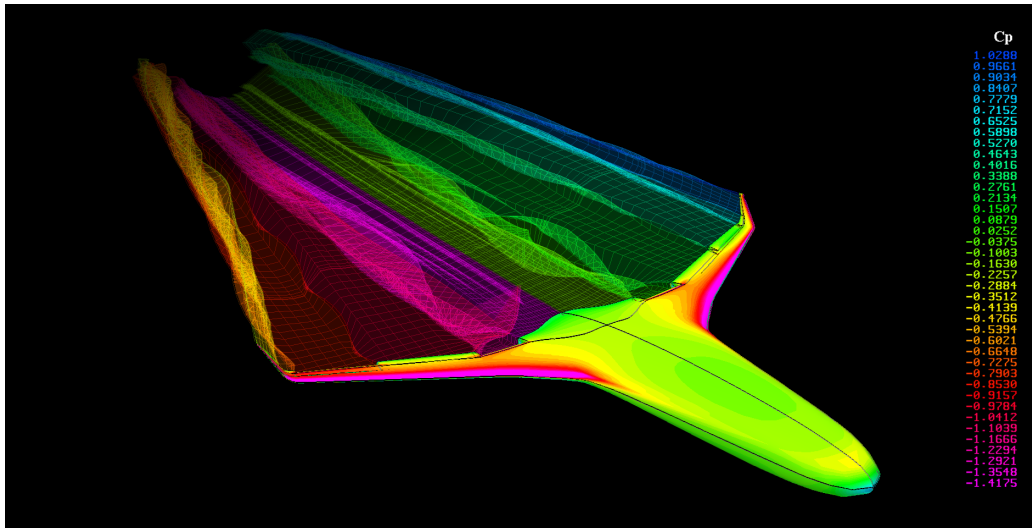


Figure 8.28: Isometric view of the best sample DOC configuration at an angle of attack of 4.9 degrees

9

Conclusion and Recommendations

The devised design methodology has been successfully implemented to create a program capable of exploring various control surface configurations. Based on user-input the program automatically generates a specified number of geometries that span a pre-defined design space. These samples are analysed using a first order panel method to establish the aerodynamic performance and derive the stability and control derivatives. The aerodynamic loading of each configuration is utilized by a class II & 1/2 wing weight estimation method. Connected to a mission analysis module, the scheme is able to provide information on the structural, and maximum take-off weight. A direct operating cost algorithm employs these values to establish the economic impact of the design. The computed characteristics are then implemented in a virtual test flight program that analysis the behaviour of the baseline BWB aircraft during critical landing conditions. The information gathered for each of the samples was successfully connected to a response surface methodology. The selected methodology allowed the design space to be expanded, enabling the user to map the behaviour of the stability and control characteristics.

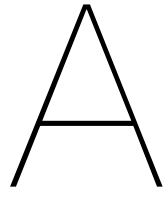
Validation of the program was done in twofold. First the aerodynamic panel method had been validated using test data from the Fokker 100 and Learjet Model 23. Secondly, the winglet design program was validated as a whole, by comparing the behaviour of the aerodynamic performance and structural wing weight to literature. Once the program had been validated, it was employed to analyse 400 unique yaw-control incorporated winglet configurations. The influence of each of the 6 winglet design variables that comprise the design space had been analysed for: LD, W_{wing} , $C_{l\beta}$, $C_{Y\beta}$, $C_{n\delta_r}$, and the eigenvalues of the asymmetric eigenmodes. However, research indicated that none of the tested winglet configurations met the dutch roll frequency requirement set forth by the handling quality level criterion. Since the tip device appeared to have little influence on ω_{dr} , it was opted to disregard the dutch roll as a limiting objective and introduce it as part of the optimization.

It was found that the accuracy of the program was largely dependent on the capability of the response surface to capture the behaviour of the individual parameters. To establish the accuracy, 40 randomly generated winglet configurations were analysed and compared to the response surface estimates. The estimates for the aerodynamic performance, structural wing weight, and operating cost displayed an average error of less than 1.0%. Larger deviations were found for parameters characterized by values that approach zero. The largest deviation was found for λ_{sp} and $C_{n\beta}$ with an average error of 58.0% and 35.2% respectively. Normalization of these values had little influence on the accuracy. Therefore, further research is needed to reduce the error caused by the response surfaces.

The behaviour, as identified by the response surfaces, was utilized to optimize the tip device with respect to 5 optimization objectives. However, in recognition of the inaccuracies of the method, a secondary analysis was performed based on the original 400 samples. The results indicated that the aerodynamic performance, MTOW, and direct operating cost can be improved by employing yaw-control incorporated winglets, despite the significant increase in W_{wing} . To conclude, the devised program successfully mapped the behaviour of the stability and control parameters and could provide the first step towards the generation of less computational intensive models, if the accuracy of the response surfaces could be improved.

Apart from the need to improve the accuracy of the response surface, the research identified other aspects that should be further developed to progress the winglet design program. This leads to the following recommendations:

- For stability analysis, the program utilizes the linearised equations of motion. Analysis of the results illustrate the validity of the linearisation and suggests that better estimates can be obtained by selecting a larger value for $\Delta\beta$ and $\Delta\delta_r$. It also demonstrates the influence of a change in angle of attack, that should be accounted for by either empirical models or additional simulations.
- Investigation into the influence of the design variables on the dutch roll frequency revealed that none of the tested configurations meet the requirement set forth by the handling quality criterion. It was found that the non-planar component had little effect on ω_{dr} . Therefore, the baseline aircraft needs to be modified to establish its impact on this stability characteristic. Once the design space includes viable options, the dutch roll can be reinstated as a limiting objective.
- One of the requirements listed for a vertical fin or winglet is the need to postpone stall beyond the maximum sideslip angle. During the research this criterion had been validated for an individual configuration. However, connecting an empirical model, able to accurately predict stall, would expand the capabilities of the program and would lead to a more complete system.
- During the mission analysis the computed lift over drag ratio is used to estimate the fuel usage. As the aerodynamic performance is dependent on the density and Mach number, the computed ratio established during low speed flight will not properly reflect the performance during cruise. Therefore, the use of an additional program, able to compute the aerodynamic properties during cruise, is recommended.
- The aircraft configurations that can be analysed by the winglet design program is currently limited by the mesher embedded in the multi-model-generator. Expanding the capabilities of the mesher would significantly improve the flexibility of the program and will reduce the required computational time.



Baseline Aircraft

The AHEAD multi-fuel blended wing body, MF-BWB, aircraft has been developed at the faculty of Aerospace Engineering at Delft University of Technology. The high level characteristics of aircraft are listed in this appendix. It will also provide all the data needed to analyse and design a yaw-control incorporated winglet.

Table A.1: *High level mission requirements of the AHEAD MF-BWB*

Parameter	Unit
<i>passengers</i>	300 [-]
<i>payload</i>	39950 [kg]
<i>range</i>	14000 [km]
<i>altitude</i>	11.00 [km]
<i>Mach</i>	0.80 [-]
<i>fuel ratio</i>	0.80 [-]
<i>primary fuel</i>	LNG

Table A.2: *Weight break-down of the MF-BWB preliminary design study*

Parameter	Unit
W_0	222775 [kg]
<i>OEW</i>	107027 [kg]
$W_{payload}$	39950 [kg]
$W_{f_{LNG}}$	64607 [kg]
$W_{f_{ker}}$	16152 [kg]
$W_{f_{tank}}$	1936 [kg]
W_{engine}	6350 [kg]

Table A.3: *Centre of gravity and inertias of the MF-BWB preliminary design study*

Parameter	Unit
$CG_{x_{aircraft}}$	26.51 [m]
I_{xx}	11960000 [kg m ²]
I_{yy}	30960000 [kg m ²]
I_{zz}	42320000 [kg m ²]
I_{xz}	226992 [kg m ²]

Table A.4: Planform parameters and aerodynamic properties of the MF-BWB preliminary design study

Parameter		Unit
c_r	48.0	[m]
MAC	24.50	[m]
b	68.0	[m]
S_{wing}	845.0	[m^2]
S_{canard}	102.0	[m^2]
S_{ref}	947.0	[m^2]
A	6.57	[–]
C_{L_0}	0.155	[–]
$C_{L_{max}}$	0.800	[–]
C_{L_α}	6.050	[rad^{-1}]
C_{D_0}	0.0059	[–]
e	0.692	[–]

The multi-model-generator requires detailed information on the planform to construct the model. The leading and trailing edge coordinates used to generate the MF-BWB are tabulated in table A.5. The table also notes the local quarter chord twist. A constant dihedral angle of 2.02 degrees is applied to the 2-dimensional representation. It had already been indicated in Chapter 5 that the NACA/Langley N0011SC supercritical airfoil was employed. A top view of the aircraft can be found in figure A.1.

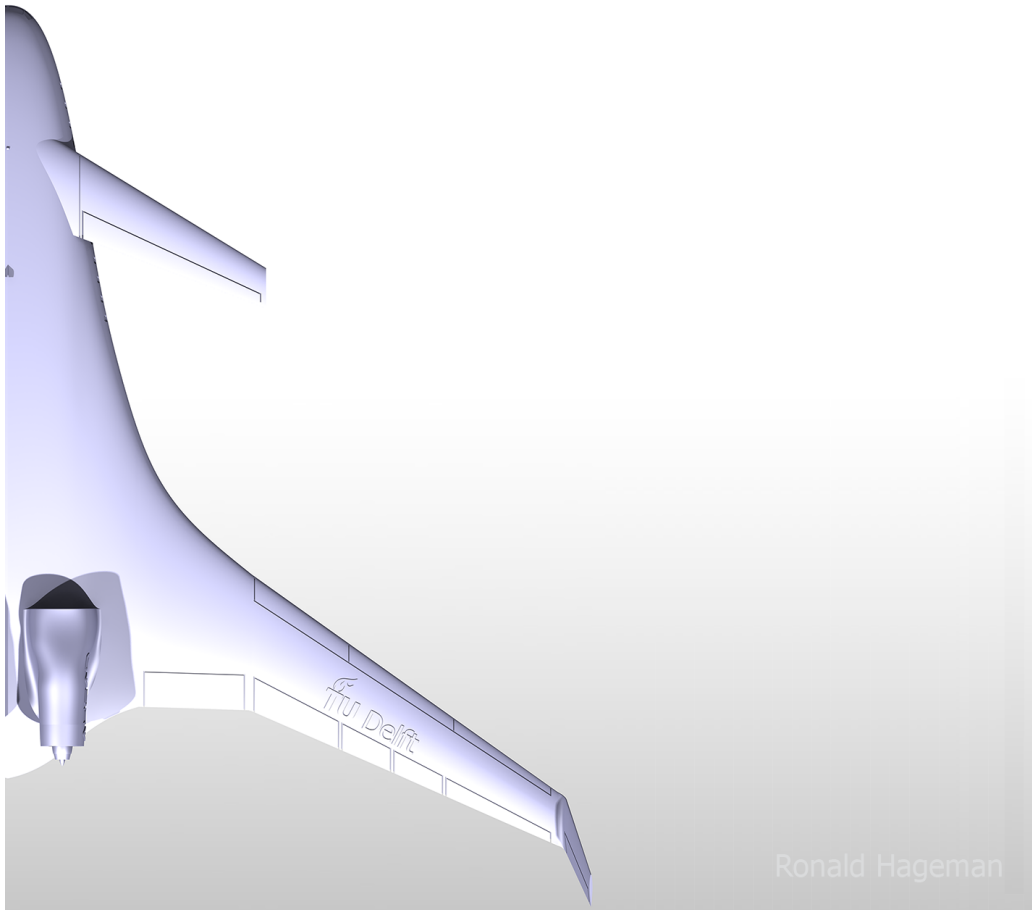


Figure A.1: Top view of the preliminary AHEAD multi-fuel BWB

Table A.5: *Planform coordinates and quarter chord twist angle*

<i>Leading Edge</i>		<i>Trailing Edge</i>		<i>Twist</i>
<i>x</i>	[m]	<i>y</i>	[m]	[deg]
0.00	0.00	48.00	0.00	1.530
0.02	0.40	47.98	0.40	1.530
0.07	0.60	47.96	0.60	1.530
0.16	0.80	47.91	0.80	1.530
0.57	1.40	47.71	1.40	1.530
1.04	1.80	47.50	1.80	1.530
2.11	2.40	47.10	2.40	1.530
3.14	2.80	46.85	2.80	1.602
5.69	3.40	46.43	3.40	1.709
11.51	4.50	45.59	4.50	1.907
17.15	5.50	44.90	5.50	2.029
24.86	7.00	44.16	7.00	2.125
26.61	7.50	43.99	7.50	2.157
28.18	8.00	43.85	8.00	2.267
29.65	9.00	43.85	9.00	2.488
31.62	11.00	43.85	11.00	2.929
33.56	13.00	43.85	13.00	3.369
34.39	14.00	43.85	14.00	3.590
35.20	15.00	43.85	15.00	3.810
35.38	15.25	43.96	15.25	3.760
35.56	15.50	44.08	15.50	3.710
36.28	16.50	44.53	16.50	3.509
36.44	16.73	44.64	16.73	3.462
37.33	17.97	45.19	17.97	3.215
38.21	19.20	45.75	19.20	2.968
39.09	20.43	46.31	20.43	2.721
39.98	21.67	46.87	21.67	2.473
40.86	22.90	47.43	22.90	2.226
41.74	24.13	47.99	24.13	1.979
42.63	25.37	48.54	25.37	1.731
43.51	26.60	49.10	26.60	1.484
44.39	27.83	49.66	27.83	1.237
45.28	29.07	50.22	29.07	0.989
46.16	30.30	50.78	30.30	0.742
47.04	31.53	51.34	31.53	0.495
47.93	32.77	51.89	32.77	0.247
48.81	34.00	52.45	34.00	0.000

B

Components

The winglet design program consists of a number of components dedicated to a specific task. In this appendix the high-level functionalities and architecture of these components will be described. For a more detailed presentation of the programs, the reader is referred to the listed papers and manuals.

B.1. Multi-Model-Generator

The multi-model-generator is an initiative by the TU Delft, resulting in a program able to generate and analyse various aircraft configurations during the early stages of design. Originally based on the ICAD design platform, the knowledge based engineering method utilized 4 elementary building blocks to generate an aircraft. These primitives consist of: wing-trunk; fuselage-trunk; engine part; and connection element. Depending on the level of detail provided by the user, the program is able to translate the geometry into a format compatible with discipline-specific analysis software.

In 2002 the ICAD platform was acquired by Dassault Systemès. Due to the unavailability of the platform, it was opted to re-initiate the project, translating it to a similar knowledge based system. The development of the new MMG led to a program that focussed on the wing-, and fuselage-trunk. The design program was capable of modelling an arbitrary aircraft with or without slotted moveables. However, as the selected Genworks GDL platform evolved, some of the functionalities of the program were lost. As a result the MMG was no longer able to perform adequately, leading to another translation.

The compatibility and limitations of the Genworks model instigated the transition to Python. The translation to this open source platform has been initiated recently. Therefore, the program is still being developed and many of the functions embedded in the original code are still missing. The primary attributes of the wing-, and fuselage-trunk have already been scripted, allowing the user to generate a large variety of aircraft. Although the geometric models can be acquired, the connection to discipline-specific software, such as VSAero, is limited. These limitations are caused by the discretization strategy employed to generate the mesh. As a result, the program is currently limited to wing or fuselage-wing configurations.

The object based code employs so-called .JSON-files to generate the aircraft. These files adhere to a tree-like structure in which the individual components are described using keywords. The MMG links these keywords to the various objects that define the wing or fuselage. To generate such a component, the user is to provide data on the bounds, or rails, of the part. For a wing the rails comprise of a 2-dimensional representation of the leading, and trailing edge. Once details on the twist, dihedral, and the airfoil sections have been processed, the 2-dimensional layout is translated to a 3-dimensional geometry. This geometry can be visualised and inspected using the proprietary ParaPy platform.

An additional layer is created when the wing is to contain control surfaces. Chapter 6 introduced the 3 different methods available to construct moveables. Each of the options requires a description of the clean wing, which is to be decomposed into a number of sections. Depending on the selected option, the program will rotate the local normal-vector or the actual geometry, according to the input provided by the .JSON-file.

The resulting geometric model can be exported as a .stp-file or processed for discipline-specific analysis. Currently the post-processing ability of the system is limited to provide input for VSAero. This requires the model to be discretized into a number of panels. Therefore, the program connects to the open source software package Salomé. Salomé is able to construct a variety of surface grids, based on a high-level meshing strategy embedded in the MMG. Apart from the surface grid, the program requires a description of the progression of the wake. Each discontinuity at the trailing edge of the wing will produce a so-called wake-line, that provides a first estimation of the shape of the wake. The reader is referred to reference [29] for further information on the capabilities and limitations of the MMG.

The MMG, still being in an early stage of development, is able to generate geometric models for a vast variety of aircraft and has the potential to bridge the gap between model generation and discipline-specific analysis.

B.2. VSAero

Founded on potential flow theory, VSAero is capable of establishing the aerodynamic properties of any arbitrary object submerged in a low velocity flow. In contrast to vortex lattice methods, which represents a 3-dimensional shape as a 2-dimensional lifting surface, panel methods discretize the actual geometry. As the resultant surface grid utilizes sources, sinks, and doublets to model the vorticity of each of the panels, the panel method is applicable to both lifting, and non-lifting surfaces. The Fortran based program employs the Neumann boundary condition to solve for the perturbation potential given by Green's Identity [30]. This architecture enables VSAero to account for more complex features, such as jet flows, by modifying the local boundary conditions.

Originally the code was written as a first-order panel method, neglecting higher-order terms for the unknown source strength [28]. Over the years the available computing power increased significantly, leading to the incorporation of these additional terms. The development of this multi-order aerodynamic solver resulted in a hybrid scheme that distinguishes between thick and thin surfaces ($t/c < 0.01$). By adopting different mathematical expressions for these surfaces, the system became better able to predict the behaviour of the wake. Apart from its effect on the wake, the modified program also demonstrates improved predicting capabilities for thin body models. Since each of the panels will induce a velocity on their neighbouring panels, the increase in accuracy is also visible in compound models [28].

To expand the scope of the panel method, VSAero couples viscous computations to potential flow. A variety of viscous models is readily available, as are the methods in which they are integrated. All these options can be selected in the VSAero operating file. This file adheres to a card based system, where each card corresponds to a specific topic and follows a predefined format. Only a limited number of cards will be discussed in this report. For further information on the program and the operating file, the reader is referred to reference [30]. The VSAero operating file starts with a slot in which the user can list information he or she deems important. This text based entry slot does not adhere to a predefined format and won't have any influence on the simulation. The second card enables the user to select the data to be printed in the output files and will determine the available post-processing methods. It had already been noted that VSAero has the capability to incorporate viscous models. These models can be set in card 4, together

with the number of wake, and viscous/potential iterations. Once an appropriate number of iterations has been specified, the user is to provide information on the onset conditions, card 6, and the reference values utilized to non-dimensionalize the forces and moments, card 7. Amongst the options is the ability to set the operating velocity, orientation, and the different body rates. Card 6 also includes the option to define a mathematical model to account for compressibility effects. However, the most important slot is card 8. This card lists the geometry of the model and specifies the mathematical solver. In Chapter 7 it had been indicated that VSAero incorporates both direct, and iterative solvers to resolve the system of unknown source strengths. Reference [30] states that the robust direct solver LAPACK produces the best results, especially for models comprising of a limited number of panels. As the number of panels increase, the required computational time grows exponentially and iterative solvers might prove to be a better solution. For more complex configurations, such as models including rotors or propellers, more dedicated solvers can be employed.

The VSAero computation produces 3 files. The most interesting of these output files is the *.OUT*-file, which contains all information requested by the users in slot 2. This text-based file can be connected to a post-processing algorithm to automatically structure and process all data. A second file structures the computed data to be compatible with Omni3D. This program allows the user to visualize the various parameters by projecting them on the 3-dimensional model, or by plotting them in a 2-dimensional graph. The final file has the extension *.RES* and can be used to continue the computations if the obtained level of convergence is insufficient.

The capabilities and mathematical models embedded in the multi-order panel method are vast and a detailed overview is beyond the scope of this report. Therefore, the reader is referred to reference [30] for further information on VSAero.

B.3. EMWET

EMWET, the *Elham Modified Weight Estimation Technique*, is defined as a class II & 1/2 wing weight estimation method. The method, as described in reference [32], combines an analytical approach for the wing box with empirical relations for other components, such as joints and control surfaces. According to the authors, the geometric model used in similar methods is crude and does not accurately represent the wing. The research also revealed that the aerodynamic loads used to compute the wing weight does not properly reflect the actual loading. As a result, the wing box could not be properly analysed, leading to discrepancies in the weight estimation.

To overcome these problems, EMWET connects to an aerodynamic solver capable of deriving the spanload and local pitching moment. For the presented project VSAero was selected, however, generally the class II & 1/2 weight estimation method employs Q3D. The quasi-3-dimensional aerodynamic solver is able to utilize the geometric input for EMWET to ascertain an accurate representation of the load case for the actual wing.

Another distinct difference is that EMWET utilizes a newly defined efficiency parameter to account for the curvature of the top and lower surface of the wing. By introducing this so-called *airfoil effective distance*, EMWET relates the size of the wingbox to the actual shape of the wing sections. To simplify the computations, the *effective distance* is utilized to represent the upper and lower panel by two flat plates. It is assumed that these panels are to withstand the bending moment, whereas the spars are sized to cope with the shear loads. The components are sized iteratively to ascertain the structural wing weight. This approach enables the program to account for load relief caused by engines and the wing itself. For further information on the program, the reader is referred to reference [32].

The method had been validated against various types of aircraft of different manufacturers and showed an average error of less than 2% for conventional aluminium based commuter aircraft. Due to the short computation time and high level of accuracy, the EMWET method provides an excellent structural platform to be used in the winglet optimization.

B.4. DOC

The design process is not only subject to compromise on a technical level, the economic impact should also be included in the analysis. In 1944 the Air Transportation Association of America, ATA, presented a universally recognized method to predict the cost known as the *direct operating cost*, DOC. As the world of aviation evolved, so did the cost analysis method. The model was progressively modified and updated to reflect the economic break-down of modern airliners. The computation scheme embedded in the winglet design tool is based on the scheme prescribed by Liebeck et al [33]. The model was composed by a collaboration between Boeing, NASA, and McDonnell Douglas. The scheme added interest cost, as well as landing fees, navigation fees and cabin crew cost to the original ATA model.

The widely recognized economic estimation technique consists of *cash costs* and *ownership costs*. A further decomposition yields the following economic elements that have to be taken into account: [33]

1. Flight Crew
2. Cabin Crew
3. Landing Fees
4. Navigation Fees
5. Maintenance - Airframe
6. Maintenance - Engine
7. Fuel
8. Depreciation - Aircraft and Spares
9. Insurance
10. Interest

The first 7 components are associated with the *cash costs*, while the remainder is known as the *ownership costs*. Although the research of the impact of winglet design is limited to the change in DOC, all components have been included to increase the flexibility of the program.

The *cash costs* can directly be derived from the high level requirements and weight breakdown obtained from the *Mission Analysis* module. The flight crew and cabin crew costs are computed on a annual basis. Their contributions are identified to be:

$$\text{Flight Crew} = 482 + \frac{\text{MTOW}}{1000} \text{BH FC} \quad (\text{B.1})$$

$$\text{Cabin Crew} = 78 \frac{\text{seats}}{30} \text{BH FC} \quad (\text{B.2})$$

In the equations *BH* is the block hours and *FC* the number of flight cycles per year. It is to be noted that, due to its origin, *MTOW* is to be translated into pounds. The expressions for the landing and navigation are listed to equal:

$$\text{Landing Fees} = 4.25 \frac{MTOW}{1000} FC \quad (\text{B.3})$$

$$\text{Navigation Fees} = 0.136 \cdot 500 \sqrt{\frac{MTOW}{1000}} FC \quad (\text{B.4})$$

The contribution of the maintenance components consists of a labour and a material component. A third component is added to account for the overhead and is defined as twice the direct labour cost resulting in the following airframe maintenance costs:

$$\begin{aligned} \text{Airframe Labour} &= \left(1.26 + \frac{1.774 AFW}{10^5} - 0.1071 \left(\frac{AFW}{10^5} \right)^2 \right) BH \\ &\quad + \left(1.614 + \frac{0.7227 AFW}{10^5} + 0.1024 \left(\frac{AFW}{10^5} \right)^2 \right) \end{aligned} \quad (\text{B.5})$$

$$\begin{aligned} \text{Airframe Material} &= \left(12.39 + \frac{29.8 AFW}{10^5} + 0.1806 \left(\frac{AFW}{10^5} \right)^2 \right) BH \\ &\quad + 15.20 \frac{97.33 AFW}{10^5} - 2.862 \left(\frac{AFW}{10^5} \right)^2 \end{aligned} \quad (\text{B.6})$$

$$\text{Airframe Total} = (3 \cdot 25 \text{ Airframe Labour} + \text{Airframe Material}) FC \quad (\text{B.7})$$

With AFW being the airframe weight defined as the manufacturer's empty weight minus the dry weight of the engines. A similar scheme is devised to derive the engine maintenance cost using the static thrust at sea level, $SLST$, and the number of engines, NE .

$$\text{Engine Labour} = 25 \left(0.645 + \frac{0.05 SLST}{10^4} \right) \left(0.566 + \frac{0.434}{BH} \right) BH NE \quad (\text{B.8})$$

$$\text{Engine Material} = \left(25 + \frac{18 SLST}{10^4} \right) \left(0.62 + \frac{0.38}{BH} \right) BH NE \quad (\text{B.9})$$

$$\text{Engine Total} = (3 \text{ Engine Labour} + \text{Engine Material}) FC \quad (\text{B.10})$$

The fuel cost can simply be computed by multiplying the required fuel volume by the cost as specified by the user.

The *ownership costs* are derived from the airframe cost. A method to estimate the development, testing and production of an airframe is presented by Raymer [1]. The prescribed model is a modified version of the DAPCA IV cost model that decomposes the airframe cost in a number of subcomponents.

$$\text{Engineering Hours} = 4.86 W_e^{0.777} V^{0.894} Q^{0.163} = H_E \quad (\text{B.11})$$

$$\text{Tooling Hours} = 5.99 W_e^{0.777} V^{0.696} Q^{0.263} = H_T \quad (\text{B.12})$$

$$\text{Manufacturing Hours} = 7.37 W_e^{0.82} V^{0.484} Q^{0.641} = H_M \quad (\text{B.13})$$

$$\text{Quality Control Hours} = 0.133 H_M = H_Q \quad (\text{B.14})$$

$$\text{Development Support Cost} = 45.42 W_e^{0.630} V^{1.3} = C_D \quad (\text{B.15})$$

$$\text{Flight Test Cost} = 1243.03 W_e^{0.325} V^{0.822} FTA^{1.21} = C_F \quad (\text{B.16})$$

$$\text{Manufacturing Material Cost} = 11.0 W_e^{0.0921} V^{0.621} Q^{0.799} = C_M \quad (\text{B.17})$$

In the equations W_e is the empty weight, V the maximum velocity in knots, Q the number of aircraft to be produced and FTA being the number of flight test aircraft. The computed

hours are multiplied by the respective average hourly rate and summed together with the remaining costs. To arrive at the cost per aircraft, the total cost needs to be divided by the number of aircraft, resulting in the following expression for the total airframe cost.

$$AFC = \frac{H_E * R_E + H_T * R_T + H_M * R_M + H_Q * R_Q + C_D + C_F + C_M + C_{av}}{Q} \quad (B.18)$$

The parameter R denotes the average hourly rate, while C_{av} is the estimate of the avionics cost. The computed value can be inserted in the expressions for the *ownership cost*, with *Spares* defined as the investment in spares as a percentage of AFC .

$$\text{Depreciation} = (1 - \text{residual}) \frac{AFC}{\text{Period}} + \text{Spares}_{af} \frac{AFC}{\text{Period}} + \text{Spares}_{eng} \frac{AFC}{\text{Period}} \quad (B.19)$$

$$\text{Insurance} = 0.0035AFC \quad (B.20)$$

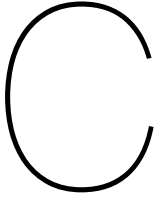
$$\text{Interest} = \text{interest rate} \left(AFC \frac{(1 + \text{interest rate})^2 \text{Period}}{-1 + (1 + \text{interest rate})^2 \text{Period}} \right) \quad (B.21)$$

The total cost is the summation of the ten listed components. The cost analysis requires input from the user. For an indication of these values, the user is referred to reference [33] and [1].

B.5. Phalanx

The Phalanx flight mechanics toolbox originated at the TU Delft as part of the Design Engineering Engine. Over the years the system was featured in a number of European projects, including in the multidisciplinary optimization of a BWB [40]. The program can best be described as a variable fidelity scheme that is applicable to both rotorcraft and fixed-wing aircraft. Due to its modular architecture, Phalanx is capable of linking sub-models from different disciplines to construct a single, non-linear aircraft model. Using the automatically generated aircraft model, the system is able to describe the behaviour of the vehicle. Before the various stability analysis can be initiated, an equilibrium condition needs to be established. By deploying each of the control surfaces individually and monitoring their influence, the program is able to find a trimmed condition. Once the trimmed condition is found, the user can select the type of analysis he or she is interested in. Amongst the available options are time domain simulations and an analysis of the handling quality levels. Another feature embedded in Phalanx is the possibility to fly the actual aircraft using the FlightGear package.

At the heart of the flight mechanics toolbox are the equations of motion. Modelling the equations using multi-body dynamics creates a flexible program that allows for deformations during manoeuvres and the deployment of the landing gear. The Matlab based program employs a module library from which various components can be selected. The complexity, or fidelity, of the program can be defined using identifiers linked to a specific module. This set-up allows users to quickly modify or expand existing computational blocks to tailor the simulation to their needs. The input required for these simulations are dependent on the selected modules. The minimum input comprises of: the stability and control derivatives; reference values; flight condition information; inertia tensor; aircraft mass; control surface data; and information on the engine. The data pertaining to each of these components is stored within an aircraft *struct*, that is build using the aircraft definition script. This script provides the program with a high level description of the vehicle and the fidelity of scheme. In addition, it links the aircraft specific data to the simulation using a string-identifier. For further information on the program, the reader is referred to reference [40].



Sensitivity Data

In Chapter 7 the influence of the available regression and correlation models on the response surface have been described. An elaborate overview of the results of this analysis is presented this appendix. The appendix is concluded by providing detailed information on the computed error for each of the analysed parameters.

C.1. Sensitivity Data: Regression and Correlation Models

Table C.1: Accuracy of the exponential correlation model on the various parameters

Correlation model: Exp		Samples: 200						
Polynomial order			C_{n_β}	$C_{n_{\delta_r}}$	LD	W_{wing}	MTOW	DOC
0	e_{avg}	120.44%	4.40%	0.39%	0.90%	0.41%	0.20%	
	σ	566.51%	3.60%	0.31%	0.79%	0.31%	0.16%	
1	e_{avg}	74.67%	4.49%	0.43%	0.90%	0.44%	0.22%	
	σ	275.95%	4.01%	0.30%	0.70%	0.30%	0.16%	
2	e_{avg}	43.98%	4.69%	0.36%	0.75%	0.40%	0.18%	
	σ	84.70%	4.20%	0.29%	0.69%	0.29%	0.14%	
Samples: 400		C_{n_β}	$C_{n_{\delta_r}}$	LD	W_{wing}	MTOW	DOC	
0	e_{avg}		49.29%	5.11%	0.46%	0.94%	0.46%	0.25%
	σ		114.14%	3.47%	0.29%	0.61%	0.28%	0.15%
1	e_{avg}	37.27%	4.42%	0.45%	0.79%	0.48%	0.26%	
	σ	61.00%	3.57%	0.27%	0.54%	0.28%	0.15%	
2	e_{avg}	53.34%	4.60%	0.40%	0.64%	0.40%	0.22%	
	σ	198.35%	4.72%	0.26%	0.57%	0.28%	0.15%	

Table C.2: Accuracy of the Gaussian correlation model on the various parameters

Correlation model:		Gaussian						
Samples:		200						
Polynomial order			C_{n_β}	$C_{n_{\delta_r}}$	LD	W_{wing}	$MTOW$	DOC
0	e_{avg}	201.73%	7.62%	0.48%	1.40%	0.48%	0.22%	
	σ	1008.43%	7.48%	0.41%	0.92%	0.38%	0.18%	
1	e_{avg}	39.35%	5.93%	0.44%	1.02%	0.46%	0.23%	
	σ	58.93%	4.77%	0.33%	0.67%	0.34%	0.16%	
2	e_{avg}	45.25%	4.18%	0.36%	0.76%	0.38%	0.18%	
	σ	84.01%	3.58%	0.29%	0.69%	0.30%	0.14%	
Samples:		400	C_{n_β}	$C_{n_{\delta_r}}$	LD	W_{wing}	$MTOW$	DOC
0	e_{avg}	35.39%	5.48%	0.46%	0.89%	0.47%	0.25%	
	σ	43.97%	3.66%	0.29%	0.60%	0.29%	0.17%	
1	e_{avg}	67.71%	6.02%	0.48%	0.95%	0.50%	0.27%	
	σ	203.14%	5.13%	0.34%	0.91%	0.36%	0.19%	
2	e_{avg}	55.80%	5.02%	0.39%	0.66%	0.41%	0.22%	
	σ	214.38%	4.47%	0.26%	0.56%	0.27%	0.14%	

Table C.3: Accuracy of the linear correlation model on the various parameters

Correlation model:		Lin						
Samples:		200						
Polynomial order			C_{n_β}	$C_{n_{\delta_r}}$	LD	W_{wing}	$MTOW$	DOC
0	e_{avg}	94.55%	4.34%	0.38%	0.99%	0.42%	0.20%	
	σ	399.78%	3.52%	0.32%	0.79%	0.34%	0.16%	
1	e_{avg}	86.42%	4.80%	0.39%	0.92%	0.42%	0.21%	
	σ	349.77%	4.03%	0.30%	0.76%	0.32%	0.15%	
2	e_{avg}	44.22%	4.43%	0.35%	0.75%	0.38%	0.18%	
	σ	91.09%	3.82%	0.28%	0.70%	0.29%	0.14%	
Samples:		400	C_{n_β}	$C_{n_{\delta_r}}$	LD	W_{wing}	$MTOW$	DOC
0	e_{avg}	44.95%	5.18%	0.46%	0.91%	0.47%	0.25%	
	σ	89.51%	3.81%	0.29%	0.56%	0.32%	0.17%	
1	e_{avg}	36.10%	4.41%	0.46%	0.80%	0.48%	0.26%	
	σ	51.25%	3.73%	0.29%	0.54%	0.30%	0.16%	
2	e_{avg}	36.17%	4.44%	0.39%	0.67%	0.42%	0.22%	
	σ	91.62%	4.39%	0.26%	0.58%	0.28%	0.15%	

Table C.4: Accuracy of the spherical correlation model on the various parameters

Correlation model:		Spherical						
Samples:		200						
Polynomial order			C_{n_β}	$C_{n_{\delta_r}}$	LD	W_{wing}	MTOW	DOC
0	e_{avg}	129.96%	4.45%	0.39%	0.93%	0.41%	0.20%	
	σ	626.15%	3.48%	0.32%	0.78%	0.32%	0.15%	
1	e_{avg}	82.57%	4.62%	0.41%	0.93%	0.45%	0.22%	
	σ	314.25%	3.88%	0.31%	0.74%	0.33%	0.16%	
2	e_{avg}	49.43%	4.30%	0.35%	0.75%	0.38%	0.18%	
	σ	126.64%	3.90%	0.28%	0.70%	0.29%	0.14%	
Samples:		400	C_{n_β}	$C_{n_{\delta_r}}$	LD	W_{wing}	MTOW	DOC
0	e_{avg}	35.39%	5.48%	0.46%	0.89%	0.47%	0.25%	
	σ	43.97%	3.66%	0.29%	0.60%	0.29%	0.17%	
1	e_{avg}	47.03%	4.40%	0.46%	0.80%	0.49%	0.26%	
	σ	112.54%	3.44%	0.30%	0.54%	0.30%	0.16%	
2	e_{avg}	42.68%	4.87%	0.40%	0.64%	0.41%	0.22%	
	σ	128.30%	4.84%	0.25%	0.60%	0.27%	0.15%	

Table C.5: Accuracy of the cubic correlation model on the various parameters

Correlation model:		Cubic						
Samples:		200						
Polynomial order			C_{n_β}	$C_{n_{\delta_r}}$	LD	W_{wing}	MTOW	DOC
0	e_{avg}	77.36%	13.37%	0.53%	1.99%	0.53%	0.24%	
	σ	217.90%	19.34%	0.41%	1.76%	0.43%	0.20%	
1	e_{avg}	40.23%	5.37%	0.45%	1.11%	0.46%	0.22%	
	σ	66.77%	5.57%	0.31%	0.78%	0.33%	0.16%	
2	e_{avg}	45.12%	4.31%	0.36%	0.75%	0.39%	0.19%	
	σ	99.25%	3.34%	0.27%	0.70%	0.28%	0.14%	
Samples:		400	C_{n_β}	$C_{n_{\delta_r}}$	LD	W_{wing}	MTOW	DOC
0	e_{avg}	116.01%	10.31%	0.56%	2.18%	0.50%	0.27%	
	σ	420.60%	8.59%	0.38%	2.21%	0.40%	0.21%	
1	e_{avg}	61.86%	6.65%	0.49%	0.99%	0.51%	0.27%	
	σ	160.71%	6.99%	0.32%	0.94%	0.34%	0.18%	
2	e_{avg}	35.15%	4.65%	0.41%	0.66%	0.42%	0.22%	
	σ	85.97%	4.29%	0.27%	0.59%	0.29%	0.16%	

Table C.6: Accuracy of the spline correlation model on the various parameters

Correlation model:	Spline	Samples: 200	C_{n_β}	$C_{n_{\delta_r}}$	LD	W_{wing}	MTOW	DOC
Polynomial order								
0	e_{avg}	284.08%	6.36%	0.46%	1.33%	0.49%	0.22%	
	σ		1519.71%	4.76%	0.40%	1.01%	0.38%	0.19%
1	e_{avg}	41.95%	6.02%	0.42%	0.99%	0.44%	0.21%	
	σ		59.81%	4.72%	0.30%	0.68%	0.33%	0.16%
2	e_{avg}	45.60%	4.39%	0.37%	0.77%	0.38%	0.18%	
	σ		102.49%	3.77%	0.28%	0.67%	0.30%	0.14%
Samples: 400		C_{n_β}	$C_{n_{\delta_r}}$	LD	W_{wing}	MTOW	DOC	
Polynomial order								
0	e_{avg}	105.88%	4.59%	0.45%	1.03%	0.47%	0.24%	
	σ		430.09%	3.98%	0.37%	0.84%	0.38%	0.19%
1	e_{avg}	47.23%	5.25%	0.47%	0.82%	0.49%	0.26%	
	σ		107.09%	4.78%	0.33%	0.65%	0.33%	0.18%
2	e_{avg}	37.54%	4.62%	0.39%	0.65%	0.40%	0.21%	
	σ		96.27%	4.22%	0.26%	0.57%	0.27%	0.14%

C.2. Sensitivity Data: Error Estimation

To derive the accuracy of the system, 40 randomly generated winglets have been analysed by VSAero and compared to the response surface estimates.

Table C.7: *Established error for C_{n_β} and $C_{n_{\delta_r}}$, as computed using a 2nd order polynomial cubic scheme*

Config	C_{n_β}			$C_{n_{\delta_r}}$		
	Analysis	Estimate	Error	Analysis	Estimate	Error
1	0.0138	0.0052	62.43%	-0.0153	-0.0157	2.45%
2	0.0255	0.0238	6.62%	-0.0254	-0.0254	0.15%
3	0.0030	0.0005	82.48%	-0.0060	-0.0058	4.26%
4	0.0417	0.0399	4.27%	-0.0219	-0.0234	6.57%
5	0.0444	0.0379	14.76%	-0.0229	-0.0239	4.44%
6	-0.0029	-0.0018	35.39%	-0.0065	-0.0070	6.75%
7	0.0026	0.0006	78.09%	-0.0062	-0.0050	19.17%
8	0.0237	0.0270	14.19%	-0.0184	-0.0181	1.86%
9	0.0249	0.0344	38.40%	-0.0182	-0.0171	5.98%
10	0.0066	0.0034	49.26%	-0.0069	-0.0077	11.67%
11	-0.0001	-0.0006	550.04%	-0.0105	-0.0104	1.21%
12	0.0278	0.0209	24.70%	-0.0172	-0.0163	5.09%
13	0.0252	0.0245	2.78%	-0.0245	-0.0245	0.02%
14	0.0052	0.0042	18.93%	-0.0073	-0.0069	5.36%
15	0.0195	0.0209	7.45%	-0.0134	-0.0139	4.12%
16	0.0123	0.0116	6.18%	-0.0101	-0.0107	6.03%
17	0.0056	0.0046	17.24%	-0.0090	-0.0093	3.41%
18	0.0551	0.0532	3.45%	-0.0247	-0.0275	10.99%
19	0.0285	0.0296	3.90%	-0.0228	-0.0217	4.73%
20	0.0054	0.0074	37.81%	-0.0149	-0.0135	9.27%
21	0.0232	0.0197	15.10%	-0.0189	-0.0184	2.73%
22	-0.0052	-0.0030	43.57%	-0.0116	-0.0097	15.89%
23	0.0068	0.0101	49.18%	-0.0069	-0.0061	11.62%
24	0.0181	0.0134	26.14%	-0.0156	-0.0158	1.15%
25	0.0192	0.0211	9.82%	-0.0116	-0.0121	4.68%
26	0.0091	0.0063	30.82%	-0.0104	-0.0106	1.73%
27	0.0399	0.0402	0.64%	-0.0257	-0.0266	3.62%
28	0.0064	0.0072	11.38%	-0.0130	-0.0130	0.45%
29	0.0161	0.0145	9.90%	-0.0132	-0.0138	4.10%
30	0.0231	0.0176	23.82%	-0.0146	-0.0145	0.28%
31	0.0049	0.0052	5.89%	-0.0098	-0.0097	1.01%
32	0.0194	0.0233	19.96%	-0.0190	-0.0178	6.36%
33	0.0185	0.0141	23.75%	-0.0155	-0.0157	1.07%
34	0.0665	0.0532	19.94%	-0.0409	-0.0398	2.86%
35	0.0346	0.0355	2.74%	-0.0267	-0.0260	2.62%
36	0.0372	0.0346	7.05%	-0.0216	-0.0229	5.59%
37	0.0287	0.0390	35.59%	-0.0230	-0.0229	0.51%
38	0.0388	0.0360	7.24%	-0.0213	-0.0217	1.66%
39	0.0300	0.0304	1.40%	-0.0146	-0.0148	1.21%
40	0.0340	0.0327	3.80%	-0.0184	-0.0190	3.52%

Table C.8: Established error for C_{l_β} and C_{Y_β} , as computed using a 2nd order polynomial cubic scheme

Config	C_{l_β}			$C_{Y_\delta_r}$		
	Analysis	Estimate	Error	Analysis	Estimate	Error
1	-0.1606	-0.1040	35.25%	-0.0852	-0.0648	23.99%
2	-0.1210	-0.1412	16.64%	-0.1162	-0.1163	0.10%
3	-0.1481	-0.1006	32.08%	-0.0542	-0.0473	12.67%
4	-0.1466	-0.1164	20.59%	-0.1569	-0.1507	3.94%
5	-0.1460	-0.1397	4.28%	-0.1679	-0.1521	9.40%
6	-0.0806	-0.0826	2.53%	-0.0404	-0.0389	3.54%
7	-0.1401	-0.1001	28.58%	-0.0543	-0.0421	22.51%
8	-0.1143	-0.1202	5.18%	-0.1080	-0.1110	2.78%
9	-0.0878	-0.1069	21.74%	-0.1159	-0.1365	17.77%
10	-0.1328	-0.0973	26.69%	-0.0628	-0.0513	18.31%
11	-0.0895	-0.1007	12.59%	-0.0472	-0.0455	3.51%
12	-0.1476	-0.1079	26.89%	-0.1249	-0.1062	14.93%
13	-0.1584	-0.1337	15.58%	-0.1150	-0.1145	0.41%
14	-0.0834	-0.0986	18.18%	-0.0608	-0.0661	8.68%
15	-0.0953	-0.1045	9.67%	-0.0960	-0.0990	3.16%
16	-0.1230	-0.1061	13.69%	-0.0752	-0.0752	0.04%
17	-0.0810	-0.0937	15.64%	-0.0628	-0.0619	1.36%
18	-0.1295	-0.1058	18.28%	-0.1881	-0.1812	3.69%
19	-0.1029	-0.1224	18.96%	-0.1218	-0.1247	2.36%
20	-0.0773	-0.1055	36.47%	-0.0634	-0.0708	11.57%
21	-0.1249	-0.1352	8.27%	-0.1103	-0.1019	7.67%
22	-0.0547	-0.0855	56.43%	-0.0359	-0.0394	9.73%
23	-0.0913	-0.0966	5.80%	-0.0668	-0.0734	9.79%
24	-0.1522	-0.1209	20.56%	-0.0952	-0.0836	12.19%
25	-0.1207	-0.1253	3.76%	-0.1034	-0.1060	2.59%
26	-0.0989	-0.1135	14.82%	-0.0718	-0.0699	2.58%
27	-0.1212	-0.0985	18.71%	-0.1482	-0.1460	1.51%
28	-0.0877	-0.0987	12.52%	-0.0656	-0.0696	6.15%
29	-0.1286	-0.1100	14.47%	-0.0906	-0.0831	8.20%
30	-0.1658	-0.1220	26.37%	-0.1067	-0.0969	9.19%
31	-0.1173	-0.1119	4.64%	-0.0608	-0.0638	5.03%
32	-0.0848	-0.1266	49.27%	-0.0965	-0.1070	10.87%
33	-0.1561	-0.1222	21.70%	-0.0988	-0.0960	2.82%
34	-0.1713	-0.1323	22.77%	-0.2253	-0.1948	13.53%
35	-0.1336	-0.1433	7.26%	-0.1387	-0.1428	2.96%
36	-0.1247	-0.1268	1.72%	-0.1481	-0.1445	2.42%
37	-0.1012	-0.1324	30.74%	-0.1233	-0.1465	18.85%
38	-0.1424	-0.1177	17.34%	-0.1553	-0.1489	4.16%
39	-0.1200	-0.1061	11.55%	-0.1263	-0.1267	0.33%
40	-0.1219	-0.1209	0.89%	-0.1329	-0.1363	2.52%

Table C.9: *Established error for $\delta_{r_{cw}}$, as computed using a 2nd order polynomial cubic scheme*

$\delta_{r_{cw}}$ Analysis	Estimate	Error
39.2595	16.7163	57.42%
43.8206	45.0615	2.83%
21.7216	7.4517	65.69%
83.0040	82.6842	0.39%
84.7809	68.5981	19.09%
-19.1225	-19.5689	2.33%
18.0446	-0.3817	102.12%
56.0387	54.0388	3.57%
59.7197	75.6729	26.71%
41.9760	11.4408	72.74%
-0.3790	-3.2874	767.42%
70.5489	55.5439	21.27%
44.9149	42.1706	6.11%
30.7872	37.0173	20.24%
63.6782	61.8825	2.82%
53.5698	46.5676	13.07%
27.1314	21.8692	19.40%
97.2282	81.3577	16.32%
54.6696	61.6594	12.79%
15.7073	24.4135	55.43%
53.3553	47.6016	10.78%
-19.7649	-5.0992	74.20%
42.4407	58.0881	36.87%
50.5014	33.7382	33.19%
72.4244	70.1237	3.18%
37.9683	28.3260	25.40%
67.9023	71.7903	5.73%
21.6105	28.2264	30.61%
53.1661	42.4236	20.21%
69.0663	51.3546	25.64%
21.8225	23.0484	5.62%
44.7346	60.5437	35.34%
52.2309	52.4768	0.47%
70.8986	64.4580	9.08%
56.5638	66.1483	16.94%
75.1178	71.1750	5.25%
54.4173	64.1410	17.87%
79.5727	76.9160	3.34%
89.5651	89.8283	0.29%
80.6870	77.6843	3.72%

Table C.10: Established error for λ_{sp} and λ_{rm} , as computed using a 2nd order polynomial cubic scheme

Config	λ_{sp}			λ_{rm}		
	Analysis	Estimate	Error	Analysis	Estimate	Error
0.0278	0.0319	14.57%	3.5525	3.3720	5.08%	
0.0190	0.0155	18.13%	3.8731	3.8135	1.54%	
0.0473	0.0438	7.47%	2.6289	3.4612	31.66%	
0.0123	0.0180	46.59%	3.1413	3.4452	9.67%	
0.0154	0.0180	16.98%	3.7584	3.5451	5.68%	
0.0405	0.0420	3.69%	4.0653	3.2639	19.71%	
0.0323	0.0370	14.55%	3.2597	3.4219	4.98%	
0.0041	0.0178	333.07%	4.6842	3.6914	21.20%	
0.0065	0.0114	75.39%	3.7838	3.4134	9.79%	
0.0313	0.0362	15.91%	3.0333	3.2836	8.25%	
0.0535	0.0400	25.19%	3.3573	3.4654	3.22%	
0.0244	0.0179	26.56%	3.8571	3.4010	11.82%	
0.0255	0.0212	16.67%	3.2596	3.6284	11.32%	
0.0205	0.0278	35.64%	3.9516	3.4483	12.74%	
0.0165	0.0208	26.42%	3.5789	3.3320	6.90%	
0.0336	0.0265	21.05%	2.8279	3.4022	20.31%	
0.0223	0.0265	18.74%	3.3278	3.2617	1.98%	
0.0168	0.0228	35.72%	3.4116	3.5287	3.43%	
0.0002	0.0191	11019.55%	3.4965	3.3523	4.12%	
0.0355	0.0305	14.10%	4.4019	3.4113	22.50%	
0.0146	0.0169	15.87%	4.3127	3.5971	16.59%	
0.0346	0.0410	18.44%	3.6895	3.1870	13.62%	
0.0219	0.0198	9.88%	3.3680	3.3634	0.14%	
0.0243	0.0290	19.09%	3.0199	3.3106	9.63%	
0.0299	0.0156	47.93%	3.7210	3.2834	11.76%	
0.0329	0.0283	14.04%	3.7502	3.3884	9.65%	
0.0097	0.0149	54.22%	3.2613	3.4497	5.78%	
0.0316	0.0274	13.38%	3.4507	3.2880	4.72%	
0.0323	0.0228	29.50%	2.5752	3.3762	31.11%	
0.0173	0.0205	18.85%	3.2221	3.4978	8.55%	
0.0270	0.0269	0.36%	3.7172	3.4211	7.97%	
0.0146	0.0242	65.66%	4.1611	3.7942	8.82%	
0.0104	0.0177	70.60%	3.8757	3.4934	9.86%	
0.0033	0.0145	343.97%	3.8786	3.7461	3.41%	
0.0053	0.0162	203.74%	3.7809	3.5483	6.15%	
0.0055	0.0143	158.38%	3.1355	3.4502	10.03%	
0.0076	0.0177	133.70%	3.5644	3.3921	4.84%	
0.0236	0.0144	39.06%	3.0747	3.2573	5.94%	
0.0057	0.0128	123.68%	3.6810	3.4400	6.55%	
0.0022	0.0176	710.21%	3.0521	3.3028	8.21%	

Table C.11: Established error for ζ_{dr} and ω_{dr} , as computed using a 2nd order polynomial cubic scheme

Config	ζ_{dr}			ω_{dr}		
	Analysis	Estimate	Error	Analysis	Estimate	Error
0.1509	0.1444	4.34%	0.2794	0.2488	10.95%	
0.3645	0.3195	12.34%	0.2428	0.2558	5.37%	
0.0712	0.0764	7.40%	0.3143	0.2189	30.35%	
0.3659	0.4629	26.50%	0.2834	0.2504	11.63%	
0.4418	0.4637	4.94%	0.2691	0.2687	0.12%	
0.0422	0.0269	36.31%	0.1876	0.2183	16.36%	
0.0636	0.0360	43.35%	0.2752	0.2209	19.71%	
0.3945	0.3512	10.96%	0.2069	0.2440	17.91%	
0.3332	0.4074	22.29%	0.2048	0.2235	9.14%	
0.1121	0.0771	31.22%	0.2764	0.2278	17.58%	
0.0753	0.0595	21.05%	0.2154	0.2246	4.30%	
0.2647	0.2729	3.08%	0.2541	0.2365	6.95%	
0.3021	0.3122	3.35%	0.2866	0.2562	10.60%	
0.1170	0.1413	20.75%	0.1919	0.2213	15.34%	
0.2656	0.2555	3.81%	0.2136	0.2340	9.51%	
0.1637	0.1827	11.58%	0.2735	0.2317	15.28%	
0.1202	0.1062	11.65%	0.2060	0.2355	14.31%	
0.5684	0.5855	3.00%	0.2701	0.2445	9.48%	
0.3258	0.3249	0.27%	0.2286	0.2551	11.61%	
0.1710	0.1706	0.24%	0.1723	0.2334	35.47%	
0.3362	0.2400	28.61%	0.2317	0.2552	10.15%	
0.0173	0.0541	212.47%	0.1633	0.2224	36.16%	
0.1287	0.1761	36.77%	0.2173	0.2196	1.06%	
0.2193	0.1926	12.16%	0.2946	0.2510	14.80%	
0.2451	0.2754	12.37%	0.2336	0.2551	9.21%	
0.1697	0.1435	15.46%	0.2120	0.2392	12.83%	
0.4715	0.4358	7.57%	0.2622	0.2317	11.64%	
0.1766	0.1231	30.25%	0.2088	0.2297	10.03%	
0.1685	0.2067	22.67%	0.2933	0.2379	18.88%	
0.2608	0.2651	1.66%	0.2984	0.2470	17.21%	
0.1197	0.1130	5.60%	0.2344	0.2363	0.80%	
0.2980	0.3282	10.11%	0.1859	0.2403	29.25%	
0.1636	0.2354	43.88%	0.2649	0.2453	7.40%	
0.5765	0.5861	1.67%	0.2765	0.2630	4.90%	
0.5137	0.4002	22.09%	0.2549	0.2709	6.24%	
0.3211	0.3795	18.19%	0.2636	0.2563	2.78%	
0.3952	0.3980	0.71%	0.2220	0.2654	19.56%	
0.2829	0.4002	41.48%	0.2796	0.2523	9.75%	
0.3779	0.3989	5.57%	0.2431	0.2346	3.49%	
0.4120	0.4198	1.89%	0.2682	0.2503	6.67%	

Analysis of the response surface indicates disproportionately large errors for parameter values approaching zero. These values have a significant impact on the average error. As a result the error becomes distorted, leading to uncharacteristic e_{avg} and σ . Therefore, the error of parameters approaching zero are omitted, to provide a better representation of the accuracy of the scheme.

Table C.12: *average error and standard deviation of the presented parameters*

	e_{avg}	σ
C_{n_β}	35.15%	85.97%
$C_{n_{\delta r}}$	4.65%	4.29%
C_{l_β}	18.23%	12.37%
C_{y_β}	7.45%	6.42%
$\delta_{r_{cw}}$	22.35%	23.91%
λ_{sp}	58.00%	114.82%
λ_{rm}	9.98%	7.30%
ζ_{dr}	15.31%	13.20%
ω_{dr}	12.62%	8.65%

Bibliography

- [1] D.P. Raymer. Aircraft design: A conceptual approach, american institute of aeronautics and astronautics. Inc., Reston, VA, 1999.
- [2] J. Roskam and C.T.E. Lan. *Airplane aerodynamics and performance*. DARcorporation, 1997.
- [3] E. Obert. Static directional stability and control of transport aircraft. Technical Report A-128, Fokker-VFW B.V., 1979-2013. department CB-AP.
- [4] R.H. Liebeck. Design of the blended wing body subsonic transport. *Journal of aircraft*, 41(1):10–25, 2004.
- [5] G. La Rocca M. Voskuyl and F. Dircken. Controllability of blended wing body aircraft. In *Proceedings of the 26th International Congress of the Aronautical Sciences, ICAS 2008, including the 8th AIAA Aviation Technology, Integration and Operations (ATIO) Conference, Anchorage, Alaska, September 14-19,(2008)*. Optimage Ltd., 2008.
- [6] L.L.M. Veldhuis S.M. Waters, M. Voskuyl and F.J.J.M.M. Geuskens. *Control allocation performance for a blended wing body–Wind-tunnel and numerical investigation into non-linear aerodynamic control surface effects and their impact on design*. PhD thesis, Master thesis, Delft University of Technology, 2012.
- [7] A.P. Hettema. Vertical tail design: Development of a rapid aerodynamic analysis method. Master's thesis, TU Delft, Delft University of Technology, 2015.
- [8] P.S. Park and K. Rokhsaz. Effects of a winglet rudder on lift-to-drag ratio and wake vortex frequency. In *21st applied aerodynamics conference, Orlando, Florida. Paper AIAA-2003-4069*, 2003.
- [9] M.V. Cook and H.V. De Castro. The longitudinal flying qualities of a blended-wing-body civil transport aircraft. *Aeronautical Journal*, 108(1080):75–84, 2004.
- [10] E. Torenbeek. *Advanced aircraft design: Conceptual design, technology and optimization of subsonic civil airplanes*. John Wiley & Sons, 2013.
- [11] M. Drela M.A. Sargeant J.I. Hileman, Z.S. Spakovszky and A. Jones. Airframe design for silent fuel-efficient aircraft. *Journal of aircraft*, 47(3):956–969, 2010.
- [12] E. Torenbeek and R. Slingerland. *Innovative configurations and advanced concepts for future civil aircraft*. Von Karman Institute for Fluid Dynamics, 2005.
- [13] M.V. Cook. *Flight Dynamics - Principles*. Elsevier, 2007.
- [14] W.H.J.J. Van Staveren J.A. Mulder and J.C. Van der Vaart. *Flight dynamics (lecture notes): ae3-302*. TU Delft, 2000.
- [15] E. Obert. *Aerodynamic design of transport aircraft*. Ios Press, 2009.
- [16] R.P. Harper and G.E. Cooper. Handling qualities and pilot evaluation. *Journal of Guidance, Control, and Dynamics*, 9(5):515–529, 1986.
- [17] European Aviation Safety Agency (EASA). <https://easa.europa.eu/document-library/certification-specifications>. As visited on 28 January, 2016.
- [18] F.W. Lanchester. *Aerodynamics: constituting the first volume of a complete work on aerial flight*, volume 1. D. Van Nostrand, 1908.

- [19] Engineering Sciences Data Unit (ESDU). Aerodynamic principles of winglets. Item 98013, June 1998.
- [20] R.T. Whitcomb. *A design approach and selected wind-tunnel results at high subsonic speeds for wing-tip mounted winglets*. National Aeronautics and Space Administration, 1976.
- [21] A. Elham and M.J.L. Van Tooren. Winglet multi-objective shape optimization. *Aerospace Science and Technology*, 37:93–109, 2014.
- [22] J.D. Anderson Jr. *Fundamentals of aerodynamics, fourth edition*. Tata McGraw-Hill Education, 2005.
- [23] M.M. Munk. The minimum induced drag of aerofoils. 1923.
- [24] W. Yamazaki K. Takenaka, K. Hatanaka and K. Nakahashi. Multidisciplinary design exploration for a winglet. *Journal of Aircraft*, 45(5):1601–1611, 2008.
- [25] R. Eppler. Induced drag and winglets. *Aerospace science and Technology*, 1(1):3–15, 1997.
- [26] S.A. Ning and I. Kroo. Tip extensions, winglets, and c-wings: conceptual design and optimization. *AIAA Paper*, 7052, 2008.
- [27] S.G. Fletcher and P.F. Jacobs. *Experimental results of winglets on first, second, and third generation jet transports*, volume 72674. National Aeronautics and Space Administration, Scientific and Technical Information Office, 1978.
- [28] J.K. Nathman and A. McComas. Comparison of stability and control calculations from vortex lattice and panel methods. *AIAA Paper*, 7052, 2008.
- [29] J.H. Wei. Parametric modelling for determining aircraft stability & control derivatives. Master's thesis, TU Delft, Delft University of Technology, 2016.
- [30] B Maskew. *Program VSAero: A computer program for calculating the non-linear aerodynamic characteristics of arbitrary configurations*. NASA, 1982.
- [31] A. Sobester A. Forrester and A. Keane. *Engineering design via surrogate modelling: a practical guide*. John Wiley & Sons, 2008.
- [32] G. La Rocca A. Elham and M.J.L. Van Tooren. Development and implementation of an advanced, design-sensitive method for wing weight estimation. *Aerospace Science and Technology*, 29(1):100–113, 2013.
- [33] Chau Girvin Lyon Rawdon Scott Wright Liebeck, Andrastek. Advanced subsonic airplane design & economic studies. 1995.
- [34] H.B. Nielsen S.N. Lophaven and J. Søndergaard. Dace - a matlab kriging toolbox. Technical Report IMM-TR-2002-12, Technical University of Denmark, 2002. Information and Mathematical Modeling Institute.
- [35] A.J. Colozza. Hydrogen storage for aircraft applications overview. *NASA CR-2002-211867, September*, 2002.
- [36] F. Yin A.G. Rao and J.P. van Buijtenen. A novel engine concept for aircraft propulsion. *ISABE, Gothenburg, ISABE-2011-1341*, 7052, 2011.
- [37] P.T. Soderman and T.N. Aiken. Full-scale wind-tunnel tests of a small unpowered jet aircraft with t-tail. *NASA TN D-6573, November*, 1971.
- [38] F.S. Heiberger C.A. Schollenberger, J.W. Humphreys and R.M. Pearson. Results of winglet development studies for dc-10 derivatives. Technical report, NASA, 1983.

- [39] G.W Loptien. The effect of winglets on the kc-135a aircraft. Technical report, DTIC Document, 1978.
- [40] D. Bohnke A. Rizzi T. Pfeiffer, B. Nagel and M. Voskuijl. Implementation of a heterogeneous, variable-fidelity framework for flight mechanics analysis in preliminary aircraft design. In *Proceedings of the 60 Deutscher Luft-und Raumfahrtkongress, 27-29 September 2011, Bremen, Duitsland*, 2011.